UNIVERSITÀ DEGLI STUDI DI CAGLIARI

DIPARTIMENTO DI SCIENZE FISICHE

Low Mass Dimuon Production in p-A Collisions at 400 GeV/*c* with the NA60 Detector

A Thesis submitted for the Degree of Doctor of Philosophy

January 2011

Advisors

Prof. Gianluca USAI
Dott. Alessandro DE FALCO

PhD School Director

Prof. Giovanni BONGIOVANNI

Antonio URAS

XXIII PhD Cycle (2008 ▫ 2010)

Contents

I

Introduction, Apparatus and Simulations

1

Introduction and Physics Motivations

High energy nuclear collisions are the most effective tool for studying nuclear matter under extreme conditions. The intimate structure of the involved nucleons is revealed, and the collisions can be interpreted in terms of parton interactions, described by the Quantum Chromo Dynamics (QCD).

If the energy density and the temperature characterizing the collision surpass the critical values predicted by QCD ($T_c \sim 150$ MeV and $\epsilon_c \sim 1$ GeV/fm^3), investigations of the non-perturbative properties of QCD on a discrete space-time lattice predict the creation of an extended medium of deconfined partons, called Quark-Gluon Plasma (QGP). Simultaneously with this deconfinement transition, chiral symmetry is expected to be restored [40]. The phase diagram is qualitatively described in the left panel of Figure 1.1, where ρ_0 is the density of the nuclear matter inside the ordinary nuclei.

Electromagnetic radiation (real and virtual photons) is continuously emitted during the whole evolution of the collisions (see right panel of Figure 1.1) sensing the entire space-time history of the reaction. After a pre-equilibrium state, the "fireball" expands through several phases: the evolution starts with a quark-gluon plasma phase, characterized by a temperature $T > T_c$; then a chemical freeze-out is reached, at temperature $_{\rm ch}$, when hadrons stop being produced; scattering interactions between the hadrons stop at a later stage, when kinematical freeze-out is established at temperature $T_{\rm kin}$.

During the whole evolution of the fireball, the radiation decouples from the strongly interacting matter at the point of creation, and can be revealed through its conversion into lepton pairs (dileptons). The information carried by dileptons, in turns, arrives to the detectors almost unaffected, since this probe is not sensible to the strong color field dominating inside the deconfined medium (dileptons only suffer from Coulomb scattering − which would in any case affect hadronic probes as well). For this reason,

dileptons can be regarded as the ideal tool to probe the whole evolution of nuclear collisions, in the cleanest way as possible: dilepton measurements, in fact, have always played a key-role in the high energy nuclear physics experimental scenario [69].

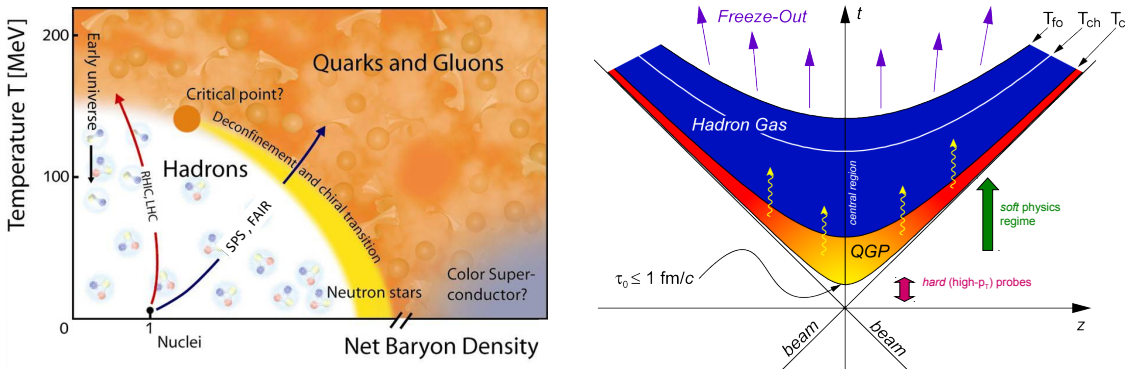

Figure 1.1: *Phase diagram from hadronic matter to a QGP phase as a function of temperature and barionic density (left). Space-time diagram for a nucleus-nucleus collision (right).*

1.1 Light Vector Mesons Production in High-Energy Nuclear Collisions

The study of light vector mesons in ultra-relativistic heavy ion collisions is mainly motivated by the fact that in-medium modifications of the hadron masses and widths should be observed with increasing temperature and density, in particular in a deconfined, hot nuclear matter environment where the chiral symmetry is expected to be maximally restored. It was predicted [63, 48, 37, 29] that if these modifications were observed, they could be an indication of chiral symmetry restoration, possibly related to a transition from hadronic matter to a deconfined QGP: to investigate these modifications, high temperature and density can be achieved by experiments using heavy-ion collisions.

The ρ meson is a primary candidate for probing in-medium effects on hadronic matter, due to its strong coupling to the $\pi\pi$ channel and its short lifetime of only 1.3 fm/c, much shorter than the lifetime of the fireball created in a heavy-ion collision. The spectral modifications of the ρ are observable via the kinematic reconstruction of the decay products.

The first indication of a possible medium modification of the ρ meson came from the CERES [5] and HELIOS-3 [51] Collaborations at CERN in 1995. CERES observed an enhancement over the hadronic contributions, in Pb-Au collisions, in the mass range between 300 and 700 MeV/c^2. However, the resolution of the data – as well as

the available statistics – did not allow a quantitative measurement of any mass shift or change in the width of the ρ vector meson.

The NA60 experiment has accumulated in the dimuon low mass region (below $\sim$ 1.2 GeV/c^2) a statistics $\sim$ 1000 times larger than the one collected by the experiment CERES in dielectrons [18, 30, 31]. This allowed, for the first time, a very accurate study of the properties of the ρ meson in nuclear collisions, without any *a priori* assumption on its shape, see Figure 1.2.

The observations by NA60 can thus discriminate between the main theoretical scenarios developed historically for describing the in-medium properties of the ρ meson, the unmodified ρ scenario being clearly ruled out. Two main models were developed in the 90s, predicting the behavior of the ρ in the hot and dense matter produced in heavy-ion collisions. The first model directly links the mass of the ρ to the restoring of chiral symmetry, predicting a lowering of the mass pole by more than 100 MeV/c^2 in the hot and dense medium [29, 48]. The second was a hadronic many-body inspired model which predicted a strong broadening due to the coupling of the ρ to baryons and due to in-medium modifications of pions, but essentially no mass shift [63]. As shown by the data, the scenario of a broadening provides a rather good description of the observed excess, while the dropping mass models [29, 48] is clearly ruled out.

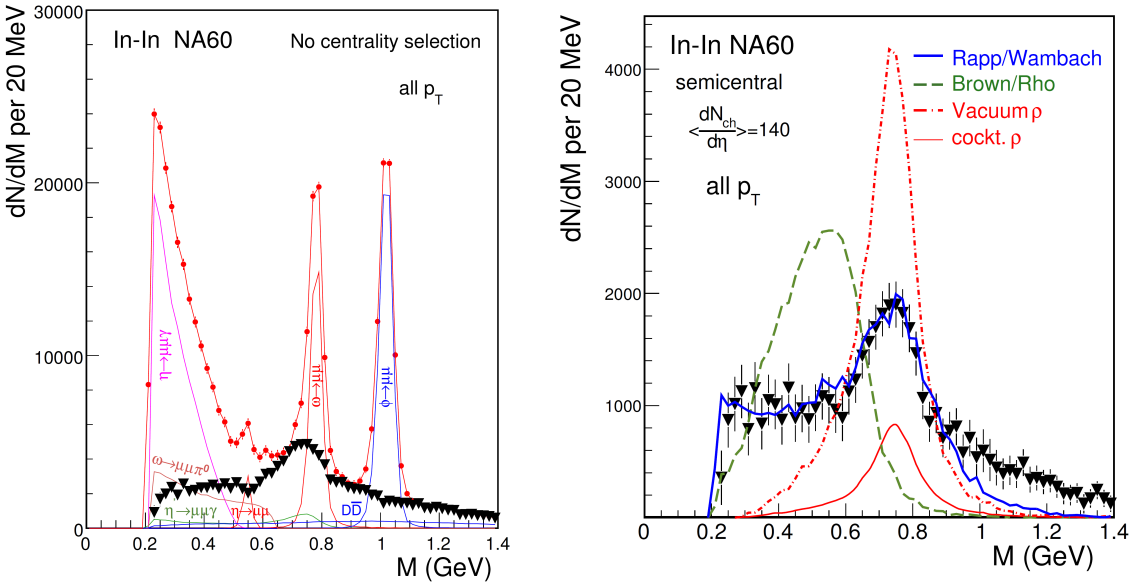

Figure 1.2: *(Left Panel) NA60 dimuon mass spectrum in In-In collisions, integrated over centrality, before (dots) and after (triangles) of the known decay sources. (Right Panel) The excess dimuons before acceptance correction, reflecting the in-medium ρ spectral function averaged over space-time and momenta. The theoretical predictions also shown are renormalized to the data for $M < 0.9$ GeV/c^2. Beyond 0.9 GeV/c^2, other physical processes take over. Details can be found in [18, 32, 70].*

1.1.1 Strangeness Enhancement

Strange-particle production is one of the observables expected to deliver detailed information on the reaction dynamics of ultrarelativistic heavy-ion collisions. In particular, strangeness enhancement was proposed long ago as a signature of a possibly occurring phase transition to QGP [62, 43]. The ϕ meson is a key experimental probe in this context, being an almost pure $s\bar{s}$ state (see Chapter 4): the strangeness is "hidden", and therefore without influence on a hadro-chemical equilibrium. On this ground, ϕ yield should depend more sensitively than that of kaons (the lightest mesons having a strange component) on a strangeness enhancement stemming from the early partonic phase.

Significantly enhanced production of the ϕ meson was indeed proposed as a QGP signature in nucleus-nucleus collisions, and recently studied from p-p to Pb-Pb collisions at the CERN SPS by the NA35, NA45 (CERES), NA49, NA50 and NA60 experiments [12, 15, 14, 39, 4, 26]. Discrepancies between the measured yields in the lepton ($\phi \rightarrow e^+e^-$ and $\phi \rightarrow \mu^+\mu^-$) and kaon ($\phi \rightarrow K^+K^-$) channels have been observed, comparing the data coming from the various experiments. Further insight recently came from a new analysis on the NA60 data, the only experiment allowing a detailed study in both the decay channels [33]: a good agreement has been observed between the yields of the $\phi \rightarrow K^+K^-$ and $\phi \rightarrow \mu^+\mu^-$ channels in the common range $p_T > 0.9$ GeV/c.

What the SPS experiments found was that strangeness production is already significantly enhanced in lighter collision systems, such as C-C, Si-Si and S-S. The ϕ yield breaks the N_{part} scaling, and the ϕ enhancement, quantified as $\langle\phi\rangle/N_{part}$, saturates already for Si-Si central collisions, see Figure 1.3.

1.2 Intermediate Mass Dileptons in High-Energy Nuclear Collisions

In the previous Section we have seen that the excess observed by NA60 in the mass spectrum below 1 GeV/c^2 is consistent with a dominant contribution from the $\pi + \pi \rightarrow \rho \rightarrow \mu + \mu$ process, with the associated ρ spectral function showing a strong broadening, but essentially no shift in mass.

Moving to higher masses, the NA60 experiment also observed an excess in the invariant mass region $1 < M < 2.5$ GeV/c^2 in In-In collisions at 158 GeV/c, with respect to the expected contributions given by Drell-Yan dimuons and muon pairs from the decays of D meson pairs [19, 21]. These latter sources properly account for the dimuons produced in proton-nucleus collisions. This excess is found to be prompt, not due to enhanced charm production, with pronounced differences to Drell-Yan pairs.

The left panel of Figure 1.4 shows the NA60 In-In inclusive invariant mass spectrum of the excess dimuons for the complete range $0.2 < M < 2.5$ GeV/c^2, with all known sources subtracted (except for the ρ), integrated over p_T , corrected for

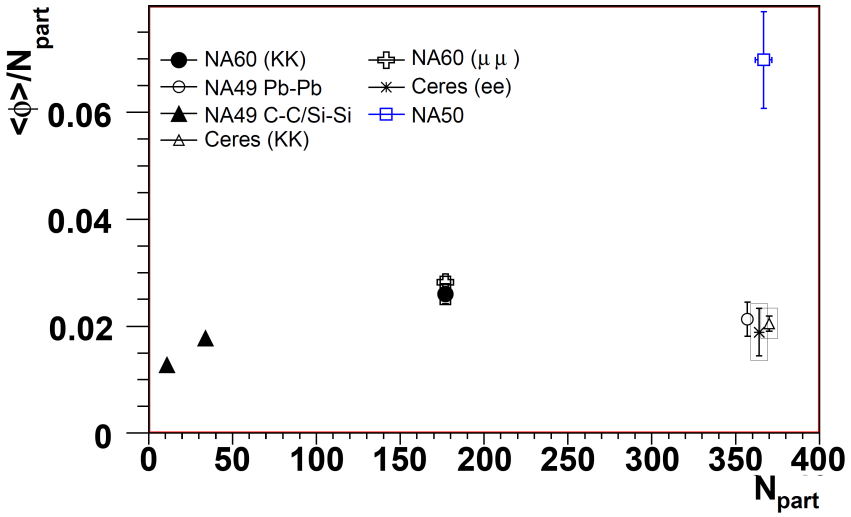

Figure 1.3: $\langle\phi\rangle/N_{\mathrm{part}}$ *as a function of* N_{part}*, as determined by various experiments in central collisions. The experimental points (apart from the NA50 measurement, clearly out of the common trend) suggest that* $\langle\phi\rangle/N_{\mathrm{part}}$ *already saturates for Si-Si central collisions. Figure taken from [33].*

experimental acceptance and normalized absolutely to the charged-particle rapidity density [70, 32]. As it can be seen, a Planck-like (nearly exponential) shape of the mass spectrum is observed above 1 GeV/c^2: this observation, together with the absence of any polarization as expected for radiation from a randomized system [20] and the purely exponential m_{T} spectra, justifies the interpretation of this excess in terms of a thermal radiation emitted from the fireball.

The observed Planck-like thermal radiation is compatible both with hadronic and partonic sources. This dual scenario can be clarified considering the kinematics of the dileptons emitted from the medium: dileptons, in fact, resulting from the conversion of virtual photons, profits from the combined information of the invariant mass and transverse momentum, thus providing further insight with respect to real photons. This allowed the study of the slope parameter T_{eff} – associated with the transverse momentum spectra – as a function of mass, as shown in the right panel of Figure 1.4. The trend rises with mass up to the ρ, followed by a sudden decline above. The rise for $M < 1$ GeV/c^2 is consistent with radial flow of a hadronic emission source. On the contrary, the seeming absence of significant flow for $M > 1$ GeV/c^2 suggests a dominantly partonic emission source in this region [70, 32].

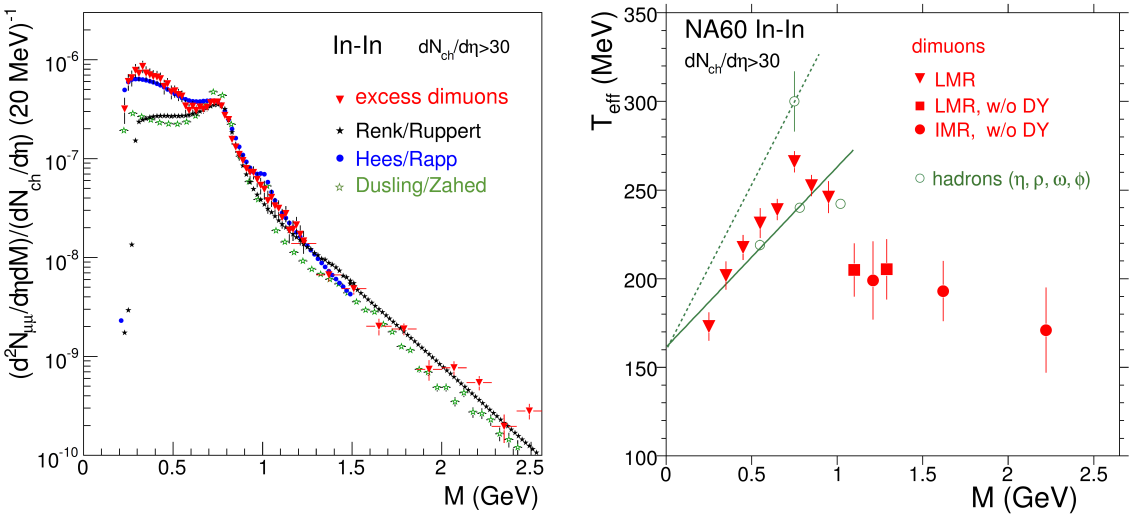

Figure 1.4: *(Left Panel) Acceptance-corrected invariant mass spectrum of the excess dimuons, integrated over p_T, compared with three different sets of thermal-model results in absolute terms. (Right panel) Inverse slope parameter T_{eff} of the acceptance-corrected m_T spectra as a function of the dimuon mass [70, 32].*

1.3 Light Mesons Production in p-A Collisions

p-A data serve as a robust reference baseline for the heavy-ion data, providing measurements in an environment of cold nuclear matter. In fact, the study of the nuclear dependence of the properties of the light neutral mesons (kinematic distributions, production cross sections, particle ratios and spectral properties) allows one to have a solid understanding of the physics processes involved in elementary nuclear collisions, so that the heavy-ion observations can be interpreted on more robust grounds.

In addition, proton-nucleus data also stimulates a genuine physics interest, allowing one to measure particle properties in a rather clean environment: this is the case of the measurement of the electromagnetic transition form factors of the η and ω mesons, also considered in the present thesis, concerning an *intensive* property of the particles, having no dependence on the physics of the underlying process in which the particles are created.

1.3.1 Transverse Momentum Distributions for the Light Neutral Mesons

In high-energy nuclear collisions, the transverse momentum of the produced particles is one of the most significant variables to be considered and studied. Since the transverse observables are created within the collision (the initial state being just longitudinal by definition) their distributions are directly linked to the physics mechanisms being responsible of the production of the final state particles, and their interpretation

is then a crucial feature in every high energy physics experiment.

In general, physics mechanisms responsible for particle production in high energy physics involve the contribution of both hard and soft processes. In contrast to hard processes, whose description can be afforded by means of perturbative methods, the description of particle production in soft interactions is not well-established within QCD. Current models of hadron-hadron collisions at high energies, such as the event generator PYTHIA [68], combine perturbative QCD for the description of hard parton interactions with phenomenological approaches to model the soft component of the produced particle spectrum.

Data on charged particle production in hadron-hadron collisions are needed to tune these models, before they can provide a detailed description of the existing measurements and predictions for particle production in the next available facilities, first of all the Large Hadron Collider (LHC) which in 2010 started colliding proton beams at $\sqrt{s} = 3.5$ TeV − the highest energy ever reached in particle collisions. These data include the measurement of multiplicity, pseudorapidity (η) and transverse momentum (p_{T}) distributions of produced particles, as well as their possibly existing correlations.

Until now there is a general lack of measurements of the p_{T} distributions in elementary collisions (where no deconfined medium is thought to be created) for the light neutral mesons η, ρ, ω and ϕ. The NA27 experiment [76] is the only one having measured a variety of light mesons, including η, ρ, ω and ϕ, in proton-proton collisions at 400 GeV/c ($\sqrt{s} = 27.5$ GeV). Concerning the p_{T} distributions, results are given for charged mesons $\pi^{\pm}$, $K^{\pm}$, p, $\bar{\mathrm{p}}$ and for the neutral pseudoscalar mesons π^0 and η, see Figure 1.5. Experimental data are fitted using the functional form:

$$\frac{\mathrm{d}N}{\mathrm{d}p_{\mathrm{T}}^2} \propto \left(1 + \frac{p_{\mathrm{T}}^2}{p_0^2}\right)^{-\beta} , \tag{1.1}$$

which is a standard form for a mixture of soft $(1+\ldots)$ and hard processes ($p_{\mathrm{T}}^{-\beta}$). This latter component is a pure power law, used e.g. in the ALICE publication on p_{T} spectra [1] to describe the hard component above 3 GeV/c. No data on p_{T} distributions for the light vector mesons ρ, ω and ϕ were reported in the NA27 reference.

The inclusive production of the strange vector mesons K^{*0}, $\bar{K}^{*0}$ and ϕ has been also measured in interactions of 920 GeV protons with C, Ti and W targets with the HERA-B detector [3] at the HERA storage ring. Differential cross sections as a function of rapidity and p_{T} have been measured in the central rapidity region and for $p_{\mathrm{T}} < 3.5$ GeV/c. The results for the ϕ meson are shown in Figure 1.6. As already seen with the NA27 experiment, data are successfully fitted with the function described by Equation 1.1, while a thermal-like exponential form fails to describe the experimental points above $p_{\mathrm{T}} \simeq 1$ GeV/c:

$$\frac{1}{p_{\mathrm{T}}}\frac{\mathrm{d}N}{\mathrm{d}p_{\mathrm{T}}} = \frac{1}{m_{\mathrm{T}}}\frac{\mathrm{d}N}{\mathrm{d}m_{\mathrm{T}}} = 2\frac{\mathrm{d}N}{\mathrm{d}p_{\mathrm{T}}^2} \propto \exp\left(-\frac{m_{\mathrm{T}}}{T}\right) . \tag{1.2}$$

This latter parametrization, on the contrary, successfully describes the observed p_{T} spectrum for the ϕ mesons produced in In-In collisions at $\sqrt{s} = 17.3$ GeV at various

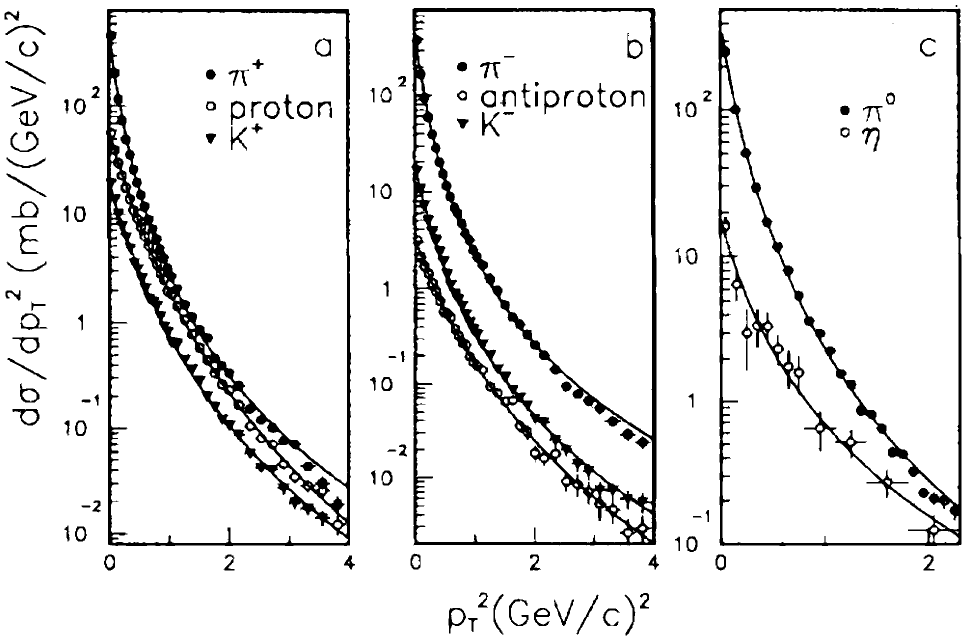

Figure 1.5: *NA27 p_T measurement for various charged and neutral particles, including the η meson of interest for the present thesis. Figure taken from [76].*

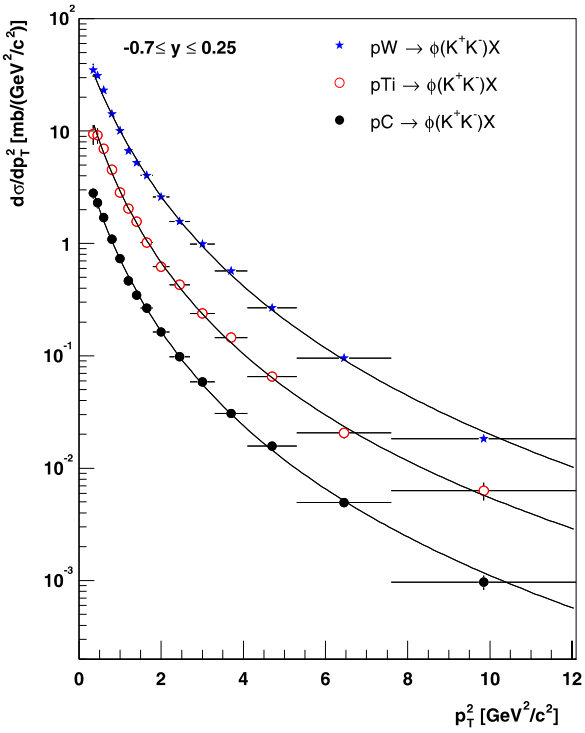

Figure 1.6: *HERA-B p_T measurement for the ϕ meson in p-C, p-Ti and p-W collisions. Experimental distributions are fitted with the function described by Equation 1.1. Details can be found in [3].*

centralities, as recently shown by the NA60 experiment [26], see Figure 1.7. This observation is indeed suggestive of different mechanisms being responsible for the particle production in p-p, p-A on one side, and heavy ion collisions on the other.

Going beyond the energy scale of interest for the present work, we may still cite the current efforts by the experiments taking data at the CERN LHC, where proton-proton collisions at $\sqrt{s} = 900$ GeV, $\sqrt{s} = 2.36$ TeV and $\sqrt{s} = 7$ TeV energies became recently available, probing a new energy regime. Figure 1.8 reports the first inclusive p_T measurement performed with the ALICE and CMS detectors [1, 41] at $\sqrt{s} = 900$ GeV and $\sqrt{s} = 2.36$ TeV: both experiments have excellent coverage on a large p_T range, starting from $p_T \simeq 150$ MeV/c; data published by the ALICE Collaboration extend up to $p_T = 10$ GeV/c. It is worth to note how – even at such large $\sqrt{s}$ values, still the functional form used to describe the data must contain a term accounting for the shape of the distribution at low-p_T, beyond the power-law term successfully describing the high-p_T component.

Coming to the present analysis capabilities, we note that the NA60 data in p-A collisions allows one to study in detail the p_T distributions for the vector mesons ω and ϕ, while the corresponding distributions for the η and ρ mesons are more difficult to extract. Concerning the η meson, its 2-body decay is heavily suppressed, so one has to rely on the measure of the Dalitz decay $\eta \to \mu^+\mu^-\gamma$, trying to infer the p_T distribution of the parent meson by comparing MC and measured distributions for the p_T of the muon pair. Concerning the ρ meson, its contribution within the hadronic cocktail describing the mass spectrum can only be fixed with accuracy in a p_T-integrated analysis. Even exploiting the large data sample at our disposal, a reliable disentanglement of the ρ contribution for single bins of p_T cannot be easily afforded.

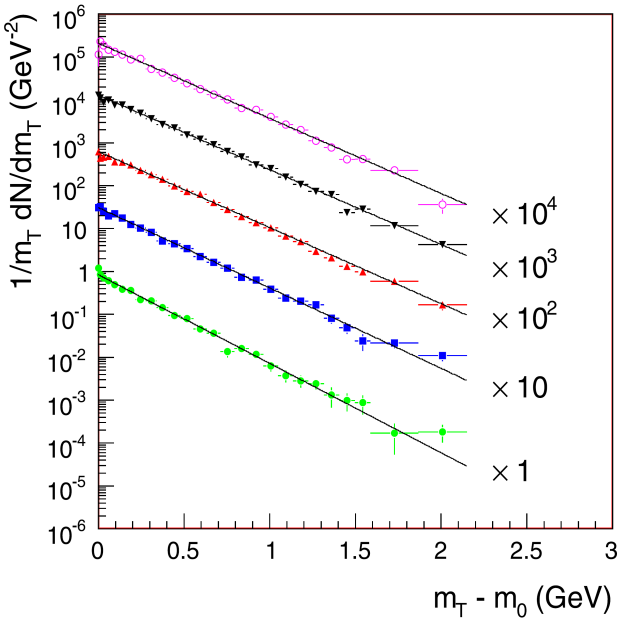

Figure 1.7: *NA60 p_T measurement for the ϕ meson in In-In collisions at various centralities. Experimental distributions are fitted with the thermal-like function described by Equation 1.2. The detailed analysis can be found in [26].*

It should be also noted that the measurement of the p_T distributions for the ω and ϕ mesons, obtained in the present analysis of the NA60 p-A data, represent the first measurement of these kinematic distributions at the energy of $\sqrt{s} = 27.5$ GeV. This should motivate and aid further theoretical efforts, to gain a deeper understanding in a field which still suffers from lack of solid experimental observations providing the needed support to theoretical and phenomenological models.

1.3.2 Light Mesons Relative Cross Sections and Strangeness Enhancement

The description of the dimuon mass spectrum in terms of the expected hadronic sources allows the investigation of the nuclear dependence of the production cross sections for the light neutral mesons, accessible by considering the mass spectra for each production target separately. As it is widely documented in the literature, a rather simple and natural parametrization for the nuclear cross sections in proton-nucleus collisions is the power law:

$$\sigma_{pA} \propto A^{\alpha} , \tag{1.3}$$

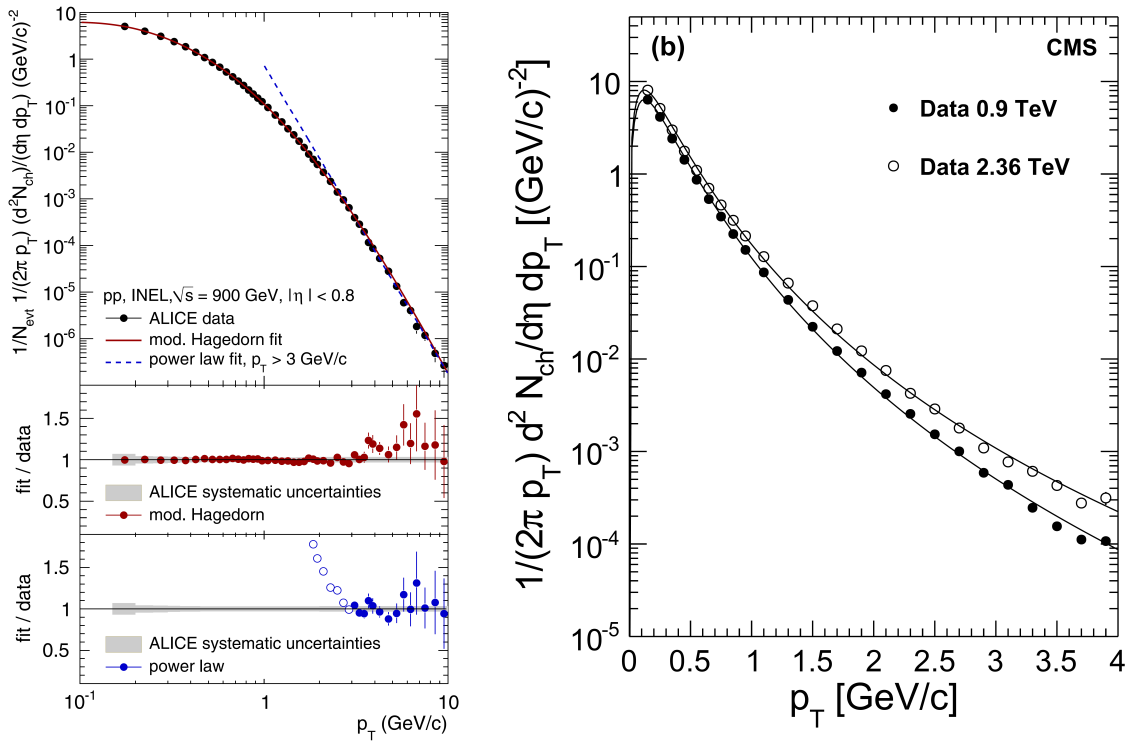

Figure 1.8: *Inclusive p_T measurement by the ALICE (left) and CMS (right) experiments at the LHC. Figures are taken from [1] and [41], where all the details can be found.*

where A is the number of nucleons in the target nucleus. The value of the parameter α depends on the nature of the process involved in the production of the particle. A parameter $\alpha = 2/3$ can be interpreted in terms of a production cross section directly proportional to the transverse area of the target nucleus, independently on the thickness of the nuclear medium traversed; on the other hand, $\alpha = 1$ is typical of hard processes, having small cross sections and then scaling proportionally to the number of nucleons available for the scattering. Values of the α parameter smaller than 2/3 or greater than 1 are also still possible, if one consider the chance of having absorption or re-interaction effects taking place in the nuclear medium.

In general, the interpretation of any α parameter must rely on a model: this model should not only describe the microscopic interaction between the incoming proton and the nucleons of the target nucleus, but also has to give a picture of the modifications induced by the presence of the dense nuclear medium both on the elementary proton-nucleon cross section and on the properties of the produced particles, like their mass width (determining their lifetime) and their interaction cross section.

In order to study the nuclear dependence of the production cross sections, even when its description is given in terms of the simple power-law parametrization (1.3), the largest sample of materials should be used, spanning the largest possible range of A values. This allows one to properly determine the trend as a function of A and the value of the α parameter, together with its possible dependence as a function of the rapidity and the transverse momentum of the produced particles. It is well known, in fact, that the α parameter − whatever the process − varies as a function of x_F (or rapidity) and as a function of p_T, as can be seen for example in Figure 1.9 for the pseudoscalar mesons π^0 and η.

In particular, a rising trend of α with the p_T may be expected considering that mesons of high p_T are produced for high exchanged momenta by the incoming proton inside the target nucleus: the higher the exchanged momentum, the more effectively the single nucleons of the target nucleus are probed, leading to values of $\alpha \to 1$. The rise of α with the p_T of the particle, the so-called "Cronin effect", may be also related to initial state effects, namely the broadening of the intrinsic transverse momentum distribution of the primary partons, due to the elastic collisions possibly experienced while traversing the nuclear matter. According to this second interpretation, the larger the nucleus is, the larger p_T is gained by the primary partons before the hard scattering which originates the final particles, the larger p_T will be inherited by the particles in the final state; from here, one may infer that heavier targets have more chances to produce final state particles with higher p_T, which translates in increasing α values with raising p_T.

Evidence for Cronin effect was also found for the ϕ meson by the HERA-B experiment in p-A collisions [3], profiting of nuclear targets of C, Ti and W. Their measurement is reported in Figure 1.10 together with the historical measurements by Cronin *et al.* [42] for positive kaons. A comprehensive compilation of the presently available measurements of α_ϕ in p-A collisions has been recently reviewed in [67].

The NA60 400 GeV proton-nucleus data profit from a variety of six target mate-

rials, namely Be, Cu, In, W, Pb and U. This gives access to a clear understanding on how the production cross section for the light mesons scales as a function of A. The available statistics also makes it possible to perform a study of the A-dependence of the nuclear production cross sections as a function of p_T.

Strangeness Enhancement

From the analysis of the production cross sections for the light neutral mesons, enhancement of strange production can be revealed considering the ratio between the production yields ϕ/ω and η/ω. However, beside the experimental observations focused on the hot nuclear matter effects, there is until now a lack of accurate data on the nuclear dependence of ϕ production in proton-nucleus collisions. Such measurements are needed in view of establishing a solid understanding of the physics processes involved in a cold nuclear matter environment, so that the heavy-ion observations can be interpreted on more robust grounds. The present analysis will focus on

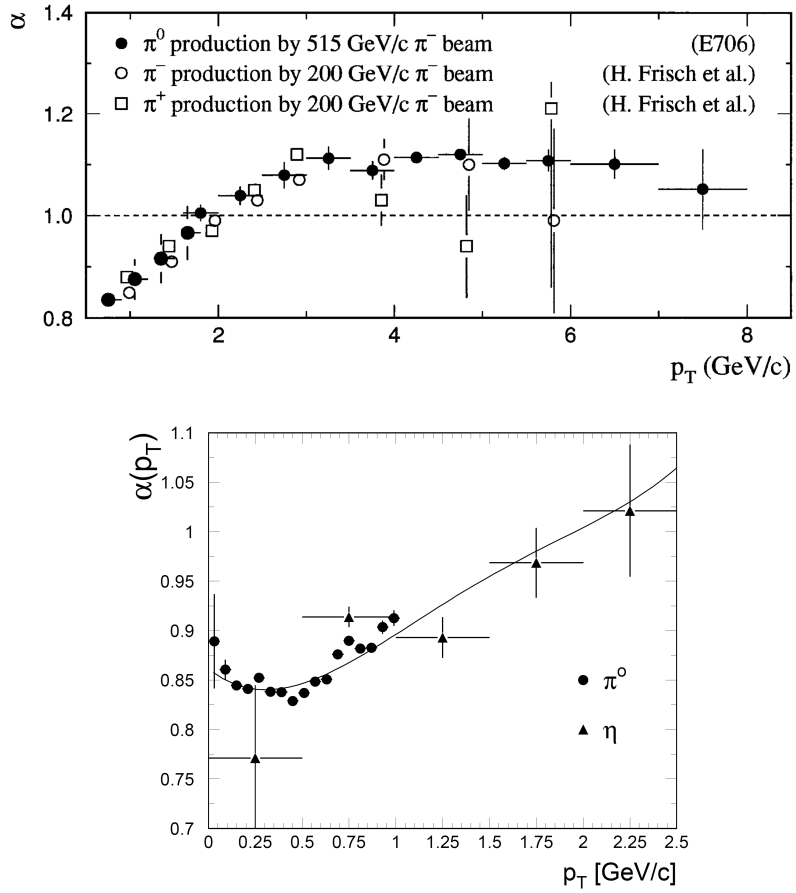

Figure 1.9: *α for $\pi^{\pm}$ and π^0 as a function of p_T (bottom panel) measured by E706 and E258 experiments [59]. α for π^0 and η as a function of p_T (top panel) measured by CERES in 450 GeV p-Be and p-Au collisions [6].*

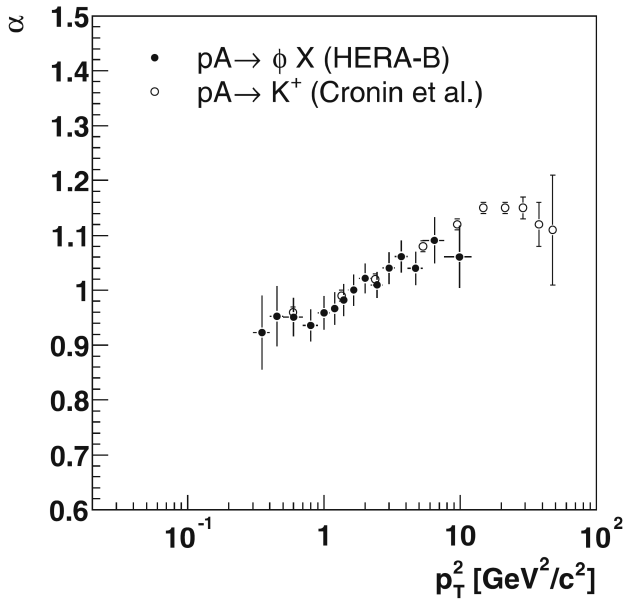

Figure 1.10: *Measured values of $\alpha(p_T)$ for ϕ production. Details can be found in [3].*

this item, too, studying the dependence of the $\sigma_\phi/\sigma_\omega$ and $\sigma_\eta/\sigma_\omega$ ratios as a function of A, thanks to variety of nuclear targets involved, ranging from Beryllium (A = 9) to Uranium (A = 238).

1.3.3 Electromagnetic Transition Form Factors for the η and ω Mesons

The third major item covered by the analysis presented in this work concerns the measure of the electromagnetic transition form factors for the η and ω mesons, which have been studied here through their Dalitz decays $\eta \to \mu^+\mu^-\gamma$ and $\omega \to \mu^+\mu^-\pi^0$. In these $A \to B\ell^+\ell^-$ processes, the mesons decay electromagnetically into a virtual photon with mass M – in turn converting into a lepton pair – and a third body, see Figure 1.11.

The probability of formation of a lepton pair with an effective mass M_{ℓ^+l} in a conversion decay $A \to B\ell^+\ell^-$ is proportional to the probability of emitting a virtual photon with a corresponding invariant mass. The probability of emission of this photon is strongly influenced by the dynamic electromagnetic structure arising at the vertex of the transition $A \to B$: this structure is due to creation of virtual states and is described by the transition form factor, which modifies the dilepton effective mass spectrum with respect to the one predicted by QED assuming point-like particles (firstly derived by N.M. Kroll and W. Wada [46] in the 1950s). This difference can be formally described by a function of M, usually expressed as $|F_{AB}(M)|^2$, known as *transition form factor*.

The electromagnetic structure of the "region of transition of A into B" can then be obtained by studying the probability of the decay $A \to B\ell^+\ell^-$ as a function of the invariant mass of the lepton pair. Experimentally, this can be achieved by comparing the measured spectrum of lepton pairs in decays $A \to B\ell^+\ell^-$, with the QED calculations for point like particles: in this way, one has direct access to the transition form factor $|F_{AB}(M)|^2$. It should be noted that the Dalitz decays $A \to B\ell^+\ell^-$ only allows to study the transition form factor $|F_{AB}(M)|^2$ in the time-like region, because of the kinematical constraints; the space-like region can be accessed exploiting reactions in which the lepton pairs annihilate in a virtual photon, in turn originating the composite particles.

As explained in [22], the physics interest in studying Dalitz decays and the associated transition form factors is twofold. First, the electromagnetic interaction continues to be an extremely useful tool to gain deeper insight into meson structure, while the role of the resonance interaction in this context is far from being quantitatively settled. Since the experiments are very difficult, the quality of the existing data is generally poor. Second, and related to the last point, the study of direct production of dileptons in high-energy nuclear collisions in the context of thermal radiation requires a precise and complete knowledge of the characteristics and the relative weights for the existing decay channels, and this is universally true at all facilities where such studies are ongoing (SIS, SPS, RHIC, LHC and FAIR in the future).

Form Factors in the Vector Meson Dominance Framework

In a process $A \to B\gamma^*$, the strength of the coupling between the hadron A and the virtual photon γ^* depends on the amount of electric charge of A probed by the photon. Since the "probing power" of the photon depends on the exchanged momentum, i.e. on its invariant mass, it follows that the strength of the $A-\gamma^*$ coupling, described by the electromagnetic form factor, depends on the invariant mass of the emitted

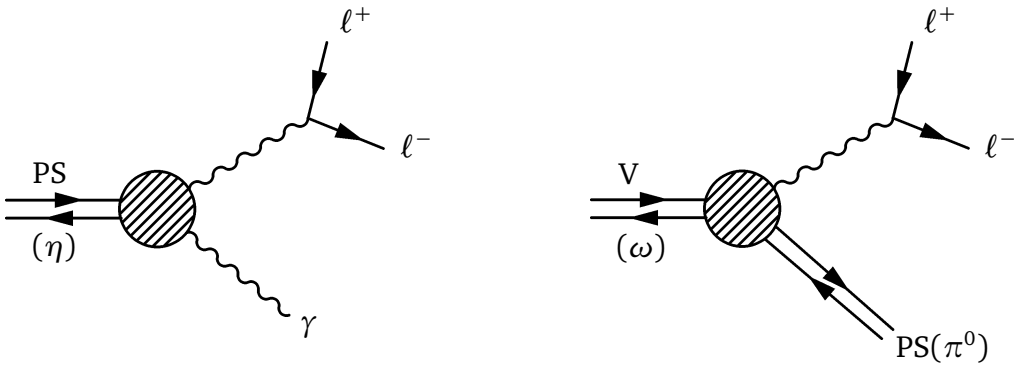

Figure 1.11: *Dalitz decays for the η and ω mesons. The probability of emission of the virtual photon is strongly influenced by the dynamic electromagnetic structure arising at the interaction vertex.*

virtual photon.

However, experimental investigations have shown that another phenomenon plays a significant and peculiar role in determining the dependence of the electromagnetic form factor on the invariant mass of the exchanged virtual photon. This phenomenon consists in the resonance interaction between photons and hadrons, and it is often referred to as the Vector Meson Dominance (VMD). A comprehensive review of the topic is contained in [47].

The VMD is made possible by the existence of neutral short lived mesons with the same quantum numbers as those of the photon. These are vector mesons with spin 1 and negative parity: $J^P = 1^-$. The lightest of them are the ρ^0 meson ($m_\rho = 775\,\mathrm{MeV}/c^2$), the ω meson ($m_\omega = 783\,\mathrm{MeV}/c^2$) and the ϕ meson ($m_\phi = 1019\,\mathrm{MeV}/c^2$). According to the VMD, a virtual photon can interact with a hadron not only directly, but also after a transition to a virtual vector meson state. In this framework, the Dalitz decays of the η and ω mesons, previously depicted in Figure 1.11, can be expressed by the diagrams shown in Figure 1.12.

The concept that this type of hadron-photon interaction is predominant (hence, the term Vector Meson Dominance) first arose in electron-proton scattering and was later confirmed by a number of other experiments [47]. This mechanism is especially well pronounced in the case of time-like photons whose squared four-momentum q^2 approaches the squared mass of the vector meson ($q^2 \approx m_V^2$). Here the virtual meson reaches its mass shell, i.e. becomes real: this "realization" of the virtual intermediate particle results in a strong resonance enhancement in the form factor describing the emission of the virtual photon. Then, having passed the resonance maximum, the form factor begins to diminish. Its further behavior depends on the contribution of heavier vector mesons and it is not sufficiently well known. In any case, the kinematic constraints for the electromagnetic form factors, describing the Dalitz decays of the η and ω meson, are such that only the contribution of the ρ meson is relevant for the VMD mechanism.

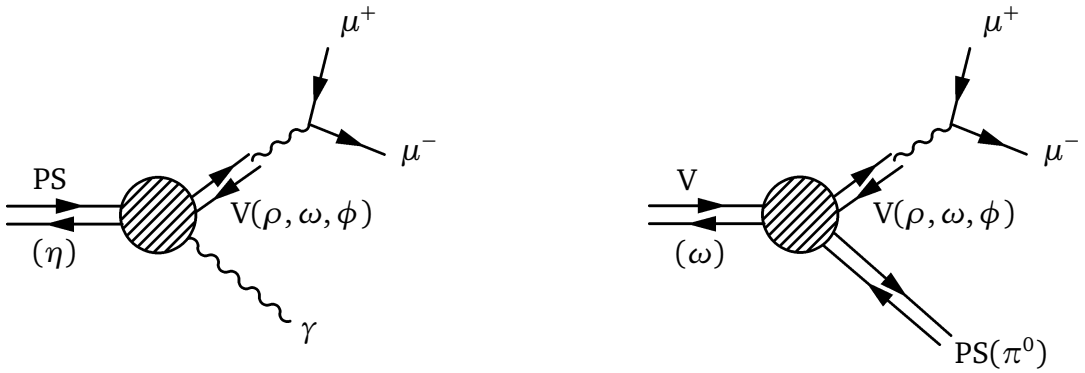

Figure 1.12: *Dimuon decay of the vector mesons ρ, ω and ϕ (left) and the ω Dalitz decay (right) in the framework of the VMD.*

Theoretical Predictions from the VMD

Disregarding the case of the π^0 (only relevant in the e^+e^- channel), the two major Dalitz decays contributing to the dilepton mass range $M < 1.4$ GeV/c^2 of interest for this work are those of the $\eta(548)$ and the $\omega(783)$ mesons. Taking into account the VMD mechanism, the electromagnetic transition form factor of a conversion decay $A \to B\ell^+\ell^-$ is expressed by the formula:

$$F(q^2) = \frac{\sum_{V=\rho,\omega,\phi} \left[g_{ABV}/2g_{V\gamma} \right] m_V^2 \left[m_V^2 - q^2 - i\Gamma_V m_V \right]^{-1}}{\sum_{V=\rho,\omega,\phi} \left[g_{ABV}/2g_{V\gamma} \right]} \tag{1.4}$$

where g_{ABV} and $g_{V\gamma}$ are the corresponding coupling costants, which may be derived from the quark model or extracted from experimental data on $A \to BV$, $A \to B\gamma$ and $V \to \ell^+\ell^-$ decays. If the exchanged momentum q^2 is smaller then the mass of the vector mesons involved in the photon-meson resonance, (1.4) reduces to the pole parametrization:

$$F(q^2) \simeq 1 + q^2 \left[\frac{\mathrm{d}F_{AB}}{\mathrm{d}q^2} \right]_{q^2 \simeq 0} \equiv 1 + q^2\Lambda^{-2} \simeq \left[1 - \frac{q^2}{\Lambda^2} \right]^{-1} , \tag{1.5}$$

where

$$\Lambda^{-2} = \left[\frac{\mathrm{d}F_{AB}}{\mathrm{d}q^2} \right]_{q^2 \simeq 0} \tag{1.6}$$

is the slope of the transition form factor in the VMD framework:

$$\left[\frac{\mathrm{d}F_{AB}}{\mathrm{d}q^2} \right]_{q^2 \simeq 0} = \left(\frac{1}{m_\rho^2} \right) \frac{\sum_{V=\rho,\omega,\phi} \left\{ \left[g_{ABV}/2g_{V\gamma} \right] / \left[g_{AB\rho}/2g_{\rho\gamma} \right] \right\} m_\rho^2/m_V^2}{\sum_{V=\rho,\omega,\phi} \left\{ \left[g_{ABV}/2g_{V\gamma} \right] / \left[g_{AB\rho}/2g_{\rho\gamma} \right] \right\}} . \tag{1.7}$$

Calculations for the Dalitz decay $\eta \to \mu^+\mu^-\gamma$ give the following result:

$$\Lambda_\eta^{-2} = \frac{1}{m_\rho^2} \left[\frac{1 + \frac{1}{9}(m_\rho^2/m_\omega^2) - \beta_\eta(\sqrt{2}/3)(m_\rho^2/m_\phi^2)}{1 + \frac{1}{9} - \beta_\eta(\sqrt{2}/3)} \right] \approx \frac{1.1}{m_\rho^2} \approx 1.83 \ [\mathrm{GeV}/c^2]^{-2} . \tag{1.8}$$

Here, the ratios between the coupling constants $g_{V\gamma}$ and $g_{\eta\gamma V}$ are given by the quark model, assuming $\theta_P = -18°$ for the mixing angle of the pseudoscalar nonet, and $\theta_V = \arcsin(1/\sqrt{3})$ for the mixing angle of the vector nonet − this latter corresponding to the ideal mixing for which the ϕ is a pure $s\bar{s}$ state. The parameter β_η depends on θ_P as follows: $\beta_\eta = \frac{2}{3}[(\sqrt{2}\cos\theta_P + \sin\theta_P)/(\cos\theta_P - \sqrt{2}\sin\theta_P)]$. It should be noted that the assumption on θ_P, whose value has a larger uncertainty than that on θ_V, weakly influences the value of the form factor slope.

Concerning the Dalitz decay $\omega \to \mu^+\mu^-\pi^0$, the VMD prediction for the transition form factor makes the assumption that the contribution of the ρ pole is the only

relevant one. In this case, we simply have:

$$\Lambda_{\omega}^{-2} = \frac{1}{m_{\rho}^2} \approx 1.66 \ [\mathrm{GeV}/c^2]^{-2} \ . \tag{1.9}$$

Available Measurements

The Λ_{η}^{-2} and Λ_{ω}^{-2} pole parameters have been measured by the "Lepton-G" experiments in the late 1970s [34, 35, 47] and more recently by the NA60 experiment in In-In collisions [22].

The "Lepton-G" experimental setup was exploited by several experiments between 1978 and 1980, using 25 and 33 GeV/c π^- beams. The setup includes a magnetic spectrometer with proportional chambers and wire spark chambers for muon pair detection, and a hodoscope γ spectrometer for photon identification. An energy measurement of all secondary particles and a complete reconstruction of the decay kinematics were performed. The experiments accumulated the following statistics:

- $N(\eta \to \mu^+\mu^-\gamma) = 600$
- $N(\omega \to \mu^+\mu^-\pi^0) = 60$

and obtained the following results for the form factors slope:

- $N(\eta \to \mu^+\mu^-\gamma)\ \Lambda^{-2} = (1.9 \pm 0.4)\ [\mathrm{GeV/c^2}]^{-2}$
- $N(\omega \to \mu^+\mu^-\pi^0)\ \Lambda^{-2} = (2.4 \pm 0.2)\ [\mathrm{GeV/c^2}]^{-2}$

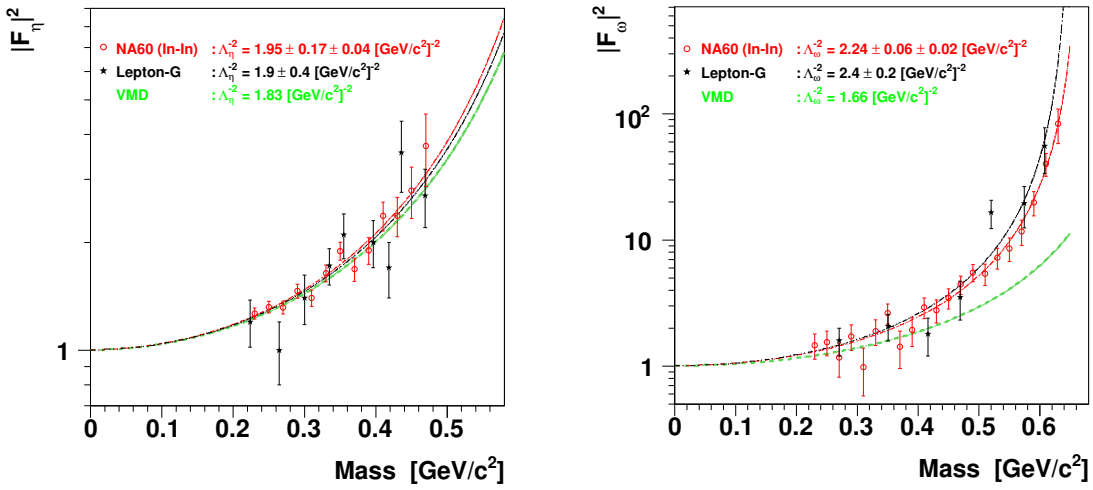

Figure 1.13: *Comparison between experimental data and VMD prediction for the form factors of the η (left) and ω (right) mesons.*

where the errors include both statistical and systematic uncertainties.

The NA60 experiment already studied the electromagnetic transition form factors of the Dalitz decays $\eta \to \mu^+\mu^-\gamma$ and $\omega \to \mu^+\mu^-\pi^0$ analyzing the peripheral In-In data at a beam energy of 158 GeV per nucleon. It should be noted that only the muon pair is measured by the NA60 apparatus, while no measurement nor identification is available for the third body. In this case, then, the processes of interest are disentangled from the dimuon mass spectrum on a statistical basis, by removing all the other known contributes involved in the hadron cocktail. The cumulated statistics is:

- $N(\eta \to \mu^+\mu^-\gamma) \sim 9000$
- $N(\omega \to \mu^+\mu^-\pi^0) \sim 3000$

and the following results for the form factors slope were finally obtained:

- $N(\eta \to \mu^+\mu^-\gamma)\ \Lambda^{-2} = (1.95 \pm 0.17 \pm 0.04)\ [\mathrm{GeV/c^2}]^{-2}$
- $N(\omega \to \mu^+\mu^-\pi^0)\ \Lambda^{-2} = (2.24 \pm 0.06 \pm 0.02)\ [\mathrm{GeV/c^2}]^{-2}$

where the statistical and systematic errors are reported in this order.

As one can observe from Figure 1.13, the Lepton-G and the NA60 experimental values agree among each other both for the η and ω mesons. On the other hand, only the VMD model prediction for the η meson is confirmed by the data, while the one for the ω meson is not, strongly underestimating the observed form factor. The NA60 p-A data can now give a further significant contribution to the measurement, thanks to the high quality and large statistics available.

1.3.4 In-Medium Effects in Cold Nuclear Matter: Current Experimental Scenario

In addition to the predicted modifications of the hadron properties in a deconfined QGP, some theoretical approaches now suggest that in-medium changes of hadrons could be observable even at normal nuclear matter densities [52]. Although this item will not be covered in the present analysis, its general relevance in the scientific contest of interest for this work justifies here an introduction to it.

The existence of in-medium effects in cold nuclear implies that mass and width modifications should be observed for hadrons decaying inside atomic nuclei. According to some of these models (see for example [37]), the mass decrease at normal nuclear density is $\sim 120 - 180$ MeV/c^2 for the ρ and ω mesons and $\sim\ 20 - 40$ MeV/c^2 for the ϕ. Another model [29] predicts that the masses of ρ and ω mesons decrease by 20% at normal nuclear density. These investigations have stimulated a series of measurements to study the effect of surrounding strongly interacting matter on the mass and width of hadrons.

In order to observe these effects in normal nuclear matter, one must rely on low-momentum observations, in order to enhance the fraction of particles decaying inside the nuclei. Experimentally, we can cite at least three measurements of in-medium modifications of the light vector mesons in ordinary nuclear matter, respectively by the KEK-PS E325 Collaboration, the CBELSA/TAPS Collaboration and the CLAS Collaboration. Current investigations are also been carried on by the HADES collaboration [65], still not published yet.

The KEK-PS E325 Collaboration investigated p-A reactions at 12 GeV [60, 64, 71, 53, 57, 56] reporting the observation of an excess on the low-mass sides of the ω and ϕ mesons: this excess presented differences between p-C and p-Cu collisions and was interpreted in terms of modification of the mass of the mesons.

The CB-ELSA/TAPS Collaboration [73, 44] studied the ω mesons produced in γ-LH_2 and γ-Nb interactions. ω mesons produced in γ-LH_2 interactions always decay in vacuum, and their mass spectrum is then used to subtract the in-vacuum component present in the mass spectrum coming from γ-Nb interactions. A broadening of ω line shape is observed, without evidence of mass shift.

The ρ, ω and ϕ mesons were also studied by the CLAS Collaboration [58] in γ-A interactions, with $E_\gamma = 1.5-2.4$ GeV. The data did not suggest any specific in-medium effect (beyond standard nuclear many-body effects) to be necessary in describing ρ production in cold nuclear matter: the photo-produced ρ is described using a Breit-Wigner function, without any in-medium modification to be taken into account.

Another measurement of the ϕ meson in γ-A is also available [38], coming from the SPring8 Collaboration. According to this analysis, the mass and width of the ϕ meson observed in the K^+K^- invariant mass spectrum are consistent with those of the free ϕ meson for all the nuclear targets used. Finally, we must cite a recent analysis by the COSY collaboration [61] in p-A interactions at $p_{\text{lab}} = 2.83$ GeV/c: the experiment finds a broadening of the in-medium ϕ width of an order of magnitude with respect to the vacuum one.

As we saw, all these experiments select mesons with a $\beta\gamma$ small enough to have a significant chance to decay inside the nucleus. In the high energy regime investigated by NA60, however, this kinematical domain is not easily accessible. In heavy ion collisions, the most relevant variable for selecting mesons mostly sensing the deconfined, expanding medium is transverse momentum; in p-A collisions, where the particles are produced inside a nucleus without any deconfined medium being produced, this aspect must be still investigated. For this reason, the detailed study of the line shapes for the processes involved in the low mass spectrum is not part of the present work

2

The NA60 Apparatus

2.1 General Overview

The purpose of the NA60 apparatus is to accurately study dimuon production in proton-nucleus and heavy ion collisions. The produced dimuons are tracked in the muon spectrometer, preceded by a hadron absorber that lets only muons pass. The stopping of hadrons (provided by more than 20 interactions lengths) allows to select the highly rare dimuon events. In this way, and by implementing a high selective trigger, we can run at very high luminosities (roughly speaking, only one out of 100 thousand collisions are recorded). On the other hand, the material which stops the hadrons also induces multiple scattering and energy loss on the muons, degrading the mass resolution of the measurement made in the spectrometer. To overcome this problem, NA60 already measures the muons *before* the absorber. This requires that the muon tracks are found among the many other charged particle tracks, by a correct matching with the reconstructed tracks in the muon spectrometer. For this reason, the angles and momenta of charged particles must be known in the vertex region with sufficient accuracy, requiring a magnetic field in the target region. The particle tracking in the vertex region is performed using a tracking telescope, made essentially of pixel and a few microstrip silicon detectors.

Figure 2.1 shows an overall representation of the NA60 apparatus. Note that the term "muon spectrometer" designates the detector system which starts with the hadron absorber, including the trigger hodoscopes, while we speak of the "vertex tracking telescope" when we mean the tracking elements in the vertex region. In the following we will use the expressions "Jura" and "Salève" sides, referring to the left and the right sides of the experiment with respect to the central vertical plane, when seen from the beam line looking downstream.

The following sections describe the motivation, the design and performance of the detector components which are important for the analysis presented in this thesis. After a short overview of the beam, we will start with the muon spectrometer, the most important detector in this experiment. The subsequent sections then describe each detector in the sequence in which they are assembled along the beam direction.

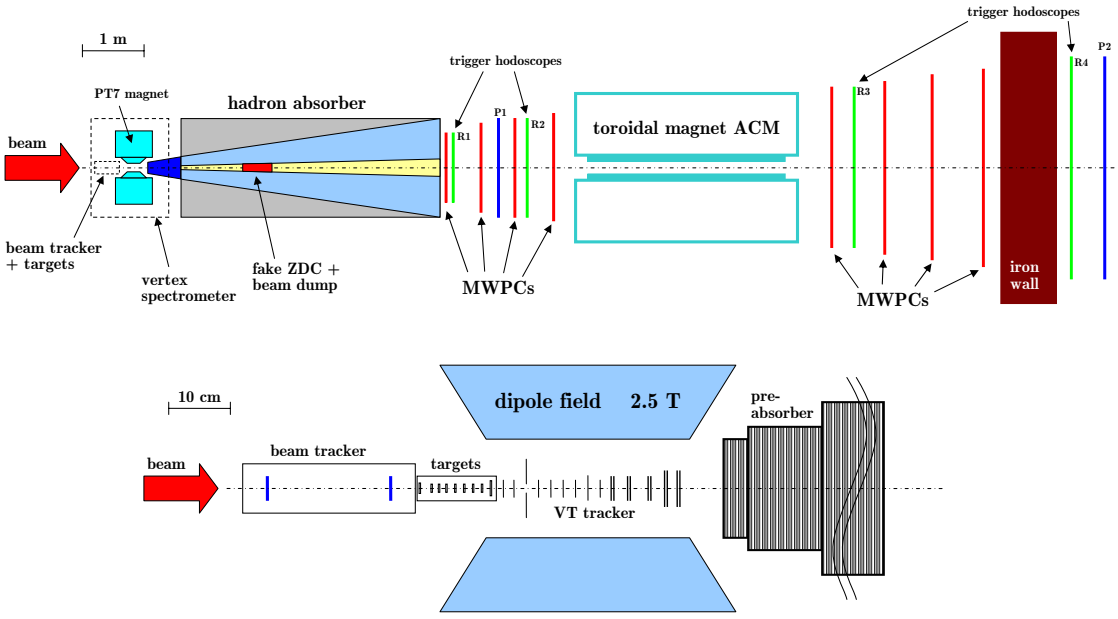

Figure 2.1: *Overall representation of the NA60 apparatus (top) and detail of the vertex region (bottom).*

2.2 The Beam

NA60 collected data with proton and ion beams provided by the CERN SPS accelerator. Ion beams were used in 2002 (test run with a Pb beam of 30 GeV per nucleon followed by 5 days with 20 GeV per nucleon) and in 2003 (In beam of 158 GeV per nucleon incident on In targets), while a 400 GeV proton beam was used both in 2002 (incident on Be, In and Pb targets) and − together with a 158 GeV proton beam − in 2004 (incident on Be, Al, Cu, In, W, Pb and U targets).

At the CERN SPS particles do not circulate in continuous mode, but rather they are delivered during well defined time intervals called “bursts”, separated by “interburts”. In the 2002 and 2004 proton runs, the bursts were ~ 4.8 s long, separated by interburts lasting ~ 12 s [54]. The intensity of the proton beam was different in 2002 and 2004 proton runs: in the former the beam intensity was $\simeq 2 \cdot 10^8$ protons per burst,

while in the latter the beam intensity was approximately ten times higher, amounting to $\simeq 2 \cdot 10^9$ protons per burst, in order to gain as much statistics as possible to allow a study of the rare χ_c meson.

2.3 The Muon Spectrometer and Trigger System

The purpose of the muon spectrometer is to identify, trigger on, and reconstruct the muon pairs produced as a result of the beam-target interactions. In order to achieve this, it consists of four main elements [16]: the hadron absorber, eight tracking multi-wire proportional chambers (MWPC), four trigger scintillator hodoscopes (R1-R4), the last one placed behind a 120 cm thick iron wall, and an Air Core toroidal Magnet (ACM) for the momentum measurement of the muons.

These components can be moved along the z-axis to ease maintenance and to keep the angular muon acceptance around mid-rapidity, in spite of changes in the beam energy. In the current setup, the angular muon acceptance lies approximately in the range 35–120 mrad (from 2° to 7°), as imposed by the magnet aperture. For beam energies of 400 GeV this corresponds roughly to one unit of rapidity at mid-rapidity, where particle production is most copious. The muon's acceptance also depends on the magnetic field settings and on the effective number of interaction lengths of the absorber; it is also affected by the trigger conditions.

2.3.1 The Hadron Absorber

The muons are filtered out among the many other produced particles by the hadron absorber. This is a simple, but effective, "particle identification" system: particles that hit the R4 trigger hodoscope (see Figure 2.1), by definition, are muons. Indeed, apart from neutrinos, only muons are penetrating enough to cross all the matter of which the absorber is made up:

- the pre-absorber, made of 41 cm BeO and 25.4 cm Al_2O_3
- the main absorber, made of 400 cm of graphite followed by 80 cm of iron[1]
- the 120 cm thick iron wall, placed after the muon chambers so as to not degrade the tracking accuracy through multiple scattering, while ensuring a very clean muon trigger

The hadron absorber starts as close as possible to the target region, immediately after the vertex telescope, in order to stop the largest fraction of pions and kaons from decaying into muons and becoming a source of background.

[1] The composition of the main absorber slightly changed during the 2004 proton run, see Chapter 3; here, we refer to the composition in the period of interest for this thesis.

The main absorber, placed between the target and the muon chambers, is made of materials with a low atomic number Z, in order to minimize the multiple scattering induced on the traversing muons, and with the highest available densities, so as to stop the hadrons in a relatively small thickness. The non-interacting protons are stopped in an "Uranium Plug", placed inside the absorber, aligned with the beam axis outside of the muon's acceptance window. The carbon blocks are surrounded by cast iron and concrete. Table 2.1 gives an overview of the position and thicknesses of the elements of the absorber for the data taking period relevant for this thesis (see Chapter 3).

Placing the last part of the absorber − the 120 cm thick iron wall − after the tracking stations and before the last trigger hodoscope, ensures that no energetic punch-through hadrons give rise to a fake trigger, without contributing to the degradation of the tracks measured in the chambers.

Material	ρ [g/cm^3]	z_{in} [cm]	Δz [cm]	λ_I [cm]	$\Delta z/\lambda_I$
BeO	2.81	43.6	41.0	35.85	1.14
Al_2O_3	3.52	84.6	25.4	32.65	0.78
C	1.93	110.0	400.0	44.70	8.95
Fe	7.87	510.0	80.0	16.76	4.77
Total number of interaction lengths in main absorber					15.64
Fe (iron wall)	7.87	1676.3	120.0	16.76	7.16
Total number of interaction lengths					22.8

Table 2.1: *Composition of the hadron absorber for the data taking period relevant for this thesis (see Chapter 3) during the 2004 proton run. λ_I is the nuclear interaction length.*

2.3.2 The Multi-Wire Proportional Chambers

The muons which have crossed the main absorber are tracked in eight multi-wire proportional chambers, separated into two sets of 4 chambers by the toroidal magnet ACM (Air Core Magnet).

Each muon chamber consists of three independent tracking planes, interspaced by 2.2 cm, rotated by 60° with respect to each other, to allow a good measurement of one space point (see Figure 2.2).

The sensing elements of these chambers are gold-plated tungsten anode wires with a diameter of $\sim$ 20 μm, inter-spaced by 3 mm and sandwiched between two graphited Mylar cathode planes, 6 mm far away. The overall read-out gate is $\sim$ 80 ns [16]. The

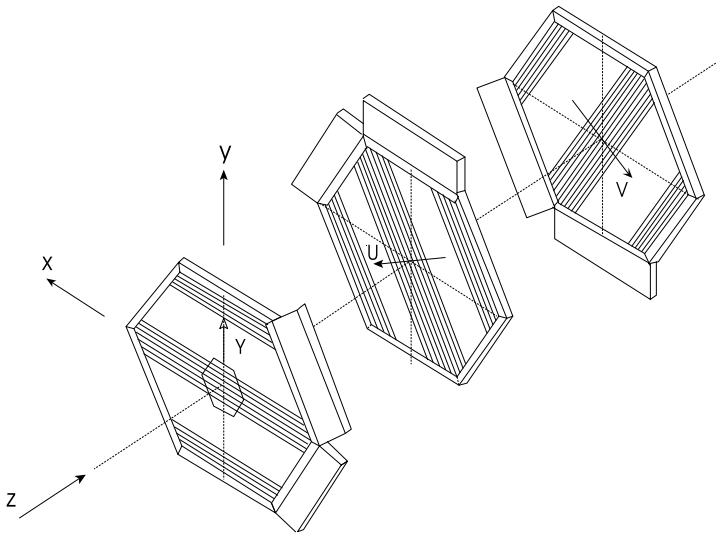

Figure 2.2: *Each MWPC consists of three independent tracking planes. For visibility purposes the individual planes are shown well separated from one another.*

chambers have hexagonal shape and their transverse size increases with increasing distance from the target to cover the angular acceptance, defined by the aperture of the ACM magnet. The z-positions with respect to the target and the transverse size of all components of the muon spectrometer can be found in Table 2.2.

The tracking volume of the chambers is filled with a gas mixture, consisting of $\sim$ 80% of Argon (of which 50% is flushed through 0.8% of Isopropyl alcohol), of 18% Isobutane iC_4H_{10} used as a quencher, and of 2% Tetrafluorethane used as a "cleaning" gas. A gas mixer rack measures and controls the flow of the gas components. Due to the fact that the gas mixture had to be changed in 2002 with respect to the previously used "magic gas", the chambers showed visible "ageing effects"; in particular, 5 planes out of 24 were not working during the data taking period relevant to this thesis [54], see Chapter 3: the track reconstruction could still be performed using the remaining working planes, with a slightly degraded efficiency. It is worth noting that − apart from chamber 1, which was completely rebuilt in 1994 − all MWPCs had been working since 1980, when NA10 (the predecessor experiment of NA38, NA50 and NA60) began to operate.

2.3.3 The Trigger Hodoscopes

The trigger system consists of four "R" hodoscopes, two before and two after the ACM magnet, made of scintillator slabs, see Figure 2.3. Like all other components of the muon spectrometer, the "R" hodoscopes have hexagonal shape, given by the geometry of the ACM magnet. The scintillator slabs of each sextant, oriented parallel to the outer edges, become longer with increasing distance from the beam axis.

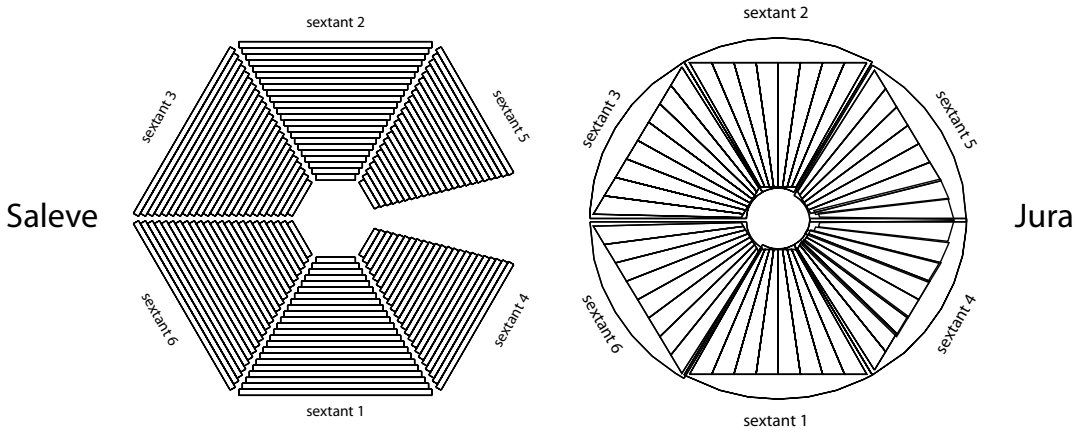

Figure 2.3: *The segmented slabs of the R3 (left) and P (right) hodoscopes.*

The width of the slabs of the R1 and R2 hodoscopes increases with the distance from the beam line so that a muon produced in the target which passes through slab i in R1 will also hit slab i in R2. In order to accommodate the longitudinal spatial extent of the target region (of the order of $\sim$ 1 m in the NA10 experiment, which designated the trigger logic) and to allow for multiple scattering for low energetic muons, the combination of hitting slab i in R1 and $i-1$ in R2 is also allowed. This "R1-R2 coincidence" for each muon is combined with the information from R3 and R4. The last trigger hodoscope, R4, is placed behind the 120 cm thick iron wall, which absorbs remaining hadrons thereby ensuring a clean (di)muon trigger; however, this implies that the muons must have a minimal momentum of $\sim$ 7 GeV/c to give a signal in R4. The dimuon trigger also requires that the two muons pass through two different sextants: this requirement reduces the fraction of low mass muon pairs that give rise to a trigger, in order to not saturate the bandwidth of the data acquisition system. The overall read-out gate of the R-hodoscopes is 20 ns.

The R3 hodoscope has a small inactive zone on the "Jura" side, called "Beam-Killer", as can be seen in Figure 2.3. Although the other trigger hodoscopes have no such dead areas, the muon acceptance is affected by this cut in sextants 4 and 5, since the trigger requires a hit in *all* trigger stations.

The P-hodoscopes

Furthermore, NA60 uses two so-called "P-hodoscopes", P1 and P2. The former is placed before the ACM magnet, the latter after the iron wall. They are used in special runs to measure the efficiency of the R1-R4 system. Their geometry is different from the R-hodoscopes; the scintillator slabs of each sextant are oriented radially, so that their width increases with increasing distance from the beam axis (see Figure 2.3).

In the 2004 proton run an additional feature was implemented: the measure of the arrival time of each muon at the P2 hodoscope; it improves our ability of rejecting

trigger coincidences of 2 muons that were produced in *different* events. In any case, this information has not been exploited in the present analysis, because not available for all the analyzed burts.

Element	z [cm]	**Main Characteristics**
MWPC 1	615.8	448 wires per plane, $\varnothing = 134$ cm
Hod. R1	629.6	6×30 scintillator slabs of 1.05–3.45 cm width
MWPC 2	684.1	512 wires per plane, $\varnothing = 153$ cm
Hod. P1	712.0	6×8 scintillator elements; width: 2.73–13.65 cm
MWPC 3	748.7	576 wires per plane, $\varnothing = 172$ cm
Hod. R2	761.0	6×30 scintillator slabs of 1.25–3.35 cm width
MWPC 4	818.2	640 wires per plane, $\varnothing = 192$ cm
ACM	828.7 – 1311.7	
MWPC 5	1347.2	1024 wires per plane, $\varnothing = 306$ cm
Hod. R3	1390.2	6×23 scintillator slabs of 5.5 cm width
MWPC 6	1445.6	1088 wires per plane, $\varnothing = 326$ cm
MWPC 7	1544.1	1152 wires per plane, $\varnothing = 345$ cm
MWPC 8	1642.1	1216 wires per plane, $\varnothing = 364$ cm
Iron wall	1676.3 – 1796.3	
Hod. R4	1800.7	6×32 scintillator slabs of 5.5 cm width
Hod. P2	1820.7	6×8 scintillator elements; width: 8.10–47.50 cm

Table 2.2: *Detector components of the muon spectrometer. Except for the ACM and iron wall, the z values given refer to the center of the respective device.*

2.3.4 The Toroidal Magnet ACM

The magnetic field of the toroidal magnet ACM is produced between 6 radial iron poles, which are 4 m long and cover 18° in azimuth. The magnet's air gap starts at a radius of 29.5 cm, while the outer radius is 154 cm. These two values are the ones determining the detector's rapidity acceptance. Events with muons which cross one of the iron pieces are rejected from the physics analysis, since they have degraded momentum resolution, compared to the ones which traverse the air core between

them. The toroidal magnetic field is $1/r$ dependent, according to the relation:

$$\vec{B}(r) = B_0/r \cdot \vec{e}_\phi \ .$$

In Figure 2.4 we can see the magnitude of the magnetic field in the air sectors for different distances from the beam-axis. The proportionality constant between the magnitude of the magnetic field and the radius is $B_0 = 0.219$ T·m for a current of 4000 A, as used for the data taking period relevant for this thesis. The ACM current is pulsed, synchronized with the SPS cycle, and is recorded burst by burst.

The bending power depends on the radial distance from the beam. Since the axis of the magnet is aligned along the beam axis, the muons keep their azimuthal angle while changing their polar angle. The ACM magnet was designed such that the deflection angle, $\Delta\theta$, is inversely proportional to the particle's p_T, as explained in [49].

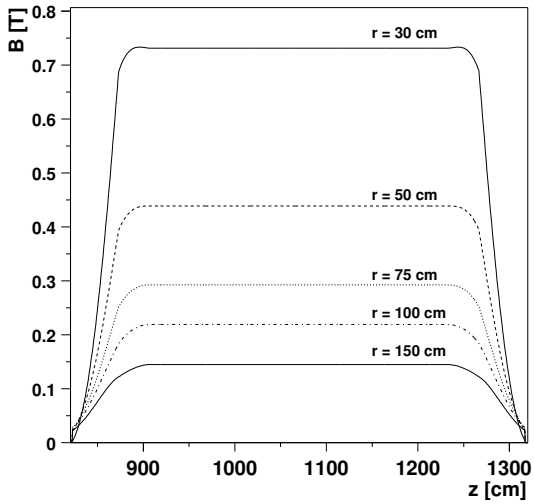

Figure 2.4: *Magnitude of the toroidal field for various distances from the beam axis.*

2.4 The Target System

The NA60 experiment used different target systems in proton and ion runs. In ion runs, in order to have a symmetric collision system, indium targets were used with the indium beam, and lead targets with the lead beam.

In the proton runs, one of the physics topics of interest is the study of the nuclear dependence of the production cross-section of various particles, hence different target materials were used. In the 2002 proton run, targets of beryllium, indium and lead were used; in 2004 aluminum, copper, tungsten and uranium targets were used additionally.

Placing these different targets simultaneously into the beam allows to minimize systematic errors coming from luminosity calculations, which will affect all the targets

in the same way. In order to distinguish the particular sub-target from which the muons originate, the various sub-targets are well separated along the beamline.

The target system used in the 2004 proton run, composed of 9 disk-shaped sub-targets, is represented in Figure 2.5. The position, thickness and diameter for each sub-target are reported in Table 2.3. The need of forcing the conversion $\gamma \to e^+e^-$ in the study of the process $\chi_c \to J/\psi + \gamma$ justifies the use of a Pb target having an exceptionally large diameter, 2 cm, placed downstream of all other targets, such that a sizable fraction of the photons produced in the upstream targets (as well as those produced in the Pb target itself) are converted into electron-positron pairs when going through the disk, which can be tracked in the vertex telescope.

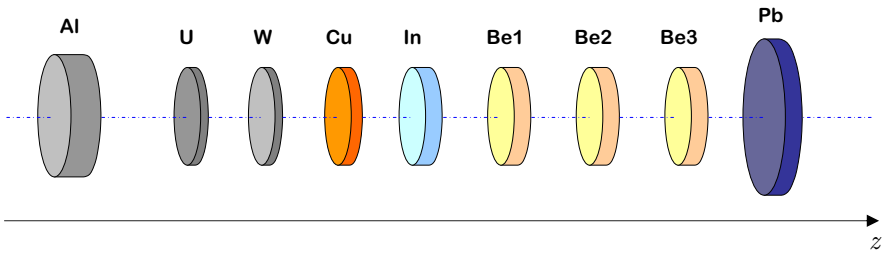

Figure 2.5: *Target system used in the 2004 proton run.*

Tgt. ID	Material	A	z [cm]	Δz [cm]	$\varnothing$ [cm]	λ_I [cm]	$\Delta z/\lambda_I$
0 (Al)	Aluminium	27	−8.15	0.3990	1.5	39.4	0.0101
1 (U)	Uranium	238	−6.65	0.0890	1.2	10.5	0.0085
2 (W)	Tungsten	184	−5.85	0.0965	1.2	9.59	0.0101
3 (Cu)	Copper	64	−5.05	0.1470	1.2	15.1	0.0097
4 (In)	Indium	115	−4.25	0.1990	1.2	23.0	0.0087
5 (Be1)	Beryllium	9	−3.25	0.1940	1.2	40.7	0.0048
6 (Be2)	Beryllium	9	−2.25	0.1930	1.2	40.7	0.0047
7 (Be3)	Beryllium	9	−1.25	0.1940	1.2	40.7	0.0048
8 (Pb)	Lead	208	−0.25	0.2000	2.0	17.1	0.0117
					Total number of interaction lengths		0.0751

Table 2.3: *Sub-targets forming the target system in 2004 proton run. The z values given refer to the center of the respective target.*

2.5 The PT7 Dipole Magnet

To measure the particles' momenta in the vertex region, the silicon tracking telescope is placed in the gap of a dipole magnet, called PT7. Its dimensions can be seen in Figure 2.6. When operated at 900 A, close to its maximum value, the PT7 magnet allows to obtain a magnetic field of 2.5 T.

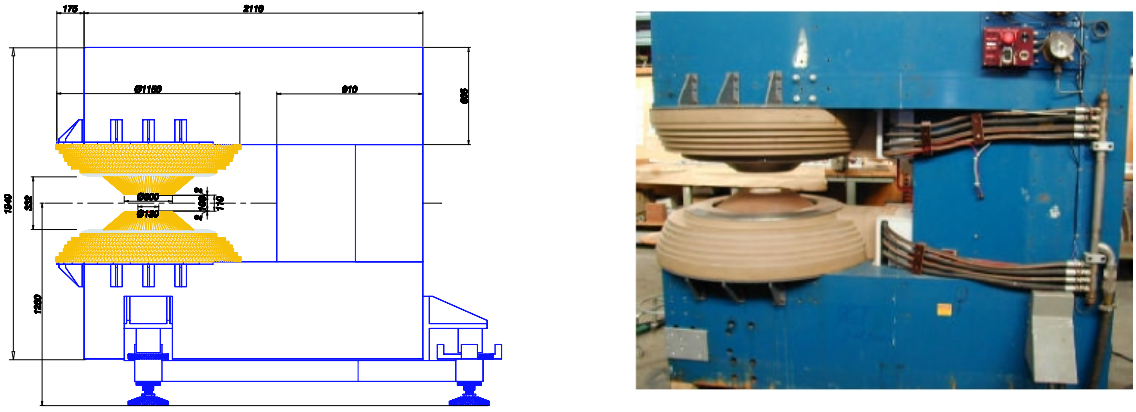

Figure 2.6: *Front view of the PT7 magnet, as seen from the incoming beam.*

Special care was taken in the design of the surface of the pole shoes, by means of specially designed "shims", to ensure that the magnetic field is highly homogeneous. Figure 2.7 shows the magnitude of the magnetic field in the $x-z$ plane, measured at the centre of the vertical gap: the rotational symmetry around the y axis is clearly visible, together with the plateau of the field in the centre of the magnet.

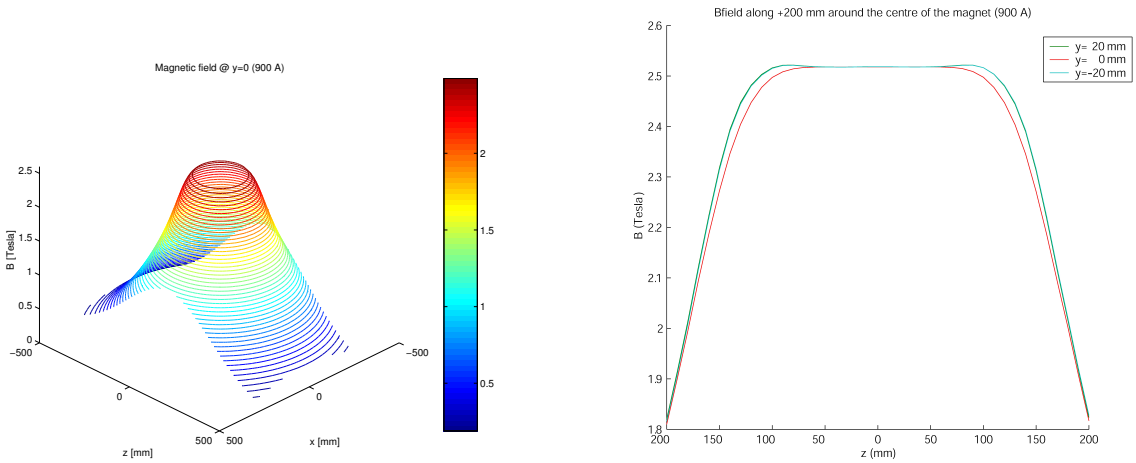

Figure 2.7: *PT7 magnetic field measured in the centre of the gap, with a current of 900 A.*

The magnetic field was carefully measured with a Hall probe in steps of 1 cm in each of the three axes. These measurements were parameterized and inserted into the NA60 detector simulation package, NA60root. Due to the dipole symmetry, it suffices to consider two components: the vertical component B_y and the radial component B_r in the $x-z$ plane. A simple bilinear interpolation of the measured values was used to describe the field.

To reduce systematic uncertainties, the polarity of the magnet is reversed every few runs. During the field mapping, it was verified that reversing the polarity leads to deviations of the magnetic field, if any, of smaller than 0.2%.

2.6 The Vertex Tracking Telescope

The purpose of the vertex tracking telescope is to track the secondary particles, including muons, produced as a result of an interaction in the target, before they enter in the hadron absorber. Out of the many uninteresting particles, the muons have to be unambiguously identified by matching with the tracks reconstructed in the spectrometer.

Apart from improving the mass resolution of the reconstructed dimuons, the tracking telescope in the vertex region allows us to "identify" the sub-target where the interaction took place, by finding the common origin of the reconstructed tracks.

NA60 uses both silicon microstrip and silicon pixel technology for the tracking elements in the target region. In the 2002 proton run, the low charged particle multiplicities allowed the use of microstrip detectors, while the much higher particle densities reached in heavy ion collisions imposed in 2003 the exclusive use of silicon pixel detectors. The microstrip and pixel planes were designed to fit in the gap of the PT7 magnet and to match the muon spectrometer's angular acceptance.

Unlike in 2002, in 2004 the vertex telescope (VT) was composed mainly of silicon pixel planes. The reason is due to the intensity of the proton beam used in 2004, which was chosen to be 10 times higher than the intensity in 2002: the increased intensity involves an increase of the occupancy in the vertex telescope, and demands the use of pixel sensors having a higher granularity than the microstrips. Furthermore, the analysis conducted on the 2002 and 2003 data has shown that pixel chips offer a slightly higher efficiency than the microstrip sensors. The use of *analog* microstrips, however, allows to have a much higher time resolution, of the order of 5 ns to be compared with the 2×100 ns and 2×25 ns read-out windows of the ALICE and ATLAS pixels, see below. For this reason, even in the 2004 high-intensity proton run the vertex telescope contained 4 microstrip sensors placed at the very end, where smaller granularity is needed.

The Setup

As will be outlined in the next chapter, the p-A data collected during the 2004 run consist of six parts, all relative to the same system of Be, Al, Cu, In, W, Pb and U sub-targets. The data taking conditions for these six periods differ from each other due to the following changes in experimental setup:

- the energy of the proton beam
- the composition of the first two tracking stations of the vertex telescope
- the thickness of the iron block sitting at the end of the main absorber, just before the multi-wire proportional chambers

As the present work is devoted to the analysis of p-A data collected during the fifth period (400 GeV proton beam, runs 11580–11804), we will only describe the corresponding setup of the vertex telescope; this setup is represented in Figure 2.8, from which 14 tracking stations can be distinguished:

- 7 stations composed of 1 small ALICE pixel plane (small ALICE stations)
- 2 stations composed of 2 ATLAS pixel planes (ATLAS stations)
- 3 stations composed of 2 large ALICE pixel planes (large ALICE stations)
- 2 stations composed of 2 BNL microstrips planes (BNL stations)

Each type of station is described in the following. The setup of the tracking stations forming the vertex telescope is summarized in Table 2.4.

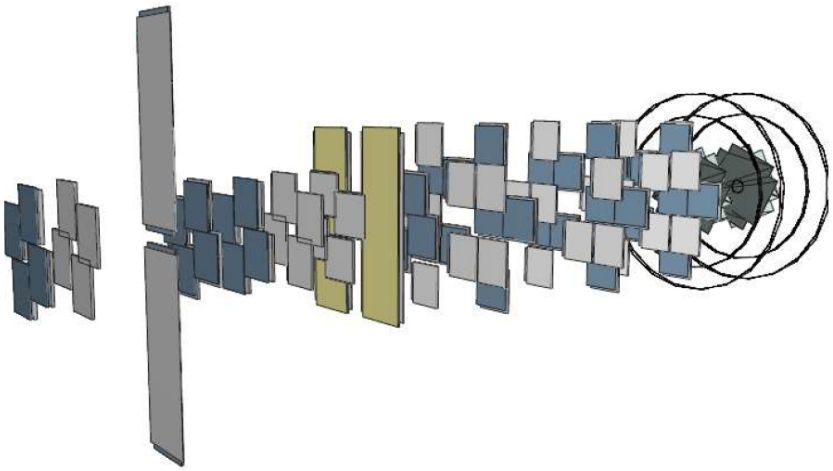

Figure 2.8: *Vertex telescope used in the run period relevant to this thesis (runs 11580–11804), see Chapter 3.*

The vertex telescope was cooled by means of a closed-circuit system with a fluorcarbon (C_6F_{14}) coolant circulating in the detector planes' cooling pipes, in order to reduce radiation damage and minimize leakage current of the silicon detectors. A custom-built, high performance refrigerator cooled and pumped the fluorcarbon through the circuit; temperatures as low as -10° C were measured on the hybrids supporting the pixel chips, with no appreciable fluctuations. To avoid condensation, the whole vertex telescope was enclosed in a protective bag, permanently flushed with nitrogen, tailored *in situ* to fit the tight and convoluted geometry of the vertex region.

The ALICE Pixel Planes

The small ALICE tracking planes, forming the small tracking stations, consist of 4 rectangular chips placed around a beam hole. Because of their small transverse dimensions they are used only in the first section of the vertex telescope, closer to the target region, where they still cover the muon spectrometer geometrical acceptance. The large tracking stations are composed of two large ALICE planes, each made of 8 chips. To improve the muon acceptance coverage, a small pixel plane is placed close to the first large station, to cover its beam hole; during the data taking period relevant to this thesis, this plane never provided any signal, although physically having been present and, hence, contributing to multiple scattering and energy loss to the particles traversing it.

Both small and large tracking planes use the same type of chip. Each chip has 8 192 pixels with an area of 425×50 μm^2, arranged in a matrix of 32 columns and 256 rows, giving a total active area of 13.6×12.8 mm^2. Within a given plane, all chips are mounted with the same orientation, defining the plane as X or Y, depending on the orientation of the 50 μm side. To cover the full angular acceptance, some planes are inverted upside-down, having their back side facing the beam [25].

A pixel chip assembly is a 750 μm thick ALICE1LHCB pixel read-out chip [80] bump-bonded to the 300 μm pixel sensor chip. These chips operate at a frequency of 10 MHz; however, since the dimuon trigger is asynchronous with respect to the chip's clock (i.e. the dimuon trigger can come at any moment with respect to the clock), we must record two clock cycles whenever there is a trigger, to ensure fully efficient tracking. Hence, the total read-out gate is 2×100 ns.

Such pixel chip assemblies are glued on BeO or Al_2O_3 hybrids, which are placed on printed circuit boards (PCBs) to route the electrical lines out of the magnet's gap. A zoomed view of a 4-chip plane and a fully assembled 8-chip plane can be seen in Figure 2.9. The PCBs are mounted on aluminum frames for mechanical support, and placed in the slots of a support box that slides in the magnet gap.

It is worth noting that most of these planes were already used in the 5-weeks long 2003 run, where they accumulated considerable radiation doses from being exposed to the secondary particles produced in the indium-indium collisions. It has been estimated that, by the end of that run, the innermost detector regions, closest

to the beam axis, integrated a radiation dose equivalent to a total fluence of more than 10^{13} 1 MeV neutrons per cm^2 [24] (an order of magnitude higher than the doses these pixels are expected to accumulate after 10 years of operation in the ALICE experiment at the LHC). At the end of 2003, the most exposed planes reached depletion voltages of 150 V compared to the 40 V needed before type inversion. In order to use these planes again in the 2004 run, expected to provide a total fluence at least as high as that of 2003, it was clearly crucial to operate them at low temperatures, to decrease their leakage current and their needed depletion voltage. This implied the development of a new cooling system, a highly non-trivial operation [54].

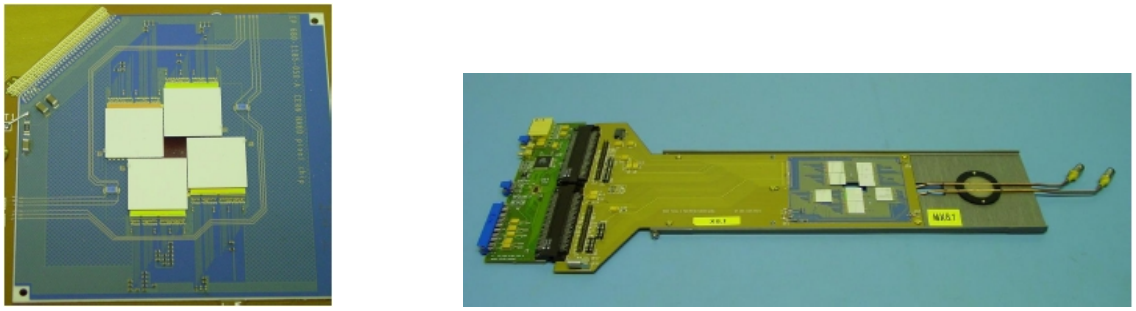

Figure 2.9: *Zoomed view of a 4-chip plane, showing the sensor and read-out chips mounted on the ceramic hybrid (left) and a fully assembled 8-chip plane (right).*

The ATLAS Pixel Planes

The four ATLAS pixel sensors [11] were arranged in two physical tracking planes to maximize their angular acceptance. The downstream plane is shown in Figure 2.10.

From a technical point of view, each ATLAS pixel module contains a single sensor chip with an active area of 16.4 × 60.8 mm^2, connected to 16 read-out chips. The sensor area is divided into 328 × 144 pixels with a size of 50 × 400 μm^2 (16 of 144 columns are 600 μm wide to bridge the gap between neighboring front-end chips). The modules were glued on a 500 μm thick carbon fiber plate and mounted on a support frame similar to those of the ALICE pixel planes.

The ATLAS pixel read-out chips operate at 40 MHz. The 2-clock-cycle window, giving a total read-out gate of 2 × 25 ns, is imposed by the asynchronous trigger, as was already discussed for the ALICE pixel planes. It is worth to note that the total read-out gate of the ATLAS pixel planes is four time smaller than the read-out gate of the ALICE pixel planes: the existence of the ATLAS tracking planes effectively plays a crucial role, because it allowed the experiment to run at four times higher beam intensities than with only ALICE pixel planes; thus, we could collect more statistics for the same amount of beam time. In particular, taking into account the ATLAS pixel read-out and assuming a Poissonian distributed arrival of beam protons, it can

be shown [50] that only at beam intensities around $2 \cdot 10^9$ protons per 4.8 s burst we reach the limit of two pile-up collisions on top of the one which gave the trigger, given the $\sim 10\%$ λ_{int} thickness of the target system; at such collision rate, the ALICE pixel detector integrate, on average, tracks from 9 different proton-nucleus collisions in their 2×100 ns read-out window (a detailed calculation of the expected pile-up in 2004 proton run is presented in [74]). During the data reconstruction we, hence, must require that a track leaves a hit in the ATLAS pixel planes, in order to reject tracks produced in pile-up interactions outside of the ATLAS planes' 2×25 ns read-out gate; on the other hand, this effectively limits the vertex telescope's geometrical acceptance to the one given by the ATLAS pixel planes.

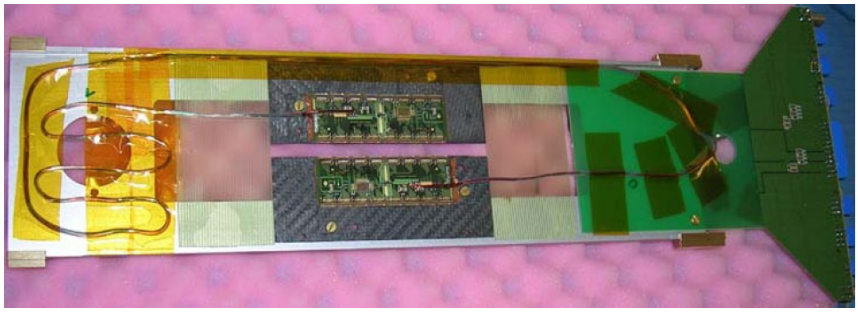

Figure 2.10: *The downstream ATLAS pixel plane. The two modules, mounted on a carbon fiber plate, are visible at the center of the picture, above and below a gap left free to let the non-interacting beam pass through.*

The BNL Microstrip Sensors

The BNL microstrip detector planes were already successfully operated during the 2002 proton run [77]. Each sensor provides the positions of the hits in one dimension. In order to obtain one space points, each microstrip tracking station consists of two microstrip sensor planes assembled back to back, which have an inclination angle of $\pm 25^\circ$ with respect to the vertical axis y. This inclination optimizes the particle tracking in the magnetic field of the PT7, oriented in the y direction.

The BNL microstrip planes are built from 4-inch silicon sensors, with 12×128 strips arranged such as to keep the occupancy below 3% for p-Pb collisions in case of single interactions without pile-up. The BNL sensors were designed with the strips arranged in two regions, the inner one, surrounding the beam hole, and the outer one, of longer strips and only used for the planes placed far from the target. The inner region is sufficient to cover the angular acceptance of the muon spectrometer in the planes closer to the target and, in fact, only the strips in that region, for those planes, were used in the track reconstruction of the 2002 data. Contrary to the other

silicon detectors used in the 2004 proton run, the BNL microstrip planes do not have any inactive area − apart from the beam hole.

The transverse dimensions of the active area of the BNL microstrip sensors still cover the angular acceptance at $\sim$ 40 cm from the target, allowing to profit the full range of the magnetic field over which it is roughly constant. In this way we can increase the vertex telescope's lever arm for momentum determination. Furthermore, at these large distances from the target the coarser granularity of the sensors' outer region is highly sufficient for particle tracking.

The BNL microstrip detectors are sampled at 40 MHz (i.e. every 25 ns) and four analog samples are read out when a trigger arrives. With respect to 2002, a new feature was added at the the read-out level, namely a TDC, leading to an improved timing accuracy of $\lesssim$ 5 ns if correctly calibrated. Although the BNL microstrip sensors have an efficiency lower than the one of the pixels (95% versus 90% on average) they should further help to improve the validation of "in time" tracks, i.e. those tracks which are produced "in time" with the collision that gave rise to the trigger.

Station ID	**Sensing elements**	z **Pos.** [cm]	**Read-out gate**
0	4 ALICE pixel chips	5.68	2×100 ns
1	4 ALICE pixel chips	6.91	2×100 ns
2	2 ATLAS pixel chips	9.37	2×25 ns
3	4 ALICE pixel chips	10.60	2×100 ns
4	4 ALICE pixel chips	12.22	2×100 ns
5	4 ALICE pixel chips	13.90	2×100 ns
6	4 ALICE pixel chips	15.47	2×100 ns
7	2 ATLAS pixel chips	16.73	2×25 ns
8	4 ALICE pixel chips	18.76	2×100 ns
9	$8 + 8$ ALICE pixel chips	20.39 ; 22.01	2×100 ns
10	$8 + 8$ ALICE pixel chips	22.67 ; 28.28	2×100 ns
11	$8 + 8$ ALICE pixel chips	31.75 ; 33.28	2×100 ns
12	2 BNL microstrip sensors	35.92 ; 36.09	4×25 ns
13	2 BNL microstrip sensors	39.92 ; 40.09	4×25 ns

Table 2.4: *Tracking stations forming the vertex telescope used in the run period relevant to this thesis (runs 11580–11804), see Chapter 3.*

3

Data Taking and Event Selection

3.1 Overview of the Six Data Taking Sub-Periods

As mentioned in the previous Chapter, the p-A data collected during the 2004 proton run consist of six sub-periods. The data taking conditions for these sub-periods differ from each other due to the following changes in experimental setup:

- the energy of the proton beam
- the composition of the first two tracking stations of the vertex telescope
- the thickness of the iron block at the end of the main absorber, just before the multi-wire proportional chambers

The data are collected in several independent runs, each taken under the same experimental conditions; each run contains several bursts, and each burst consists of several triggers.

In the following we will give an overview of the characteristics of the data taking sub-periods, summarizing them in Table 3.1. In the next section we will instead focus on sub-period 5, on which this work is based. Most of the other sub-periods are not yet reconstructed and, hence, presently not available for physics data analysis; their description only serves for reference purposes, and may be peacefully skipped if not specifically interested to it.

The First Sub-Period: Runs 10015–10116

The first sub-period useful for data analysis lasted from 2004/09/17 to 2004/09/20, giving 102 runs, corresponding to $\sim 4\,600$ bursts and $\sim 6.3 \times 10^6$ triggers.

In this sub-period a 400 GeV proton beam was used. The corresponding setup of the vertex telescope is shown in Figure 3.1; the first two tracking stations were composed of an ATLAS and a BNL microstrip station, respectively. The iron block at the end of the main absorber was 40 cm thick.

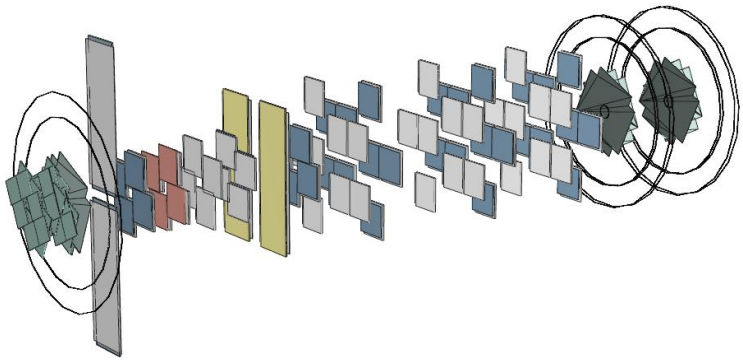

Figure 3.1: *Setup of the vertex telescope used in the first sub-period (runs 10015–10116).*

The Second and Third Sub-Periods: Runs 10117–10361 and Runs 10380–11187

The second sub-period lasted from 2004/09/20 to 2004/09/24, giving 245 runs corresponding to $\sim$ 9 900 bursts and $\sim 5.2 \times 10^6$ triggers. Also in this sub-period a 400 GeV proton beam was used. The corresponding setup of the vertex telescope is shown in Figure 3.2; the first two tracking stations were composed of an ATLAS microstrip station and a small ALICE pixel station, respectively. The iron block at the end of the main absorber was still 40 cm thick, as in the first sub-period.

The third sub-period lasted from 2004/09/24 to 2004/10/13, giving 808 runs corresponding to $\sim$ 30 700 bursts and $\sim 24.7 \times 10^6$ triggers. This sub-period shares with the second one the setup of the vertex telescope, as well as the beam energy; the only difference is the thickness of the iron block at the end of the main absorber, which on the 24$^{\text{th}}$ of September was increased from 40 to 80 cm, in order to reduce the occupancy in the muon spectrometer. The thickness of the iron block was not further changed in the subsequent data taking sub-periods. This increased absorber thickness was needed because of another wire broken in one of the planes of a MWPC placed between the absorber and the ACM magnet (the section in the muon spectrometer where the occupancies are higher), which forced to switch off the plane for further data taking. During the same sub-period, another plane stopped working in a MWPC placed *after* the ACM magnet, but this accident did not involve any change in the setup of the apparatus. No further planes had problems in the rest of the run, but it is worth mentioning that three planes were already switched off at the beginning of the first sub-period. We, thus, had three dead planes out of 24 in sub-periods 1–2; four and then five in the sub-period 3; five in sub-periods 4–6 [54].

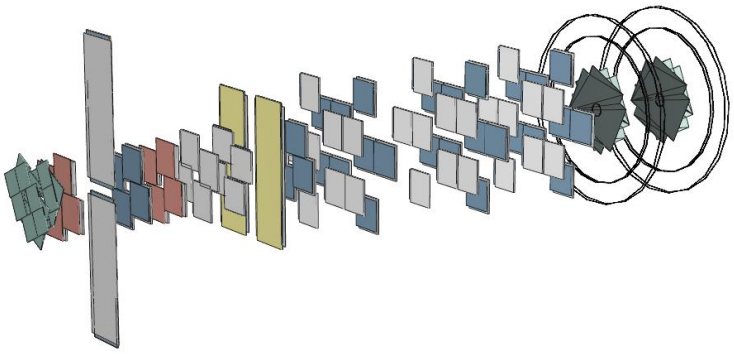

Figure 3.2: *Setup of the vertex telescope used in the second (runs 10117–10361) and the third (runs 10380–11187) sub-periods.*

The Fourth and Fifth Sub-Periods: Runs 11234–11559 and Runs 11580–11804

The fourth sub-period lasted from 2004/10/13 to 2004/10/18, giving 326 runs corresponding to $\sim 14\,000$ bursts and $\sim 11.3 \times 10^6$ triggers. This sub-period is the only one in which a 158 GeV proton beam was used, in order to extract the normal nuclear absorption cross-section of the J/ψ at 158 GeV; this allows a *direct* comparison with the heavy-ion data (Pb-Pb and In-In) collected at 158 GeV per nucleon without a rescaling to the lower energy. The setup of the vertex telescope used in this sub-period was also used in data taking sub-period number 5, the one of interest for this thesis. It was described in detail in Chapter 2, see Table 2.4. From Figure 2.8 we see that the first two tracking stations were now both composed by small ALICE pixel stations.

The fifth sub-period lasted from 2004/10/19 to 2004/10/21; the only difference with respect to sub-period 4 is the use of a 400 GeV proton beam. The run and burst selection for this period has been extensively discussed in [74]; the corresponding statistics is based on 225 runs, corresponding to $\sim 10\,600$ bursts and $\sim 12.9 \times 10^6$ triggers, representing $\sim 1/10$ of the full statistics collected at 400 GeV.

It is due to the fact that the ATLAS microstrip sensors were not used, that these two sub-periods are the only ones whose data are already reconstructed.

The Sixth Sub-Period: Runs 11805–12888

The sixth sub-period lasted from 2004/10/22 to 2004/11/15, giving 1084 runs, corresponding to $\sim 55\,600$ bursts and $\sim 49.0 \times 10^6$ triggers. This sub-period represents the largest statistics, but its data are not yet reconstructed.

The vertex telescope setup used in the sixth sub-period is the one originally foreseen for the whole 2004 proton run, and is shown in Figure 3.3. In this setup the first two tracking stations are both composed of ATLAS microstrip modules, chosen because they are more adapted in detecting the e^+e^- tracks, resulting from the conversion of the photon produced in the process $\chi_c \rightarrow J/\psi + \gamma$, whose study was

intended to be one of the main topics of the 2004 proton run; their material budget, much smaller than that of the ALICE pixel modules, induces as little multiple scattering as possible when the electrons traverse the first tracking stations.

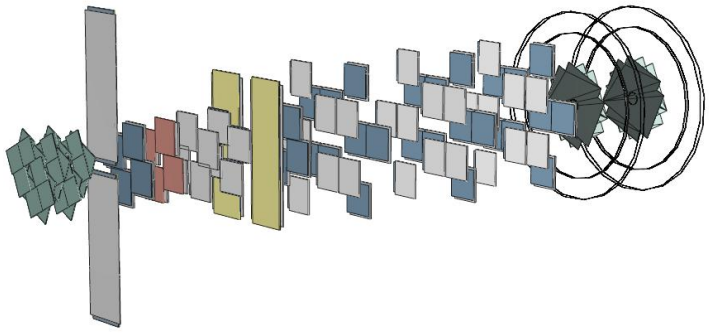

Figure 3.3: *Setup of the vertex telescope used in the last (sixth) sub-period (runs 11805–12888).*

3.2 Data Reconstruction for the Runs 11580–11804

The data reconstruction procedure begins by decoding the recorded raw data (analog or digital detector signals) into a hit map of the individual sub-detector elements (strip planes, trigger hodoscopes, multi-wire proportional chambers, ...). The data reconstruction of the digitized and clusterized data is then performed in several steps. Since the number of tracks after the hadron absorber is significantly smaller than in the vertex region, the tracks in the muon spectrometer are reconstructed first. Only if at least two muons were found, whose origin is in the target region, the track reconstruction in the vertex telescope is performed.

If at least two tracks in the vertex telescope were found, the event reconstruction proceeds via fitting the vertices of the found tracks. The matching of the muons coming from the muon spectrometer, to candidate tracks in the vertex telescope, proceeds by taking into account the multiple scattering and energy loss of the muons in the hadron absorber.

In the following, several abbreviations will be used, which are explained here. The Vertex Telescope is often referred to as VT. We also use the expression VT tracks to refer to tracks reconstructed in the VT telescope. The muon spectrometer is named shortly PC telescope, PC standing for Proportional Chambers. PC muons and PC dimuons are those muons and dimuons which are reconstructed using the PC telescope's information only. On the other hand, VT muons and VT dimuons are fully reconstructed muons and dimuons, which are first reconstructed in the PC telescope and then matched to reconstructed tracks in the vertex telescope. Furthermore, OS

Per.	Beam En.	Start – Stop	Triggers	Remarks
1	400 GeV	2004/09/17 2004/09/20 runs 10015 – 10116	6.3×10^6	Absorber: 40 cm Fe VT 0: ATLAS miscrostrip VT 1: BNL miscrostrip 3 MWPC planes switched off
2	400 GeV	2004/09/20 2004/09/24 runs 10117 – 10361	5.2×10^6	Absorber: 40 cm Fe VT 0: ATLAS miscrostrip VT 1: ALICE pixel 3 MWPC planes switched off
3	400 GeV	2004/09/24 2004/10/13 runs 10380 – 11187	24.7×10^6	Absorber: 80 cm Fe VT 0: ATLAS microstrip VT 1: ALICE pixel 4/5 MWPC planes switch. off
4	158 GeV	2004/10/13 2004/10/18 runs 11234 – 11559	11.3×10^6	Absorber: 80 cm Fe VT 0: ALICE pixel VT 1: ALICE pixel 5 MWPC planes switched off
5	400 GeV	2004/10/19 2004/10/21 runs 11580 – 11804	12.9×10^6	Absorber: 80 cm Fe VT 0: ALICE pixel VT 1: ALICE pixel 5 MWPC planes switched off
6	400 GeV	2004/10/22 2004/11/15 runs 11805 – 12888	49.0×10^6	Absorber: 80 cm Fe VT 0: ATLAS microstrip VT 1: ATLAS microstrip 5 MWPC planes switched off

Table 3.1: *Characterization of the six data taking sub-periods.*

dimuon stands for Opposite-Sign ($+-$) and LS for Like-Sign ($++$ and $--$) muon pairs.

3.2.1 Track Reconstruction

Track Reconstruction in the Muon Spectrometer

The data of the muon spectrometer are the first to be reconstructed, when processing the dimuon sample, because after the hadron absorber the charged particle multiplicity is much lower. As seen in Chapter 2, the spectrometer consists of two sets of 4 stations, which are called the "forward" and the "backward" PC telescopes. The toroidal magnetic field bends charged particle tracks only within the magnet itself, so that in the telescopes the reconstructed tracks are straight lines. The reconstruction is done independently in the two sub-telescopes, and the results are matched in a second step. The toroidal magnet only changes the polar angle of the tracks, leaving the azimuthal angle unchanged: the matching of tracks in the forward and backward telescopes relies on this feature.

Tracks in the backward spectrometer are reconstructed first: in the MWPCs after the ACM magnet the multiplicity is lower, as the contribution from residual hadronic showers is suppressed by the applied magnetic field. Tracks that would cross the iron poles of the magnet are discarded in order to have a sample of muons which all suffered the same minimum amount of multiple scattering and energy loss. Tracks that would miss to leave a hit in the R3 and R4 trigger hodoscopes are also discarded, since they cannot be the real trigger muons. The same procedure is then applied to tracks in the forward telescope (including the cross-check on the trigger hodoscopes), which are finally matched to backward tracks, on the basis of their distance at the center of the magnet and on the difference between their azimuthal angles.

After the two PC muons kinematics are fully reconstructed, it is checked if the formed pair produces a dimuon trigger (the NA60 trigger logic requires that the two trigger muons must be in different sextants); should that not be the case, the event is rejected. This cut not only select candidates satisfying the trigger logic, but also ensures that the two tracks are formed within the 20 ns wide read-out gate of the hodoscopes, being sufficiently smaller than the one of the MWPCs ($\sim$ 80 ns).

Track Reconstruction in the Vertex Telescope

The algorithm used to reconstruct tracks in the vertex detector is a *brute force* algorithm, which tries to build tracks out of all clusters in the telescope. In order to reduce the combinatorics the algorithm is applied in several steps, as described below.

Detector stations are organized in mandatory groups, such that at least one station from each of these groups must contribute to each track; with the BNL microstrip stations not yet aligned, we are left with tracking stations 0–11 (see Table 2.4). Four mandatory groups are defined as follows:

- stations 1, 3, 5 and 8
- stations 0, 4 and 6
- stations 2 and 7
- stations 9, 10 and 11

The first two groups contain the seven small ALICE pixel stations. The third group is composed of the two ATLAS pixel stations: the request of a hit coming from at least one of these two stations ensures that only tracks formed within the 2×25 ns read-out gate of the ATLAS planes are reconstructed (for a demonstration of cleaning up the event by tracks reconstructed from clusters "out of time", see Figure 3.4). Finally, the fourth group is composed of the three large ALICE pixel stations. The composition of the mandatory groups is tuned such that only tracks are reconstructed whose hits are distributed over a reasonably long distance. Moreover, the reconstruction algorithm requires a track to consist of at least 6 hits.

The reconstruction algorithm takes into account the magnetic field of the dipole magnet PT7: at least 3 space points are required in order to reconstruct a track without ambiguity. The reconstruction algorithm, hence, starts by defining a "track seed", composed of three clusters:

- a cluster from one of the stations in the upstream group is paired with a cluster from one of the downstream stations. They are connected with a straight line in the non-bending plane and a relaxed cut is applied on whether this track points to the target region or not;
- the algorithm defines a coarse "road width" by assuming a maximum positive and negative curvature, as given by a 1 GeV particle: a new cluster is then searched inside this path. If it is found, the first "track seed" is formed and a first fit is performed: very loose cuts on the χ^2 and on the vertex position are applied to this fit.

If this first "track seed" passed the preliminary cuts, new clusters from the other stations are added, looking for the ones which fall inside the road width defined by the track seed. A new cluster is added to a track seed only if: (i) its χ^2-distance from the track seed is reasonably low ($\chi^2 < 4.0$); (ii) if the χ^2 of the new track is good enough ($\chi^2_{\text{track}} < 2.2$); (iii) if the extrapolation of the new track to the vertex region is close enough to one of the targets.

The final track, fitted using a "Kalman filter" algorithm, is accepted if it has a cluster in all the mandatory groups of stations and if its length is above the predefined minimum of 6 hits. Moreover, the algorithm checks how many clusters it shares with already accepted tracks; at most, one shared cluster is allowed: in case of conflict, the track with the largest number of cluster or with the best χ^2 is kept.

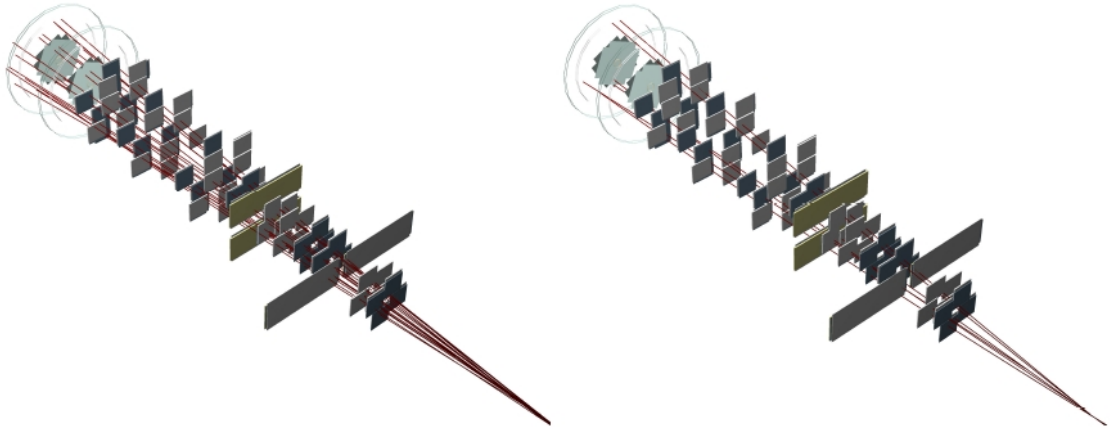

Figure 3.4: *Pile-up rejection in the vertex telescope using the ATLAS pixel as mandatory tracking planes in the track reconstruction. For the same event we plot all tracks (left) and tracks which have a hit in (at least) one of the two ATLAS pixel panes (right).*

3.2.2 Dimuon Track Matching

The matching of a reconstructed dimuon from the muon spectrometer to two track candidates in the vertex telescope proceeds in the following way. For each PC muon the algorithm looks for the matching VT track, among VT tracks with the same charge as the PC muon. In addition, only VT tracks with roughly the same kinematics of the PC muon are considered as matching candidates; this requirement implies that the slopes (k_x and k_y) and the curvatures (C) of the candidate VT track and of the PC muon − corrected for multiple scattering and energy loss in the hadron absorber − should be similar: that is, the comparison is done both in angular and momentum space. Technically, this comparison is performed applying a cut on the χ^2 of the match, defined as:

$$\chi^2_{\text{match}} = \left(\frac{\Delta k_x}{\sigma_{k_x}}\right)^2 + \left(\frac{\Delta k_y}{\sigma_{k_y}}\right)^2 + \left(\frac{\Delta C}{\sigma_C}\right)^2 . \tag{3.1}$$

The σs in the above equation are the sum in quadrature of the corresponding errors for the PC muon and the candidate VT track:

$$\sigma_i^2 = \left(\sigma_i^{\text{PC}}\right)^2 + \left(\sigma_i^{\text{VT}}\right)^2 , \qquad i = k_x, k_y, C. \tag{3.2}$$

Our reconstruction settings consider a match only for candidates with $\chi^2_{\text{match}} < 5.0$; for a given PC muon up to 10 VT candidates can be stored for further processing. Selected candidates are refitted loosely constrained by the momentum (curvature) of the PC muon. Finally, if both muons of the PC dimuon have at least one match candidate in the vertex telescope, a joint fit of the two muons is performed, using

a common vertex, with an algorithm implementing a "Kalman filter". Each pair of VT tracks, being matched with two different PC muons, is referred to as "VT dimuon", as well as "matched dimuon".

3.2.3 Vertex Finding

The vertex finding algorithm is based on a robust fitting method, which assigns a weight to each of the contributing tracks. Only tracks which have a good fit quality ($\chi^2_{\rm fit} < 1.5$) and a momentum above 2 GeV/c are selected to contribute to the vertex finding.

The vertex reconstruction is an iterative process which stops when the new vertex z-position and the old one differ by less than 100 μm. Only tracks whose weighted distance from the vertex is reasonably small are attached.

As long as the number of the remaining qualified VT tracks is larger than 1, the search for a new vertex is started. In the final step of the vertex finding − after all vertices have been identified − also the tracks which did not qualify for the vertex finding are attached, if possible, to one of the found vertices. The number of reconstructed vertices per event can be larger than 1, due to:

- pile-up interactions occurring during the read-out time of the vertex telescope, given by the 2×25 ns read-out time of ATLAS pixel planes (by requiring that each track must leave a hit in at least one of the ATLAS pixel planes), as explained in Chapter 2 (the pile-up contribution has been studied in detail in [74])

- re-interactions of high-energetic secondary particles in downstream targets

- "fake" reconstructed vertices (possibly deriving from "fake" reconstructed VT tracks, but also due to having relaxed cuts on the vertexing algorithm in order not to loose any real vertex)

Regarding the last point, we note that the vertexing algorithm was tuned to detect all possible *distinct* vertices, even if they are relatively close. It happens, however, that in a few cases one real vertex is artificially splitted into two; moreover, fake vertices can occur as a consequence of fakely reconstructed VT tracks, in particular if the multiplicity of hits deposited in the VT tracker is rather high.

3.3 Dimuon Selection

In this section we describe the selection applied to the data. After providing some general characterization on the events, the cuts applied to the dimuon sample are described, which make possible to define a final sample of dimuons to be analyzed.

3.3.1 Event Characterization

Ideally, the events we would like to study should have one matched dimuon (i.e. one pair of PC muons matched to a pair of VT tracks), coming from a well-defined VT vertex reconstructed within the volume of one of the sub-targets used in the experiment. Indeed, if we look at the sample of reconstructed events having a matched dimuon, we observe that the average number of muon pairs tracked in the PC telescope within the time resolution of the R1-R4 trigger is ~ 1. On the contrary, the VT telescope integrates, within the read-out interval of the pixel planes, an average number of interactions larger than one. The read-out interval of the vertex telescope is 2×25 ns when the ATLAS planes are considered mandatory planes in the reconstruction; otherwise it amounts to 2×100 ns, which is the read-out time of the ALICE planes.

Reconstructed VT Vertices

In Figure 3.5 the distribution of the number of VT vertices per event is showed. As already mentioned, three main mechanisms may be invoked to explain the observed number of reconstructed vertices per event larger than 1:

- pile-up interactions occurring during the read-out time of the vertex telescope, given by the 2×25 ns read-out time of the ATLAS pixel planes
- re-interactions of high-energetic secondary particles in downstream targets
- "fake" reconstructed vertices (possibly deriving from "fake" reconstructed VT tracks, but also due to having relaxed cuts on the vertexing algorithm in order not to loose any real vertex)

An estimation of the expected average number of pile-up interactions, occurring during the read-out gate of the vertex telescope, can be found in [74]. The calculations show that the pile-up contribution can explain almost by itself the observed number of reconstructed vertices.

The reconstructed VT vertices are sorted according to the order by which the vertexing algorithm find them; in this way, the "best vertex" can be identified as the first vertex found by the vertexing algorithm, which then profits from the full sample of reconstructed VT tracks. As a result, the "best vertex" typically is the one with the largest number of attached tracks. In addition, two "quality" parameters are defined characterizing the VT vertices. These parameters are related to the overall compatibility of the VT tracks with the VT vertex to which they are attached.

It is worth noting that in the present analysis we cannot apply any additional cut to the quality of the reconstructed VT vertices, besides the ones already given by the reconstruction algorithm. The reason is simply that the quality of a VT vertex is not correlated with the vertex to be the origin of a matched dimuon; we must always look at all the reconstructed VT vertices, not only at the "best" one, and see which one of them is more likely to have produced the matched dimuon.

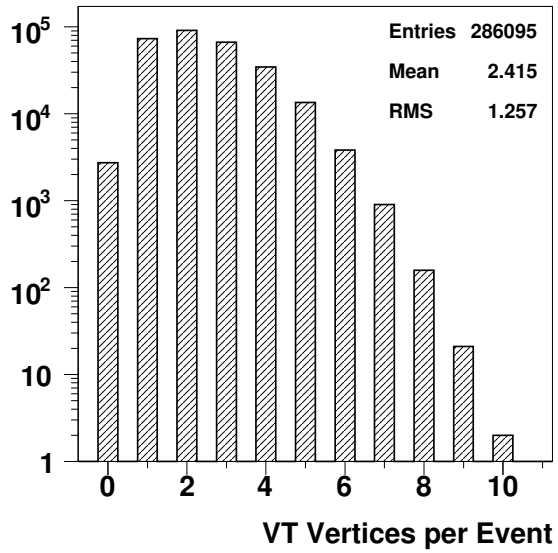

Figure 3.5: *Number of VT vertices reconstructed per event, for the full sample of events having at least one reconstructed VT dimuon.*

Reconstructed VT Muons and Dimuons

Due to the number of tracks integrated by the vertex telescope within its read-out time, each PC muon usually have more than one VT track as a matching candidate. Due to the uncertainty in the extrapolation from the muon spectrometer back to the target region, this results in an average number of VT muons per event larger than two, see left panel of Figure 3.6. In turn, it results in an average number of VT dimuons per event larger than one, see right panel of Figure 3.6.

Having an average number of VT dimuons per event larger than one, we have to define a criterion to select the VT dimuon we want to retain for the analysis. It is worth to note that this case is not equivalent to the one concerning the VT vertices multiplicity: in fact, we expect to have several interactions being integrated within the read-out time of the vertex telescope, each one producing a "genuine" interaction vertex; on the other hand, we know that each PC muon corresponds to one and only one VT track, so we only consider its VT track candidate having the best matching χ^2. This allows to consider only one VT dimuon for the analysis, corresponding to a given PC dimuon.

It should be noted that the possibility to match the PC tracks with the corresponding VT tracks dramatically improves the mass resolution of the NA60 apparatus, with respect to the former NA50 and NA38 experiments, which only could exploit the tracking performances of the muon spectrometer, no tracking being available before the absorber. The improvement is most significant for dimuons in the low mass region, their low energetic muons being maximally exposed to the effects of multiple scattering inside the absorber. In Figure 3.7 the mass spectrum up to 4 GeV/c^2 is plotted, considering the events having a VT dimuon: the figure shows how the mass spectrum appears when considering the information of the PC dimuons only (black profile, on the top), and how the resolution improves when the full information of

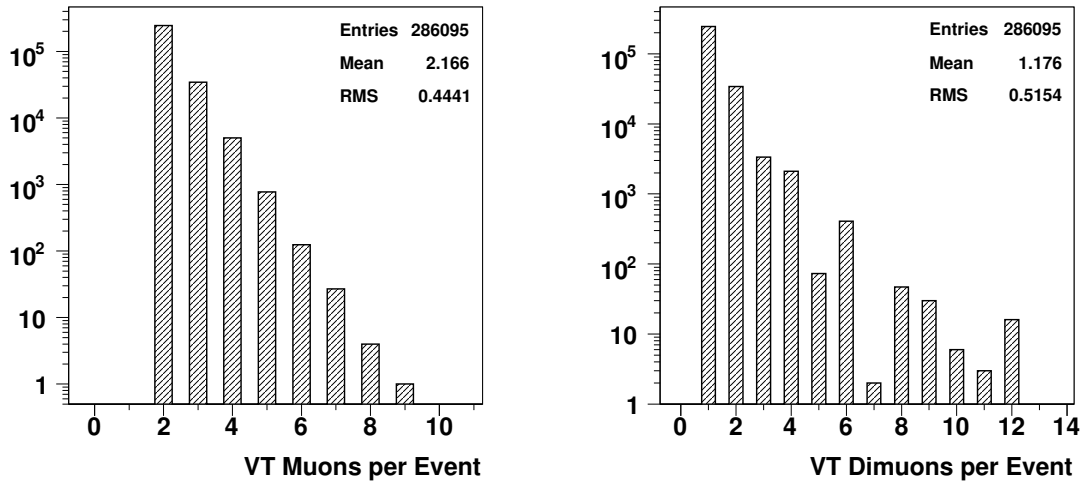

Figure 3.6: *Left panel: number of VT muons identified per event (tracks reconstructed in the vertex telescope and matched to one of the muons tracked in the muon spectrometer). Right panel: number of VT dimuons identified per event, built up combining the available VT muons.*

the combined tracking after and before the absorber − condensed in the VT dimuons kinematics − is taken into account (blue profile, on the bottom). As one can notice, J/ψ region does not show crucial improvements when applying the matching information, while the situation is much different for the low mass region: here the mass resolution clearly improves, allowing the peaks of the 2-body decays of the ϕ and ω resonances to be fully disentangled, while the characteristic shoulder on the left of the ω peak, due to the ρ contribution, becomes now pretty evident.

3.3.2 Matching χ^2 for Single Muons

The possibility to match each PC muon with a VT track automatically leads to the problem of defining the reliability of the match. As already previously explained, a variable is then introduced, named χ^2_{match}, defining quantitatively the compatibility between the matched tracks, according to Equation (3.1): the higher the χ^2_{match}, the worse the quality of the match.

In Figure 3.8 the distribution of the matching χ^2 for the single muons composing the matched dimuons is shown. The panel on the left shows the χ^2 distribution for the VT muons forming the OS and LS dimuon samples, integrated in mass; the panel on the right shows the same distributions for the OS dimuons in mass windows corresponding to the ω and ϕ mesons.

As one can see, the distribution of the matching χ^2 for the VT muons composing the LS dimuons is definitely worse than the one corresponding to the VT muons com-

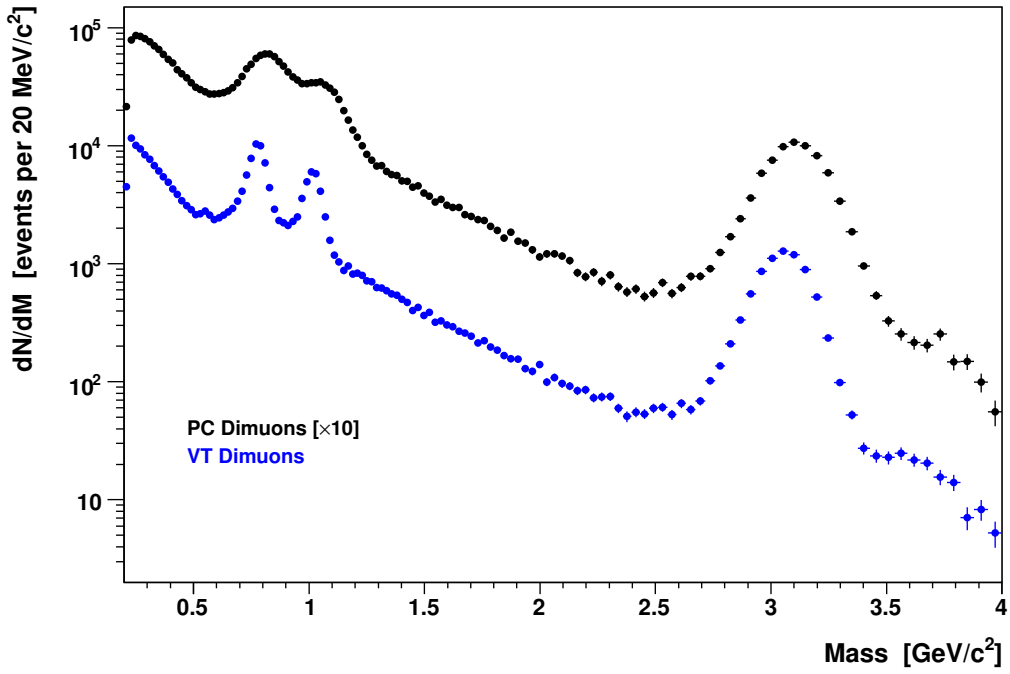

Figure 3.7: *Raw mass spectrum for the OS dimuons. The resolution significantly improves when the full information of the combined tracking after and before the absorber is considered.*

ing from OS dimuons: the LS muon pairs essentially consist of muons deriving from the uncorrelated muon decays of π and K mesons, in which the *mesons* are tracked within the geometrical acceptance of the vertex telescope and the final *muons* are then produced within the geometrical acceptance of the muon spectrometer. Since the kinematics of the muons created in such a decay differs from the kinematics of the mother particles (especially in the case of the K mesons, whose mass significantly differs from that of the muons) the matching stage results in a bad matching χ^2.

For OS dimuons, the contribution coming from correlated muon pairs largely dominates over the uncorrelated muon pairs. In this case the matching algorithm matches the two tracks (reconstructed in the vertex telescope and in the muon spectrometer, respectively) left by the *same* particle, hence, having similar kinematics: indeed, the resulting distribution is peaked at lower values than the LS one.

Selection Cuts

Simulations show the probability to have a correct match with $\chi^2 > 5.0$ is negligible, so that the cut $\chi^2_{\text{match}} < 5.0$ has been applied by default during the reconstruction step. However, in order to clean the OS dimuon sample, reducing the fraction of fake matches and improving the signal/background ratio, a stricter cut can be imposed.

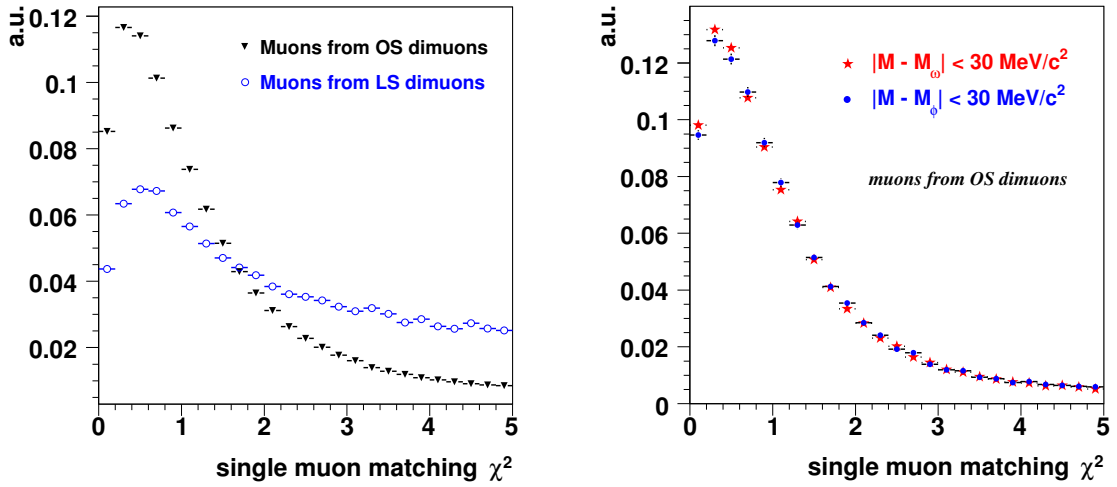

Figure 3.8: *Left panel:* χ^2_{match} *for the VT muons forming the OS and LS dimuons, with no mass selection. Right panel: same distributions considering OS dimuons only, in two mass windows centered on the* ω *and* ϕ *peaks.*

In order to roughly establish a cut for our sample, the distributions of the matching χ^2 for the VT muons composing the OS dimuons, in the ω and ϕ mass windows, were compared with the superposition of a χ^2 probability function (accounting for the "correct" behavior of the matching χ^2) and a constant offset (representing, in first order, the contribution from "fake" matches). The χ^2 probability function has the functional form for $x \geq 0$:

$$f(nx;n) = \frac{1}{2^{n/2}\,\Gamma(n/2)}\, x^{n/2-1}\, e^{-nx/2}\,, \tag{3.3}$$

where $\Gamma(z)$ is the Euler's Gamma function and the parameter $n = 1, 2, \ldots$ is the number of degrees of freedom of the distribution, which in the present case is set to $n = 3$, see Eqn. 3.1. The fits are shown in Figure 3.9. As one can see, for $\chi^2 \gtrsim 3$ the contribution coming from "properly" matched muons is comparable by the "fakely" matched muons. From inspection of the plots shown in Figure 3.9, the cut $\chi^2_{\text{match}} < 3.0$ was then chosen to be the χ^2_{match} cut for our event sample. We note here that a rigorous procedure to estimate the χ^2 distribution of the "fakely" matched muons should be based on an event-mixing analysis technique; such a study was performed within the analysis of the In-In data of NA60, from which a $\chi^2_{\text{match}} < 3.0$ cut was analogously derived.

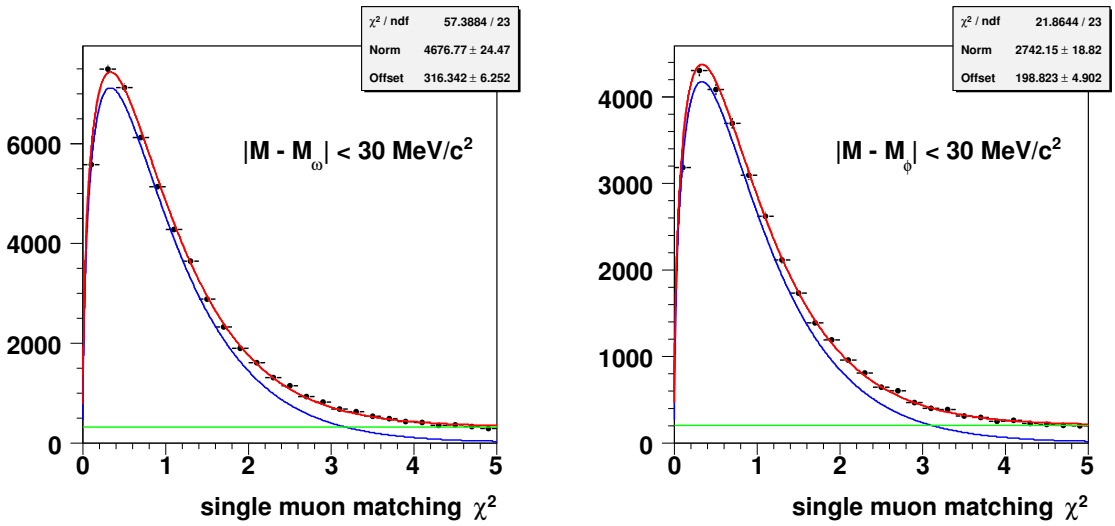

Figure 3.9: *Fit of the distributions of the matching χ^2 for the VT muons forming the OS, the ω (left panel) and ϕ (right panel) mass windows. Each distribution is compared with the superposition of a χ^2 probability function and a constant offset.*

3.3.3 Dimuon-Target Association

If we are not interested in identifying the target from which the matched dimuon originates, the only quality cut applied to the raw data is the one on the χ^2_{match} of the single VT muons. The χ^2_{match} cut is enough for defining the final sample in a target-integrated analysis, i.e. when the study can be performed independently on the production target. This is the case of the analysis of the electromagnetic transition form factors for the η and ω mesons, for instance, for which no target-dependence is expected, the form factors being *intensive* properties of the particles, not depending on the mechanisms or the conditions under which they are produced.

On the other hand, in order to address a study of the nuclear dependence of the yields and the kinematics for the particles produced in the collisions, the identification of the production target is mandatory for all the dimuons composing the final sample to be analyzed. It follows, hence, that a dimuon-target association criterion must be defined. Once the criterion has be defined, its performances can be studied with the help of MC simulations, both to understand the rate of correct associations, and characterize the bad matches.

Definition of the Dimuon-Target Association Criterion

A comparison between the performances of five different dimuon-target association criteria can be found in [74]. In general, any dimuon-target association criterion must rely either on finding the target directly considering the origin of the dimuon (defined as the point of closest approach of its two muon tracks), or on finding the

correct target considering the VT vertex from which we believe the dimuon comes from.

Considering the origin of the dimuon has the advantage to profit from the direct information given by the muon tracks. At the same time, the dimuon's origin is nothing but a two-tracks vertex, hence having a limited spatial resolution; in particular, the error associated to the z-position of the dimuon's origin becomes larger than the typical semi-distance between targets (~ 0.5 cm) for masses below 0.45 GeV/c^2, see top-left panel of Figure 3.10.

In order to overcome these difficulties, we can consider the VT vertices of the event, looking for the VT vertex from which we "trust" the dimuon is coming from (obviously, it is not possible for those $\sim 1\,\%$ events having a matched dimuon but no VT vertices); in this way, we take advantage from the better spatial resolution of the VT vertex (typically consisting of several tracks), but we are still using the information of the dimuon − even if a bit less directly. The association of a given dimuon with one of the VT vertices can be done using two different approaches:

- simply minimising the distance, weighted by the errors, between the VT vertex and the dimuon's origin, either in 3D or along the z-direction only
- considering the VT vertex to which the VT muons are attached to (if any)

Regarding the last point, the following situations are possible: (i) the muons are both attached to the same vertex; (ii) the muons are attached to different vertices; (iii) one of the muons is not attached to any vertex; (iv) none of the muons is attached to any vertex. In order to maximize the reliability of the dimuon-target association, we only consider those events in which both VT muons are attached to a VT vertex. It can also be shown that limiting the analysis to dimuons whose VT muons are attached to the *same* VT vertex, the chance of getting a correct dimuon-target association match does not improve with respect to also considering those dimuons whose VT muons come from *different* VT vertices, both falling within the same target.

In the top panels of Figure 3.10 the correlation between the dimuon mass and the uncertainty on its origin along the z direction is shown, both before and after having applied the "dimuon-target" association selection. The ratio between the two plots, also shown, demonstrates that the applied selection is more effective for dimuons whose origin is estimated with worse precision along the longitudinal coordinate (the one which discriminates between the production targets).

Performances of the Dimuon-Target Association Criterion

Not hard to believe, the performances of any dimuon-target association criterion depend on the dimuon mass, which influences both the number of events discarded from the analysis and the chance to have a correct association for the selected sample. As a consequence, each mass region could profit from an optimized association criterion. Unfortunately, in the present analysis we care about the whole low-mass

region, so that we are forced to find the best compromise optimizing the chance of a correct dimuon-target association for the total mass range considered: hence, profiting of the comparison study between various association criteria reported in [74], we finally establish the dimuon-target association criterion for the present analysis as the one defined by the following conditions:

- the two VT muons must be attached to the same VT vertex, or to two different VT vertices falling within the same target;

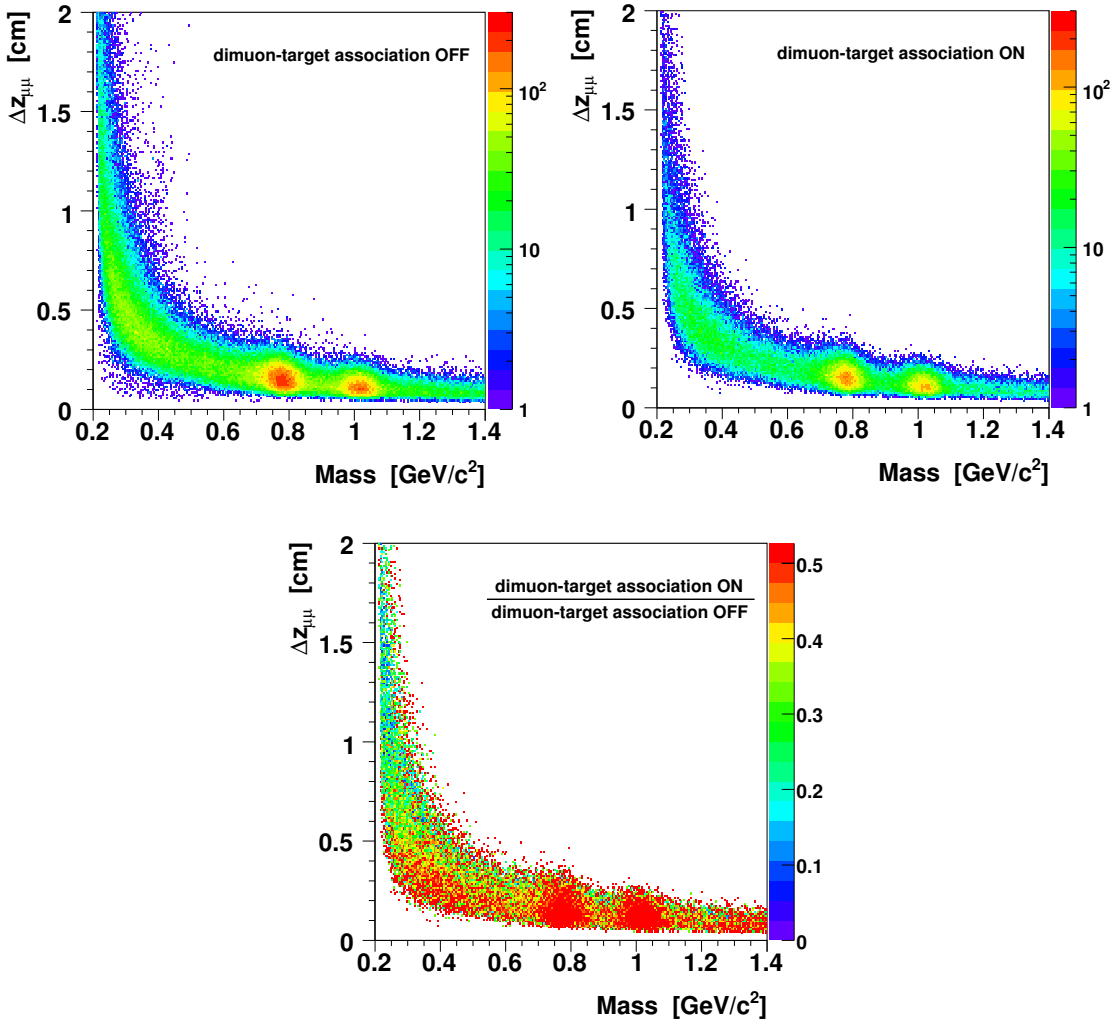

Figure 3.10: *Correlation between the dimuon mass and the uncertainty on its origin along the z direction, before (top left panel) and after (top right panel) applying the "dimuon-target" association selection described in the text. In the bottom panel, the ratio between the two distributions above is shown: as it can be seen, the dimuon-target selection is more effective for dimuons having a worse precision in the estimation of the origin along z.*

- the origin of the matched dimuon (defined as the point of closest approach of its two muon tracks) must fall within the same target as the two VT muons.

As already noted, the performances of the dimuon-target selection criterion defined above can be tested by means of MC simulations, for each of the sources contributing to the low mass dimuon spectrum (the sources are described in details in the next Chapter). For each MC process considered, we define the fraction ξ of lost dimuons (rejected by the conditions defining the criterion), and the correlation between the true and reconstructed production targets for each accepted dimuon − from this correlation deriving the "correctness" ϵ, defined as the fraction of accepted dimuons for which a correct dimuon-target association is given by the criterion.

Again, it does not come as a surprise that both ξ and ϵ heavily depends on the considered process, mainly because of their different kinematics, first of all the peculiar mass distributions. The values for ξ and ϵ are compiled in Table 3.2, with the $\eta \to \mu^+\mu^-\gamma$ and $\phi \to \mu^+\mu^-$ processes having the worst and the best (ξ, ϵ) values, respectively. The correlations turns out to be highly diagonal, with the off-diagonal elements mainly distributed along narrow side bands without evidence of any strong clusterisation. If no off-diagonal component was there in the correlation between true and reconstructed production target, we would have $\epsilon = 100\%$; the existence of such off-diagonal component, giving rise to values for ϵ below 100%, introduces a systematic uncertainty in associating each dimuon to its production target, which contributes to the systematic uncertainty in those analyses for which the identification of the production target is explicitly required for each dimuon.

	Process	**Statistics Loss ξ**	**Correctness ϵ**
Dalitz	$\eta \to \mu^+\mu^-\gamma$	72.2%	83.2%
	$\omega \to \mu^+\mu^-\pi^0$	65.6%	87.6%
	$\eta' \to \mu^+\mu^-\gamma$	57.6%	92.1%
2-body	$\eta \to \mu^+\mu^-$	53.0%	94.6%
	$\rho \to \mu^+\mu^-$	52.6%	94.4%
	$\omega \to \mu^+\mu^-$	48.4%	95.5%
	$\phi \to \mu^+\mu^-$	42.6%	97.6%

Table 3.2: *Statistics loss ξ resulting after applying the selection imposed by the dimuon-target association criterion, and probability ϵ of having a correct association for the dimuons retained by the selection. Values are given for the processes composing the "hadronic cocktail" (see next Chapter).*

4

The Low Mass Dimuon Spectrum: Expected Sources and MC Simulations

The dimuon mass spectrum observed in p-A collisions is a rich superposition of various sources, resulting in a continuously falling spectrum, on top of which several distinct resonance structures are observed.

At a beam energy of 400 GeV the continuous processes are the Drell-Yan dimuons, which dominates at large dimuon masses (i.e. above $\sim$ 3.5 GeV/c^2), and the semi-muonic simultaneous decays from two D mesons. This latter dimuon source, whose contribution is strongest at around 0.8 GeV/c^2, is often referred to as "open charm". The electromagnetic decays of the light pseudoscalar and vector mesons (η, η', ρ, ω and ϕ) are the dominating processes at the lower end of the dimuon mass spectrum, adding to the continuous spectrum via their Dalitz decays and/or giving rise to distinct peaks via their 2-body decays. We call their superposition the "hadronic decay cocktail". At higher masses the J/ψ and the ψ' can be observed, while the production cross section for the more massive bottomonium states is negligible at the SPS energies.

The hadronic decay cocktail was simulated with the NA60 Monte Carlo generator Genesis, the open charm process with Pythia. The input parameters for the kinematic distributions of the generated processes have been assumed from previous analyses [74, 78], and have been optimized by comparison with the real data, in the sense of an iterative procedure ensuring self-consistency to the analysis.

4.1 Espected Contributions to the Low Mass Dimuon Spectrum

As already mentioned, in p-A collisions at a beam energy of 400 GeV the main contributions to the low mass spectrum (which in the present analysis translates to $M < 1.4$ GeV/c^2) are the dimuon decays of the light neutral mesons η, ρ, ω, η' and ϕ, both via their Dalitz and 2-body decays. A small continuum component comes from the open charm process, smoothly extending over the whole low mass region and becoming the dominant contribution for $M > 1.2$ GeV/c^2.

4.1.1 Light Mesons Decays

Mesons consist of a quark and an antiquark. For spin $\frac{1}{2}$ quarks and antiquarks we can form spin triplet states ($\uparrow\uparrow$) with $J_S = 1$ and spin singlet states ($\uparrow\downarrow$) with $J_S = 0$. Fermions and antifermions have intrinsic opposite parity so that the $f\bar{f}$ pair carries parity $P = -1$. If they have orbital angular momentum, L, their parity is given by $P_{f\bar{f}} = (-1)^{L+1}$. Thus, the $J_S = 0$ states in the ground state $L = 0$ have the quantum numbers $J^P = 0^-$ and are called pseudoscalar mesons, while the $J_S = 1$ states with $L = 0$ have $J^P = 1^-$ and are called vector mesons.

As long as the first three quark flavours (u, d, s) are concerned, we expect pseudoscalar and vector meson families containing $3^2 = 9$ states. The pseudoscalar divide into an iso-vector triplet, namely the three pions, $\pi^+ = u\bar{d}$, $\pi^0 = 1/\sqrt{2} = (u\bar{u} - d\bar{d})$), $\pi^- = \bar{u}d$, and two iso-doublets, the $K^+ = u\bar{s}$, $K^0 = d\bar{s}$, $K^- = \bar{u}s$ and the $\bar{K}^0(\bar{d}s)$. The last two members of the pseudoscalar meson family are the η, η' mesons, whose actual states appear to be the following linear combinations:

$$\eta = \Big(\frac{\cos\theta_P}{\sqrt{6}} - \frac{\sin\theta_P}{\sqrt{3}}\Big)u\bar{u} + \Big(\frac{\cos\theta_P}{\sqrt{6}} - \frac{\sin\theta_P}{\sqrt{3}}\Big)d\bar{d} - \Big(\frac{\cos\theta_P}{\sqrt{6}/2} + \frac{\sin\theta_P}{\sqrt{3}}\Big)s\bar{s}\,, \qquad (4.1)$$

$$\eta' = \Big(\frac{\sin\theta_P}{\sqrt{6}} + \frac{\cos\theta_P}{\sqrt{3}}\Big)u\bar{u} + \Big(\frac{\sin\theta_P}{\sqrt{6}} + \frac{\cos\theta_P}{\sqrt{3}}\Big)d\bar{d} - \Big(\frac{\sin\theta_P}{\sqrt{6}/2} - \frac{\cos\theta_P}{\sqrt{3}}\Big)s\bar{s}\,. \qquad (4.2)$$

The pseudoscalar mixing angle, θ_P, is thought to be $\approx -10^\circ$, with a large uncertainty; this is compatible with the mixing $\eta = 1/\sqrt{6}(u\bar{u} + d\bar{d} - 2s\bar{s})$ and $\eta' = 1/\sqrt{3}(u\bar{u} + d\bar{d} + s\bar{s})$, which would decompose the pseudoscalar nonet into an $SU(3)$ octet and an $SU(3)$ singlet.

The (quark) structure of the vector meson states is similar to the one of the pseudoscalars. The $J_S = 1$ analog of the pions are the ρ's with the same quark contents, while the vector K^*'s mesons correspond to the pseudoscalar K's. The vector counterpart of the η and η' are the ϕ and the ω, respectively; the observed ϕ and ω states are again mixtures of the pure states $u\bar{u}$, $d\bar{d}$ and $u\bar{u}$, but the measured angle $\theta_V \approx 35^\circ$

is much larger than θ_P and is compatible with the ideal mixing angle for which the ϕ becomes a pure $s\bar{s}$ state:

$$\omega = \frac{1}{\sqrt{2}}(u\bar{u} + d\bar{d}) \,, \qquad \phi = s\bar{s} \,. \tag{4.3}$$

By contrast to the pseudoscalar case, hence, neither the ω nor the ϕ is an $SU(3)$ singlet.

The properties of the pseudoscalar and vector mesons which contribute significantly to the dimuon mass spectrum, either through a decay into two muons or via a Dalitz decay, are summarised in Table 4.1.

Particle	**Mass** $[\mathrm{MeV}/c^2]$	$\boldsymbol{\Gamma}$ $[\mathrm{MeV}/c^2]$	$\boldsymbol{J^{PC}}$	**Quark Content**
η	547.853 ± 0.024	$(1.30 \pm 0.07) \cdot 10^{-3}$	0^{-+}	$\frac{1}{\sqrt{6}}(u\bar{u} + d\bar{d} - 2s\bar{s})$
ρ	775.49 ± 0.34	146.2 ± 0.7	1^{--}	$\frac{1}{\sqrt{2}}(u\bar{u} - d\bar{d})$
ω	782.65 ± 0.12	8.49 ± 0.08	1^{--}	$\frac{1}{\sqrt{2}}(u\bar{u} + d\bar{d})$
η'	957.78 ± 0.06	0.194 ± 0.009	0^{-+}	$\frac{1}{\sqrt{3}}(u\bar{u} + d\bar{d} + s\bar{s})$
ϕ	1019.455 ± 0.020	4.26 ± 0.04	1^{--}	$s\bar{s}$

Table 4.1: *Properties of the light pseudoscalar and vector mesons contributing to the dimuon mass spectrum, values taken from [55].*

The Pseudoscalar Mesons, η and η'

Figure 4.1 shows the Dalitz and 2-body decays of the η and the η' pseudoscalar mesons. The (single) Dalitz decay (diagram on the left) is a 2γ decay, in which one of the photons is virtual and converts into a lepton pair, $PS \to \gamma^*\gamma \to \mu^+\mu^-\gamma$. There is also a double Dalitz decay (central diagram) in which both γ's are virtual photons and convert into a lepton pair, but with a much smaller branching ratio. The decay of the η into two muons (diagram on the right) is a 4^{th} order electromagnetic process, where the μ^+ coming from one γ^* and the μ^- coming from the other γ^* are contracted.

The branching ratio into two muons has a lower limit [47] given by the radiative decay channel,

$$BR(\mathrm{PS} \to \ell^+\ell^-) \geq BR(\mathrm{PS} \to \gamma\gamma) \cdot 2\alpha^2 \Big(\frac{m_\ell}{m_{\mathrm{PS}}}\Big)^2 \sqrt{1 - 4\Big(\frac{m_\ell}{m_{\mathrm{PS}}}\Big)^2} \quad . \tag{4.4}$$

From this equation we can see that the electronic branching ratio is suppressed with respect to the muonic one, by the ratio $(m_e/m_\mu)^2$. For the η the following lower limits were deduced [47]:

$$\begin{aligned} BR(\eta \to \mu^+\mu^-) &\geq 4.0 \cdot 10^{-6} \quad , \\ BR(\eta \to e^+e^-) &\geq 1.7 \cdot 10^{-9} \quad . \end{aligned}$$

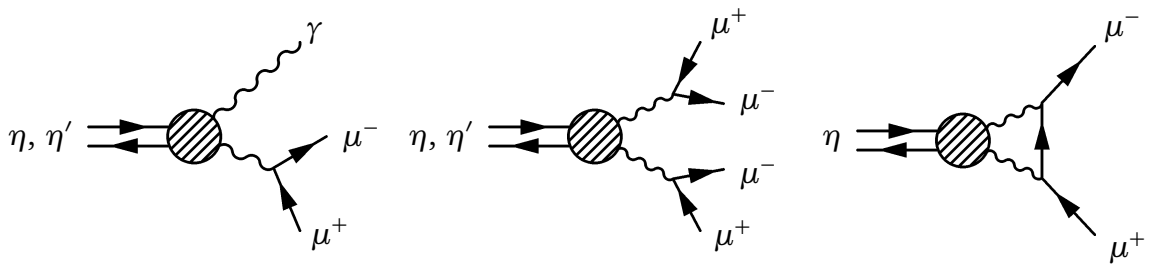

Figure 4.1: *Single Dalitz, Double Dalitz and two body decays of the pseudoscalar mesons η and η'.*

Indeed, only the muonic branching ratio is measured at present. Its value, taken from Ref. [55], is $BR(\eta \to \mu^+\mu^-) = (5.8 \pm 0.8) \cdot 10^{-6}$. For the η' 2-body leptonic decay channels there are also such theoretical lower limits. Experimentally, however, not even an upper limit is published in the PDG tables so that we can safely neglect its contribution to the dimuon mass spectrum (as one can see from Equation 4.4, the branching ratio for the 2-body decay of the η' is suppressed with respect to the one of the η, because of the factors m_ℓ/m_{PS}).

The (single) Dalitz decay channel of the η' is comparable to the one of the η, so that we must consider this process. Unfortunately, the production cross-section of the η' was never measured. Following the analysis reported in [22], we have assumed in the present work $\eta'/\omega = 0.12$; in any case, as it will be shown in the next Chapters, the large uncertainty on the η' normalization will be taken into account as a major component for the systematic uncertainty on the results.

The Light Vector Mesons: ρ, ω and ϕ

The vector mesons ρ, ω and ϕ mainly contribute to the dimuon mass spectrum via their $\mu^+\mu^-$ decay mode. The electromagnetic decay of the vector mesons ρ, ω and ϕ into two muons proceeds via a virtual photon, $V \to \gamma^* \to \mu^+\mu^-$ (they have the same J^{PC} quantum numbers as the photon). The ω possesses, furthermore, a non-negligible Dalitz decay mode, in which the lepton pair is accompanied by a π^0, $\omega \to \gamma^*\pi^0 \to \mu^+\mu^-\pi^0$, see Figure 4.2.

Branching Ratios

Table 4.2 summarizes the processes contributing to the hadronic cocktail and gives their branching ratios, taken from the Particle Data Group tables [55].

Note that we used the electronic branching ratio for the ω 2-body decay, since it is known with much better accuracy than the muonic value. We have done this assuming lepton universality, which states that the electro-weak interaction couples to all leptons with the same strength. Indeed, the electronic and muonic branching

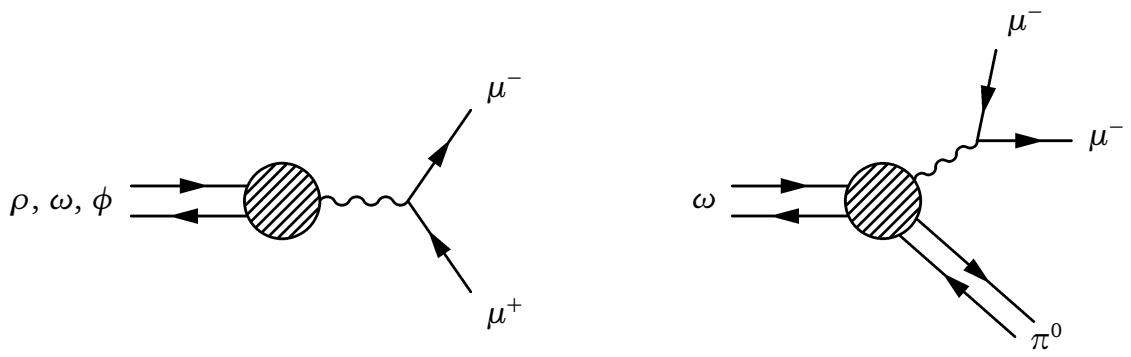

Figure 4.2: *Dimuon decay of the vector mesons ρ, ω and ϕ (left) and the ω Dalitz decay (right).*

ratios, listed in the PDG tables, agree within their error bars, $BR(\omega \to e^+e^-) = (7.28 \pm 0.14) \cdot 10^{-5}$, $BR(\omega \to \mu^+\mu^-) = (9.0 \pm 3.1) \cdot 10^{-5}$.

The branching ratio for the ω Dalitz decay has been recently updated with respect to the 2008 value ($BR_{2008}(\omega \to \mu^+\mu^-\pi^0) = (9.6 \pm 2.3) \cdot 10^{-5}$) on the basis of a new measure of the $BR(\omega \to \mu^+\mu^-)/BR(\omega \to \mu^+\mu^-\pi^0)$ ratio, obtained as a by-product of the analysis of the peripheral NA60 In-In data, as reported in [22]. The present analysis on the p-A sample has also sensitivity to the $BR(\omega \to \mu^+\mu^-)/BR(\omega \to \mu^+\mu^-\pi^0)$ ratio, so that a new estimation for it can be given here. Hence, in order to directly compare our results with those obtained in the analysis of the peripheral In-In data, we will often explicitly refer to the 2008 value of the ω Dalitz branching ratio, $BR_{2008}(\omega \to \mu^+\mu^-\pi^0) = (9.6 \pm 2.3) \cdot 10^{-5}$.

	Particle	Decay Mode	Branching Ratio
Dalitz	η	$\mu^+\mu^-\gamma$	$(3.1 \pm 0.4) \cdot 10^{-4}$
	ω	$\mu^+\mu^-\pi^0$	$(1.3 \pm 0.4) \cdot 10^{-4}$
	η'	$\mu^+\mu^-\gamma$	$(1.09 \pm 0.27) \cdot 10^{-4}$
2-body	η	$\mu^+\mu^-$	$(5.8 \pm 0.8) \cdot 10^{-6}$
	ρ	$\mu^+\mu^-$	$(4.55 \pm 0.28) \cdot 10^{-5}$
	ω	$\mu^+\mu^-$	$(7.28 \pm 0.14) \cdot 10^{-5}$
	ϕ	$\mu^+\mu^-$	$(2.87 \pm 0.19) \cdot 10^{-4}$

Table 4.2: *Processes included in the hadronic decay cocktail and the branching ratios considered in our study.*

4.1.2 Open Charm

The continuum of the dimuon mass spectrum between the ϕ and the J/ψ mesons consists of the Drell–Yan process (DY) and of the simultaneous semi-muonic decay of pairs of D mesons; this latter source also gives a not-negligible contribution in the mass region from the threshold to the ϕ. For the present analysis, which does not consider the mass spectrum above the ϕ, the Drell–Yan process can be safely neglected.

D mesons are formed via the creation of a $c\bar{c}$ pair and the subsequent hadronization (fragmentation) of the charmed quarks, when each of them binds with a u, d or s quark (or antiquark), to form the D mesons. If both charmed hadrons then decay semi-muonically, they may contribute to the dimuon mass spectrum, if the two muons are accepted and reconstructed. Since the energy of the muons depends on the decay kinematics which is not fixed, the formed muon pair will have a continuum spectrum of invariant masses.

At leading order, charm production at SPS energies proceeds through gluon fusion in $\sim 80\,\%$ of the cases and through quark-antiquark annihilation in the other $\sim 20\,\%$. The corresponding first order diagrams can be seen in Fig. 4.3.

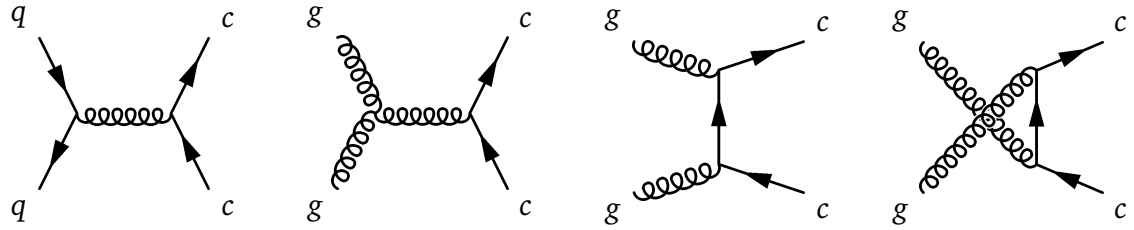

Figure 4.3: *Production mechanisms for $c\bar{c}$ production in first order perturbation theory.*

In [79] an extensive review of measured D meson cross-sections was performed and compared to lowest order calculations performed with Pythia, having varied Pythia's input parameters, like the mass of the c quark, which is not directly accessible to experimental measurements, or the set of Parton Distribution Functions (PDF). From the measurements of D meson production cross-section, the total $c\bar{c}$ cross-section was plotted as a function of the collision energy; the Pythia calculations were then scaled up in order to describe the existing data. From this procedure, the full phase space p-p cross-section was derived to be around 20 μb at $E_{\mathrm{lab}} = 400$ GeV.

In order to generate "open charm", we have used Pythia with its standard settings, i.e. the mass of charm quark was set to $m_c = 1.5$ GeV and the primordial momentum of the interacting partons was generated according to a Gaussian distribution of variance $k_{\mathrm{T}}^2 = 1.0$ (GeV/c)^2. We have generated all final state charmed hadrons with a semi-muonic decay, D^+, D^0, D_s^+, Λ_c^+, Ξ_c^0, Ξ_c^+, Ω_c^0 and their corresponding anti-particles with the relative particle abundances given by Pythia.

In order to accelerate the generation process, we have set the corresponding

branching ratios into muons to 100 %. In the final event analysis each event contributed then with a weight which is the product of the branching ratios of the two decaying charmed hadrons, thereby correctly accounting for the individual branching ratios, which were taken from the Particle Data Group tables [55].

4.2 MC simulations of the Hadronic Cocktail

As already mentioned, the processes included in the hadronic decay cocktail were simulated with the NA60 Monte Carlo generator Genesis, while for the simulation of the open charm contribution the Pythia generator has been used. Details concerning the generation of the open charm contribution have already be given above; in this Section, we focus on the details concerning the simulation of the hadronic cocktail, by far the dominant contribution to the low mass dimuon spectrum.

4.2.1 The Overlay Monte Carlo Simulation Technique

The MC simulations used in the present analysis were performed using a technique called "Overlay-MC"; it consists of superimposing a MC generated muon pair (disregarding of the generator which created it) onto real events, in order to realistically simulate the underlying hadronic event together with the detector specific behaviors. This technique has been adopted both for the simulation of the open charm and the hadronic cocktail. The Overlay-MC simulations performed in this work proceed as follow:

- a *real* event is read, chosen among the reconstructed *data* collected by the experiment in a given run and burst, and the origin of the matched dimuon is determined; here two options have been considered: (i) only high-mass dimuons (chosen within the J/ψ mass window) are used for defining the origin, or (ii) only dimuons having their z-coordinate determined with an uncertainty smaller than 3 mm. The first option is the "reference" one, providing the cleanest sample of production vertices, while the second one, applying weaker conditions on the vertex candidates, has been considered for systematic checks in the analysis;

- the vertex where to generate the dimuon is defined, having the same transverse coordinates of the vertex corresponding to the origin of the real dimuon and a re-defined z-coordinate chosen randomly within the width of the vertex' nearest target: the so-defined vertex is then imposed as the origin of the particle to be generated when simulating the process under study; note that when simulating the "open charm" contribution, the origin of the muon tracks are given "randomly" by Pythia, based on the decay lengths of the charmed hadrons and their kinematics;

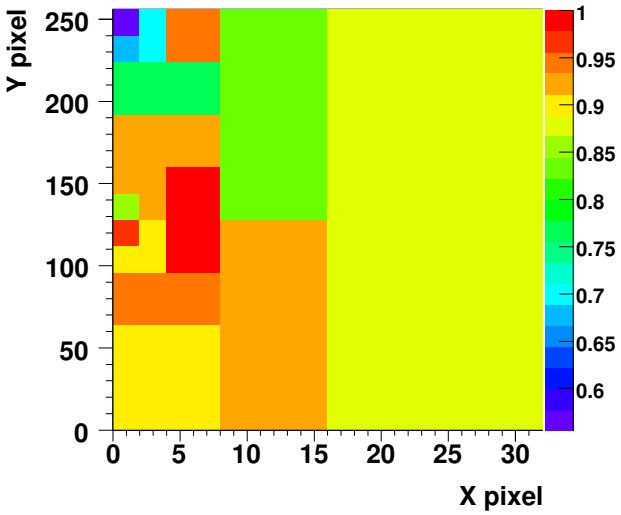

Figure 4.4: *Efficiency map for the first pixel chip of the first tracking plane, run 11609.*

- the muon pair produced in the simulation is tracked through the NA60 apparatus, using GEANT. The hits left by the MC particles in the various detectors are then put together with the hits stored in the real event from which the MC vertex was deduced: in this way we are simulating a full event without having to generate the full underlying hadronic event;

- starting from the ensemble of the MC and real hits, the events in which a muon pair gave rise to a trigger were reconstructed using the same reconstruction settings described in Chapter 3. To make the MC simulation as realistic as possible, the MC tracks leave a signal in a given VT plane with a probability proportional to the plane efficiency estimated − run by run − from the analysis of the real data. In Figure 4.4 the efficiency map for the first pixel chip of the first tracking plane is shown, corresponding to run 11609.

It is worth noting that − when putting together the MC and the real hits − we are not considering the real hits in the muon spectrometer, in order to not alter the charged multiplicity observed in the apparatus beyond the hadron absorber. We also exclude the real hits of the VT muons, in order to not alter the average number of tracks attached to the reconstructed VT vertices.

For the tracks other than the ones generated with Genesis, the Overlay-MC technique *automatically* reproduces the effects imposed by the detector, such as the finite acceptance window, the energy loss, and the smearing of the kinematics through multiple scattering or due to the finite resolution of the apparatus.

4.2.2 Transverse Momentum and Rapidity Distributions

The p_T distributions for the light mesons were originally generated according to the distribution

$$\frac{1}{p_T}\frac{dN}{dp_T} = \frac{1}{m_T}\frac{dN}{dm_T} = m_T K_1\left(\frac{m_T}{T}\right) , \tag{4.5}$$

where $K_1(x)$ is the modified Bessel function of the second kind of order 1. This functional form is very close to a pure exponential shape, justified under the hypothesis of a thermal-like p_T distribution:

$$\frac{1}{p_T}\frac{dN}{dp_T} = \frac{1}{m_T}\frac{dN}{dm_T} = \exp\left(-\frac{m_T}{T}\right) . \tag{4.6}$$

Here, it should be noted that the T parameters involved in the two parametrizations cannot be directly compared. MC simulations based on this thermal-like assumption for the p_T distributions were used to perform a first round of the analysis, including the estimation of the p_T distributions for the neutral mesons, corrected for the acceptance and efficiency. As this analysis showed that the p_T line shapes contained a hard tail not described by the exponential functional form, new simulations were then performed, adopting a power-law parametrization which proved to be able to describe the observed p_T distributions:

$$\frac{dN}{dp_T^2} \propto \left(1 + \frac{p_T^2}{p_0^2}\right)^{-\beta} , \tag{4.7}$$

with the following p_0^2, β parameters extracted by the fit on the acceptance-corrected p_T distributions (see next Chapters):

Particle	p_0^2 **[GeV^2/c^2]**	β
$\eta(548)$	1.74	6.35
$\rho(775)$	$\rightarrow$ as for the ω	
$\omega(783)$	0.84	3.40
$\eta'(958)$	$\rightarrow$ as for the ϕ	
$\phi(1019)$	1.50	4.10

Table 4.3: *Input parameters for the generation of the p_T distribution, according to the power-law (4.7).*

The rapidity distributions in the Center of Mass frame (CM frame) were generated according to the expression

$$\frac{dN}{dy} \propto \frac{1}{\cosh^2(ay)} , \tag{4.8}$$

similar to a Gaussian of $\sigma = 0.75/a$. This simple parameterization has been used by several experiments, since it describes reasonably well existing measurements.

The width of the pion rapidity distribution was estimated using Landau's expression $\sqrt{\log \gamma_{\text{proj}}}$. The width of the rapidity distribution for heavier mesons is decreased proportionally to the maximum rapidity with which such a meson can be produced in the center-of-mass frame for a given $\sqrt{s}$:

$$\sigma_{\text{part}} = \sigma_{\pi} \cdot y^{\text{cm}}_{\text{max}}(m_{\text{part}}) / y^{\text{cm}}_{\text{max}}(m_{\pi}) \,, \tag{4.9}$$

with $y^{\text{cm}}_{\text{max}} = \log(\sqrt{s}/m_{\text{part}})$. Table 4.4 summarizes the width parameters of the rapidity distributions for the particles relevant for the Genesis event generator, including the π^0 and the J/ψ, at $E_{\text{lab}} = 400$ GeV.

Particle	**Mass** $[\text{GeV}/c^2]$	σ_y	a_y
π^0	0.135	1.84	0.41
η	0.548	1.35	0.56
ρ	0.776	1.23	0.61
ω	0.783	1.23	0.61
η'	0.958	1.16	0.65
ϕ	1.019	1.14	0.66
J/ψ	3.097	0.75	1.00

Table 4.4: *Parameters of the rapidity distributions of particles with different masses, for collisions with a beam energy of* $E_{\text{lab}} = 400$ *GeV.*

4.2.3 Mass Line Shapes

For the mass line shapes of the narrow resonances η, ω and ϕ, we have used a modified relativistic Breit-Wigner parametrization, first proposed by G.J. Gounaris and J.J. Sakurai [36], with widths and masses taken from the PDG tables [55]:

$$\frac{\mathrm{d}N}{\mathrm{d}M} \propto \frac{\sqrt{1 - \frac{4m_\mu^2}{M^2}} \left(1 + 2\frac{m_\mu^2}{M^2}\right)}{\left(m_0^2 - M^2\right)^2 + m_0^2 \Gamma^2(M)} \,, \tag{4.10}$$

where the mass-dependent width $\Gamma(M)$ is given by the following expression:

$$\Gamma(M) = \Gamma_0 \frac{m_0}{M} \left(\frac{M^2/4 - m_\mu^2}{m_0^2/4 - m_\mu^2} \right)^{3/2} = \Gamma_0 \frac{m_0}{M} \left(\frac{q}{q_0} \right)^3 \tag{4.11}$$

with the Γ_0 taken from the PDG tables [55].

In principle, although, one should note that in an inclusive measurement, where one picks out one out of N particles, that particle has an exponential spectrum over a large range in energy, with an effective "temperature" T. The T parameter should not be literally interpreted as a thermodynamic variable, unless the amount of rescattering experienced by the produced particles is large enough so that the whole ensemble could equilibrate: this latter is the case of heavy ion collisions, while in proton-nucleus collision − at the SPS energies − such collective mechanisms are not expected to be effective. In any case, leaving apart the interpretation of the T parameter, it is true that we should weight the probability to produce a particle with a mass M (expressed by the $\mathrm{d}N/\mathrm{d}M$ distribution) with the factor $(2\pi MT)^{3/2}\, e^{-\frac{M}{T}}$, which from now on we will refer to as "Boltzman-like factor", although forcing in this way its interpretation in a thermodynamic sense − which in p-A collisions at SPS energies is not justified. The resulting line shape will then be:

$$\frac{\mathrm{d}N}{\mathrm{d}M} \propto \frac{\sqrt{1-\frac{4m_\mu^2}{M^2}}\left(1+2\frac{m_\mu^2}{M^2}\right)}{\left(m_0^2-M^2\right)^2+m_0^2\Gamma^2(M)}\,(2\pi MT)^{3/2}\,e^{-\frac{M}{T}}\ . \tag{4.12}$$

Actually, one can show that the effect of this Boltzman-like factor is only relevant for broad resonances: this factor varies smoothly with mass, at least compared with the Gounaris-Sakurai parametrization for the narrow resonances, so that for the η, ω and ϕ particles it can be safely neglected, see left panel of Figure 4.5.

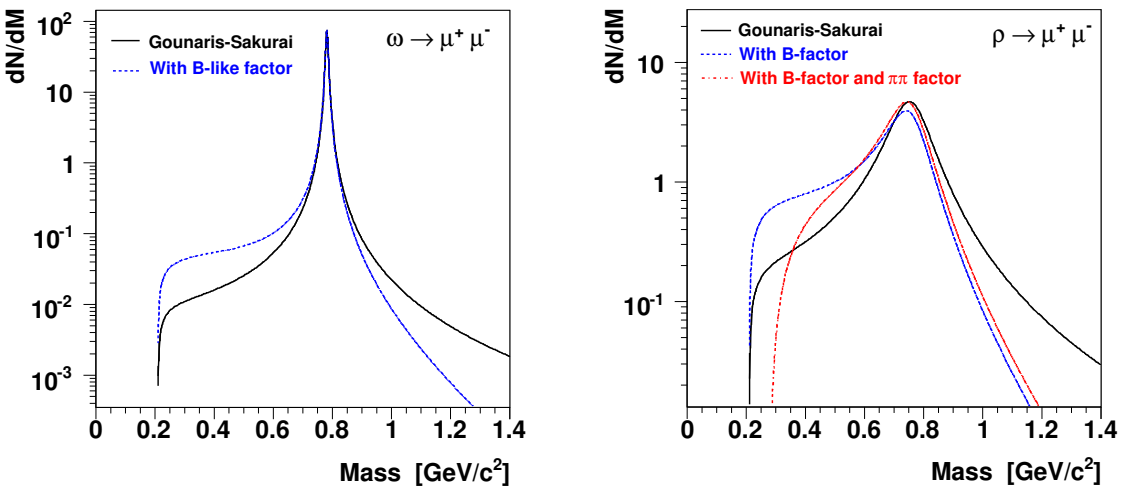

Figure 4.5: *Left panel: line shape for the 2-body decay $\omega \to \mu^+\mu^-$, with and without the Boltzman-like factor. Right panel: line shape for the 2-body decay $\rho \to \mu^+\mu^-$, with and without the Boltzman-like factor and the factor accounting for the $\pi\pi$ channel.*

The ρ meson predominantly decays in the two-pion channel, $BR(\rho \rightarrow \pi^+\pi^-) \approx 100\,\%$. Particles decaying via the strong interaction are characterized by lifetimes of the order of $\tau \sim 10^{-22} - 10^{-24}$ s, resulting in decay widths, $\Gamma \equiv 1/\tau$, of around 100 MeV. The ρ, hence, is a "broad" resonance with a decay width of ~ 150 MeV. Due to its broadness, the shape of the ρ is highly influenced by the Boltzman-like factor, as can be appreciated in the right panel of Figure 4.5. In addition to the Boltzman-like factor, the literature for the ρ line shape also includes an additional phase space factor deriving from taking into account the strong coupling of the ρ with $\pi^+\pi^-$ channel. This factor, accounting for the additional term $\left(1 - \frac{4m_\pi^2}{M^2}\right)^{3/2}$, is justified in heavy ion collisions, where the dissociation and recombination mechanisms via the two-pion channel strongly influence ρ production in a pion-rich environment. These same mechanisms are probably less effective in the environment of a proton-nucleus collision at the SPS energies, so that the "$\pi\pi$ factor" (which, furthermore, imposes a kinematic threshold at $2m_\pi > 2m_\mu$) can be safely neglected when considering the line shape for the ρ.

Dalitz Decays

The lepton pair mass distribution in the Dalitz decays of interest for the present analysis was derived by N. Kroll and W. Wada [46]. As explained in Chapter 1, the measured dimuon mass spectrum for the Dalitz conversion decays deviates from the theoretical prediction by the so-called electromagnetic transition form factors, which can be calculated in the frame of the Vector Meson Dominance model. The form factors for the simulations performed in this work were initially set according to the recent NA60 peripheral In-In measurements [22], and then fixed to the preliminary values obtained by the present analysis itself, i.e. $\Lambda_\eta^{-2} = 1.94\ (\mathrm{GeV}/c^2)^{-2}$ and $\Lambda_\omega^{-2} = 2.25\ (\mathrm{GeV}/c^2)^{-2}$. Concerning the form factor of the η', neither the present analysis nor the previous In-In one are able to make the point on its measurement, so that we have to rely on the previous measurements, reported in [47], resulting in a Breit-Wigner parametrization:

$$|F_{\eta'}|^2 = \frac{m_0^4}{\left(m_0^2 - M^2\right)^2 + m_0^2\Gamma_0^2}\,, \tag{4.13}$$

where the parameters m_0 and Γ_0 are set by the fit to $m_0 = 0.764$ GeV/c^2 and $\Gamma_0 = 0.102$ GeV/c^2, respectively. The η' form factor shows a characteristic enhancement corresponding to the ρ/ω peak, which can be easily interpreted in terms of the Vector Mesons Dominance model. The contribution of the Dalitz decay of the η', hence, mainly influences the level of the hadronic cocktail under the ρ/ω peak: for this reason, its normalization has to be carefully taken under control and the corresponding systematic uncertainty properly propagated to the final results.

4.2.4 Distribution of the Decay Angles

The kinematics of each resonance is determined by its 4-momentum, which in turn can be expressed in terms of the particle's mass, its rapidity, p_{T} and azimuthal angle. The kinematics of the muon pair needs further specifications, both in the case of 2-body and Dalitz (3-body) processes.

Regarding the 2-body decays, in principle, we need to know the 4-momentum of each muon, that is, 8 quantities; actually, we have 4 constraints coming from the conservation of 4-momentum (assuming that the parent particle's kinematic is fixed), and further two constraints since we know the mass of the particles produced in the decay. We are left with two degrees of freedom, given by the polar and azimuthal decay angles of the positive muon. Both the azimuthal angles of the parent particle and the positive muon have a flat distribution over 2π, and they are generated isotropically for all decay modes. The distribution of the polar decay angle in the helicity frame was chosen to be flat, too.

The Dalitz decays differ from the 2-body ones, since the virtual photon from which the muon pair originates does not share the kinematics of the parent particle. The kinematics of the virtual photon, hence, has to be calculated simulating the intermediate step corresponding to the $\gamma\gamma^*$ decay of the parent particle. Regarding the polar decay angle distribution for the positive muon, in the helicity frame of the dimuon, a $1 + \cos^2\theta$ distribution was chosen in case of the pseudo-scalar η and η', where the third partner is a (real) photon; on the contrary, for the ω Dalitz $-$ where the third partner is a π^0 $-$ we have adopted a uniform distribution for the polar angle. These parametrizations were already used in analysis of the low mass spectrum for the NA60 In-In data.

II

Analysis and Results

5

The Real Mass Spectrum: Signal and Background

In Chapter 4 we described the various physics processes originating the signal in the real mass spectrum. In this Chapter we show how these sources can be disentangled from each other by inspection of the raw mass spectrum, in order to evaluate the yield and the transverse momentum for each involved process.

However, before we describe how the signal is extracted from the raw mass spectrum, another important item must be addressed: the evaluation and subtraction of the background sources, i.e. the uncorrelated opposite-sign muon pair components which contribute to the real mass spectrum. This source of uncorrelated opposite-sign muon pairs is called "combinatorial background", and its characterization and simulation are described in the following Section (the discussion mainly profits from the material contained in [77, 66]).

5.1 The Combinatorial Background

Any experiment measuring dimuon production needs to take into account that a fraction of the measured opposite-sign (OS) muon pairs are not due to dimuons, i.e. $\mu^+\mu^-$ pairs produced together, by conversion of a virtual photon in the decay of a resonance (as in the case of the η, ρ, ω and ϕ mesons of interest for the present analysis) or in a $q\bar{q}$ annihilation (as in the Drell-Yan process which gives anyway no significant contribution to the low mass dimuon spectrum).

5.1.1 Do We Have Like-Sign Correlated Muon Pairs?

Among the muon pair sources which do not originate from resonance decays, we have already described the "open charm" process, in which the creation of a $c\bar{c}$ pair and the subsequent hadronization (fragmentation) of the charmed quarks, leads to the creation of two D mesons, whose semi-muonic decays originate a muon pair. In the open charm process the muon pairs are still correlated, since they trace back to the same partonic event. Moreover, at the SPS energies charm production is a rare process, and we never have more than one pair of charmed mesons produced in the same collision: it means that from $D\bar{D}$ production we cannot get like-sign (LS) muon pairs. This is not the case − for instance − at LHC energies, where so many charmed hadrons are produced that they will also originate uncorrelated muon pairs.

There are other processes which lead to correlated muon pair contributions. For instance, there are events where a single string fragments into a pair of high-p_{T} pions, necessarily of opposite charge, which subsequently decay semi-muonically. The same is true for the events where a ρ decays into a $\pi^+\pi^-$ pair, followed by the simultaneous decay of both pions into muons. The probability for these processes to take place is anyway so small that they can be safely neglected − as it was done in the present analysis.

We can conclude, then, that no physics process is able to give a significant contribution in terms of correlated LS muon pairs at the SPS energies: which is to say, that the LS component observed in the data is a *pure* sample of uncorrelated muon pairs. As we will see, this represents the basis of the procedure for the evaluation of the background.

5.1.2 Uncorrelated OS Muon Pairs in NA60

The origin of the "combinatorial background" muon pairs in NA60 is the simultaneous semi-muonic decay of pions and/or kaons. The shorter decay length of the kaons partially compensates for their lower production yield, leading to almost equal numbers of muons from pion or kaon decays.

The probability that a given pion/kaon decays before being stopped by the hadron absorber is completely independent on the probability that another pion/kaon will also decay. Therefore, from the numbers of like-sign muon pairs, N^{++} and N^{--}, we can determine the corresponding number of opposite-sign background muon pairs, given by $N^{+-} = 2\sqrt{N^{++}N^{--}}$. However, this relation does not account for possible correlations between the two muons: it means that the ratio between the opposite-sign combinatorial background and the expression $2\sqrt{N^{++}N^{--}}$ is in general different from 1; we will indicate this factor as R, and factorize it into a term R_{ch} accounting for correlations at the production level, and a term R_{exp} accounting for correlations induced by the experimental conditions. In the next paragraphs we will describe this two kinds of correlations.

5.1.3 Correlations at the Production Level

In general, pions and kaons are produced with intrinsic correlations, in particular due to the conservation of electric charge; for this reason, R_{ch} is often referred to as "charge correlation factor". Such charge correlations become non negligible in the case of (low energy) p-p collisions, when the total multiplicity of charged particles is particularly small: in these collisions, in fact, it is more likely to produce opposite-sign than like-sign muon pairs. The charge correlation factor R_{ch} is a function of the dimuon mass, rapidity and transverse momentum, and should be estimated through Monte Carlo simulations, by means of event generators.

In the case of high multiplicity collisions, such as high-energy heavy-ion collisions, it is clear that the very high number of produced pions and kaons smears out completely any charge correlation that may exist at the production level. In such collisions, hence, the R_{ch} factor must be unity, except in the most peripheral collisions, where a value slightly higher than 1 can be understood. This expected behavior has been reproduced by Monte Carlo simulations in the framework of the NA50 analysis of the intermediate mass dimuons [2].

In the case of p-A collisions, the effects of charge correlations are expected to be more important and should depend on the specific target nuclei under consideration. The exact value of R_{ch} will also depend on the interaction rate, determining the level of pile-up integrated for each event. The statistics collected by NA60 in p-A collisions does not allow a reliable evaluation of the R_{ch}, so that in the present work we exploited the results obtained in the analysis of the NA50 p-A data, sharing approximately the same running conditions of the 2004 p-A in NA60. From the NA50 analysis, an average value $R_{ch} \simeq 1.20$ has been derived, without significant dependence on the nuclear target. This will be the reference value for our analysis, its uncertainty being properly propagated to the final results as a systematic error.

5.1.4 Correlations Induced by the Detector Conditions

We have just seen how that two muons may be correlated at the production level, because of the charge correlation effect. However, the main source of correlation in a pair of measured muons usually comes from detector-induced effects, which are accounted for by the R_{exp} factor: this leads to a total R factor different from unity even when $R_{ch} \simeq 1$. The R_{exp} factor can be identified with the ratio between OS and LS muon-pair acceptances:

$$R_{exp} = \frac{A^{+-}}{\sqrt{A^{++} \cdot A^{--}}} \,. \tag{5.1}$$

In the NA38 and NA50 experiments, from which NA60 inherited the muon spectrometer, this ratio of acceptances (which include the effect of the trigger conditions) was forced to be unity by the use of the so-called "image cut": a measured event would only be kept for further analysis if the muon pair would still comply to the

acceptance and trigger conditions when any of the muons would have its charge reversed. This selection cut reduces the data sample to the fraction of events verifying $A^{+-} = A^{++} = A^{--}$, thereby simplifying the background subtraction procedure at the expense of significantly reducing the available statistics (especially for low mass dimuons).

The HELIOS-3 experiment, for instance, could not apply such a selection cut and, therefore, had an effective R factor of 1.57 ± 0.10 in p-W collisions, clearly dominated by correlations induced by the detector effects. Indeed, HELIOS-3 had a dipole magnet in the target region and a trigger condition which required one of the muons above the beam line and the other below. Given the orientation of the dipole field lines, it was much easier to fulfill this condition when the pair of muons had opposite charge: one would be detected upwards, the other downwards. It is clear that the R factor must be much higher in such a case, to compensate for the much lower trigger/acceptance probabilities of the like-sign muon pairs. It should be also clear, from this example, that this $R_{\rm exp}$ factor must depend on the kinematical variables of the dimuon. In certain corners of phase space the ratio between OS and LS detection acceptances may be completely different from other regions, so that we cannot approximate $R_{\rm exp}$ by a single constant factor.

The NA60 experiment also has a dipole magnet in the target region and a trigger condition which imposes that the two muons must be in different sextants of the scintillator hodoscopes. Therefore, the muon-pair acceptances are influenced by geometrical effects which can be rather different for OS and LS pairs, and which are very difficult to incorporate in a (multidimensional) $R_{\rm exp}$ function. The procedure which has been followed in NA60 is quite different indeed, and consists in evaluating the OS background through a "mixed event" technique. This means that we combine a single muon of a LS muon pair with single muons of another LS event, thereby building mixed events $++$, $--$ and $+-$ data samples, with the formed muon pairs satisfying the trigger conditions. Building the combinatorial background with the event mixing technique allows one to check that the built and measured LS event samples have compatible shapes, before using the generated OS sample to estimate the combinatorial background in the measured OS spectra.

The event mixing technique should be carefully handled, for what concerns the way the events are selected for the mixing. For example, since the "pools" of positive and negative single muons used in the event mixing are necessarily obtained from dimuon triggers and, therefore, biased by the dimuon trigger condition that requires the two muons to be in different sextants, the single muons used for the event mixing must be selected with probabilities which depend on the sextant (and on the muon charge). These probability factors depend on the ACM and PT7 polarities and, hence, have been evaluated for each of the four field polarity combinations separately. Further details on the procedure can be found in [77] and [66].

5.1.5 The Combinatorial Background in the Real Mass Spectrum

The mixing event technique provides us with a sample of OS and LS mixed events with their kinematical distributions. As long as the detector-induced effects are properly taken into account, via the $R_{\rm exp}$ factor, the mass profiles obtained for the LS $++$ and $--$ samples should reproduce those of the corresponding samples observed in the real data.

The comparison between the real and mixed LS components also allows one to evaluate the proper normalization for the combinatorial background present in the measured OS spectrum: it is sufficient to propagate to the real data the ratio $N^{+-}/2\sqrt{N^{++}N^{--}}$ given by the mixed event samples, which contains the effect of the $R_{\rm exp}$ factor. This normalization must then be finally corrected, as already noticed, for the charge correlation factor, $R_{\rm ch}$. Any selection applied to the real events, furthermore, must be obviously propagated in the definition of the corresponding combinatorial background. This is the case of the selections imposed by the dimuon-target association criterion, as well as the selection imposed by the cut on the matching χ^2 for the single muons.

Mixed and real LS samples are compared in Figure 5.1 for the case in which the target identification for the dimuons is not required; the same comparison, this time including the dimuon-target association selection criteria but still integrating over the targets, is shown in Figure 5.2. The corresponding real mass spectra and normalized OS combinatorial backgrounds are shown in Figure 5.3. As one can see, both requiring and not requiring the target identification for the dimuons, the LS component of the real data is well reproduced by the event mixing technique.

The level of the combinatorial background, estimated from the LS component of the real data, accounts for less than 10% of the integrated mass spectrum below 1.4 GeV/c^2. Furthermore, from the comparison between the mixed and real LS samples, the accuracy of the background subtraction can be estimated to be within a $\sim$ 10% uncertainty at worst. Thus, even assuming a 10% uncertainty on the background subtraction, this would translate in no more than a global $\sim$ 1% uncertainty on the low mass spectrum: this ensures a rather robust and reliable basis for the subtraction of the combinatorial background from the real mass spectrum.

5.1.6 Impact of the Muon Track Matching and Fake Matches Background

The muon track matching, described in Chapter 3, affects the background level. Clearly, the muon track matching significantly reduces the population of muons from pion and kaon decays, either because the decay happens after the vertex telescope and the muon track does not match the parent track, or because the decay happens within the telescope, and the decay kink invalidates the track reconstruction. The ratio between the estimated combinatorial background and the measured opposite-sign dimuons drops from $\sim$ 30% at the PC level to $\sim$ 10%, as seen, at the VT level,

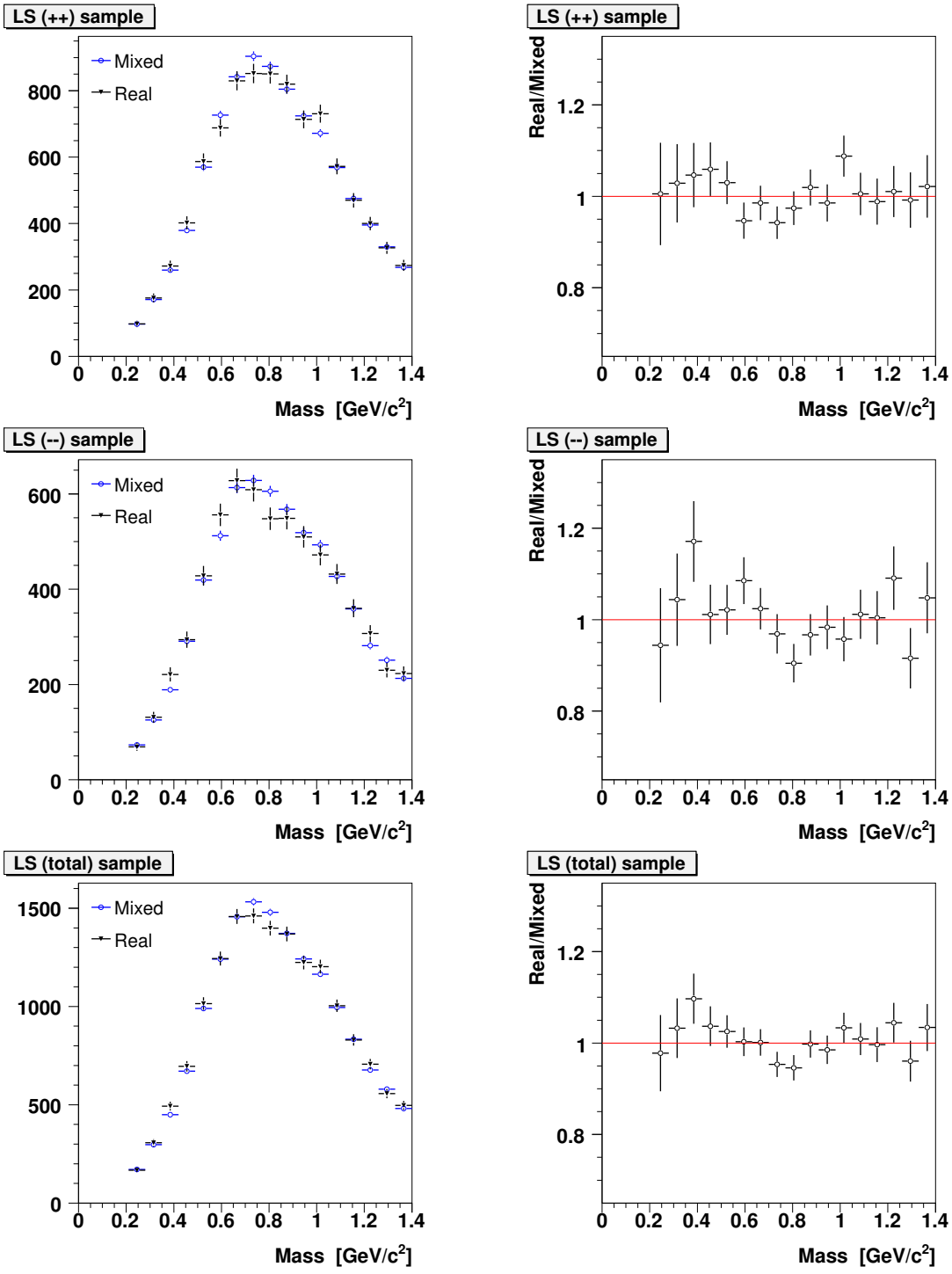

Figure 5.1: *Comparison between mixed and real LS samples. Target identification is not required.*

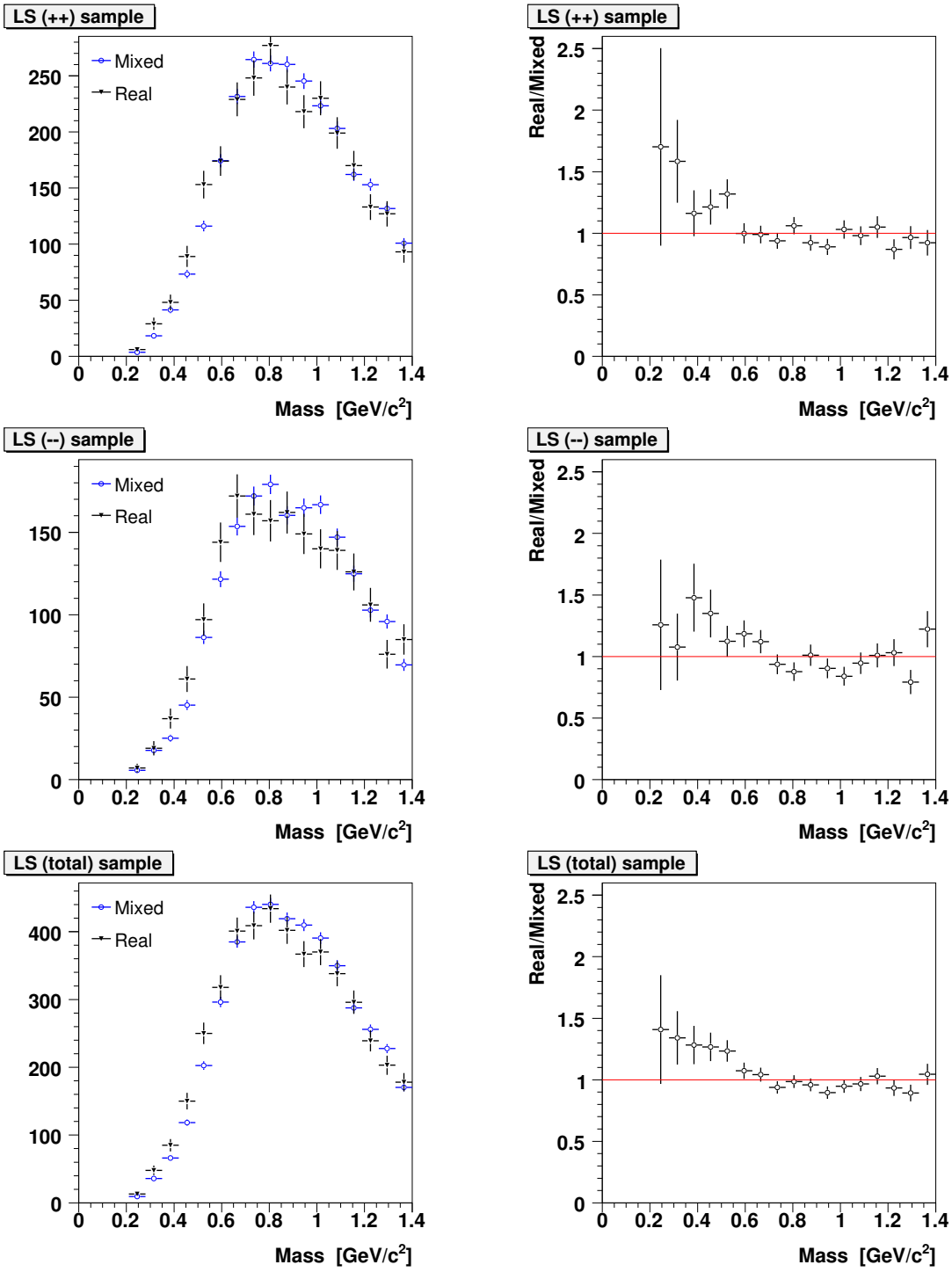

Figure 5.2: *Comparison between mixed and real LS samples. Target identification is required here.*

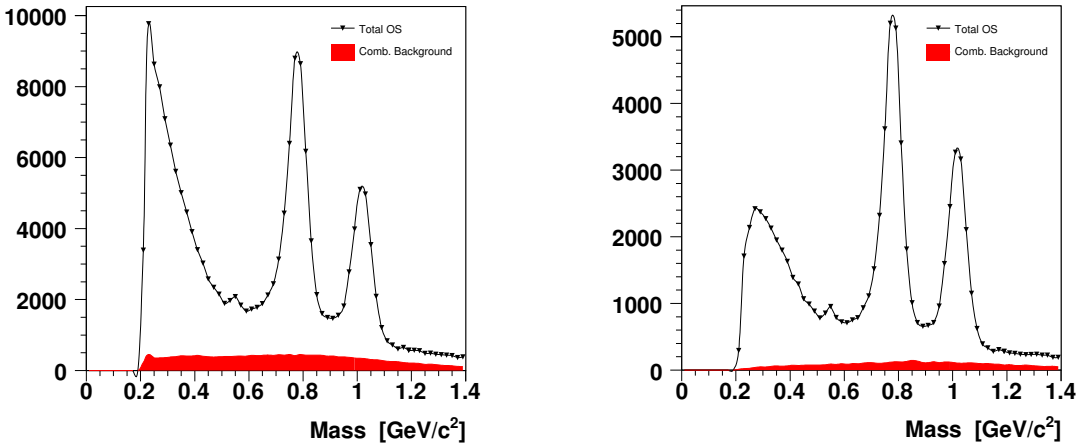

Figure 5.3: *OS real mass spectrum and combinatorial background, not requiring (left) and requiring (right) the target identification for the dimuons.*

integrated over all dimuon masses.

A priori, we could consider wrongly matched dimuons (often called "fake matches") as an additional background source. This contribution is rather small in proton-nucleus collisions, since the average multiplicities are quite low; for comparison, in the In-In data it accounted for $\sim 10\%$ of the combinatorial background. As explained in Chapter 3, when more than one match candidate is found for a given PC muon, only the one having the best $\chi^2_{\rm match}$ is retained. The few cases where accidentally the wrong track is taken (fake match) will, hence, lead at most to a degraded mass resolution for the ρ/ω and ϕ resonances, but will not give rise to an increased dimuon yield: this effect, and its probability to occur, are automatically taken into account when performing MC simulations of the whole event − in our case by exploiting an existing real event with an overlay simulation − so that the degraded resolution is included in the reconstructed MC line shapes used for describing the real data.

5.2 The Real Mass Spectrum

Once the combinatorial background has been subtracted from the raw mass spectrum, one is left with a sample of correlated muon pairs, which in proton-nucleus collisions − where no deconfined medium is created − can be explained in terms of the superposition of the known sources already listed and discussed in the previous Chapter. They include:

- Dalitz decays of η, ω and η' mesons, through the processes $\eta \to \mu^+\mu^-\gamma$, $\eta' \to \mu^+\mu^-\gamma$ and $\omega \to \mu^+\mu^-\pi^0$;

- 2-body decays of the η, ρ, ω and ϕ mesons;
- semi-muonic decays of correlated pairs of charmed mesons (open charm).

We will now address the problem of how these sources are disentangled from the total dimuon spectrum.

5.2.1 Mass Spectrum for the Single Targets

We first consider the separate dimuon samples for each production target. The main step, of course, consists in reproducing in the MC all the features included in the real data − selections, kinematics cuts, reconstruction efficiencies. In our analysis, the MC events are built starting from real events on top of which a muon pair is generated, with the kinematics given by the generator − as described in the previous Chapter. The MC events are then reconstructed in exactly the same way as the real events, in order to reproduce the reconstruction efficiency affecting the real data.

For each target we then build the MC reconstructed mass profiles for each process, so that their superposition can be directly compared with the observed mass spectrum for the given target, see Figure 5.4. The available statistics for each target is reported in Table 5.1, together with the mass resolution for the ω and ϕ peaks as observed in the real data. In the comparison, the three Be targets are summed together. Slight mass shifts, up to the level of 0.5%, have also been applied target by target, tuned on the ϕ peak, in order to properly match real data and MC mass profiles.

As it can be seen, the *reconstructed* MC histogram for a given process have different shapes in different production targets, because the acceptance profile as a function of mass is in general a function of the geometrical position of the production target. This is particularly evident, for instance, when considering the reconstructed MC profile for the Dalitz decay of the η meson, which looks rather different when going from the most upstream to the most downstream target; it can be appreciated in Figure 5.4, where we show the mass spectra for the single targets, integrated over p_T, together with the superposition of the MC processes considered in the fit: from this same picture, one can also observe how the strong differences between the mass spectra of the various targets − mainly induced by the target identification criterion − are well reproduced by the MC simulations.

The same reasoning stands for the acceptance × efficiency factors, whose dependence on the z-position of the production target is determined by the different geometrical acceptance coverage of the various targets. Other target-dependent effects can also be identified, such as the dependence of the reconstruction efficiency on the tracks multiplicity in the interaction vertex, where the target-dependence now depends on the nuclear number A, instead on the geometrical position along z. A-dependent and z-dependent effects convolute in the observed acceptance × efficiency factors, which are shown in Figure 5.5 as a function of the z position of the production target.

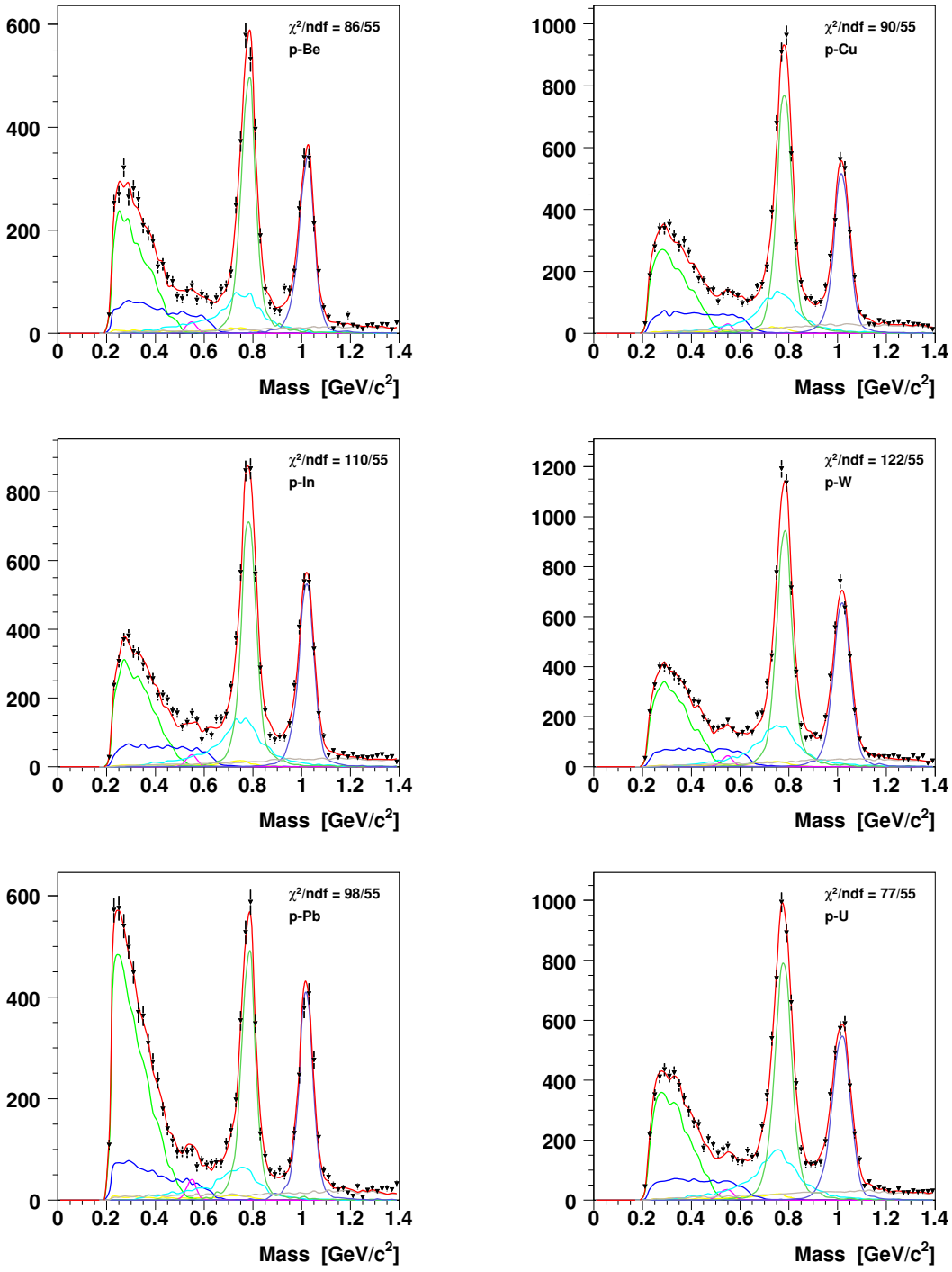

Figure 5.4: *p_T-integrated raw pass spectra, for each production target, together with the superposition of the MC processes describing the data.*

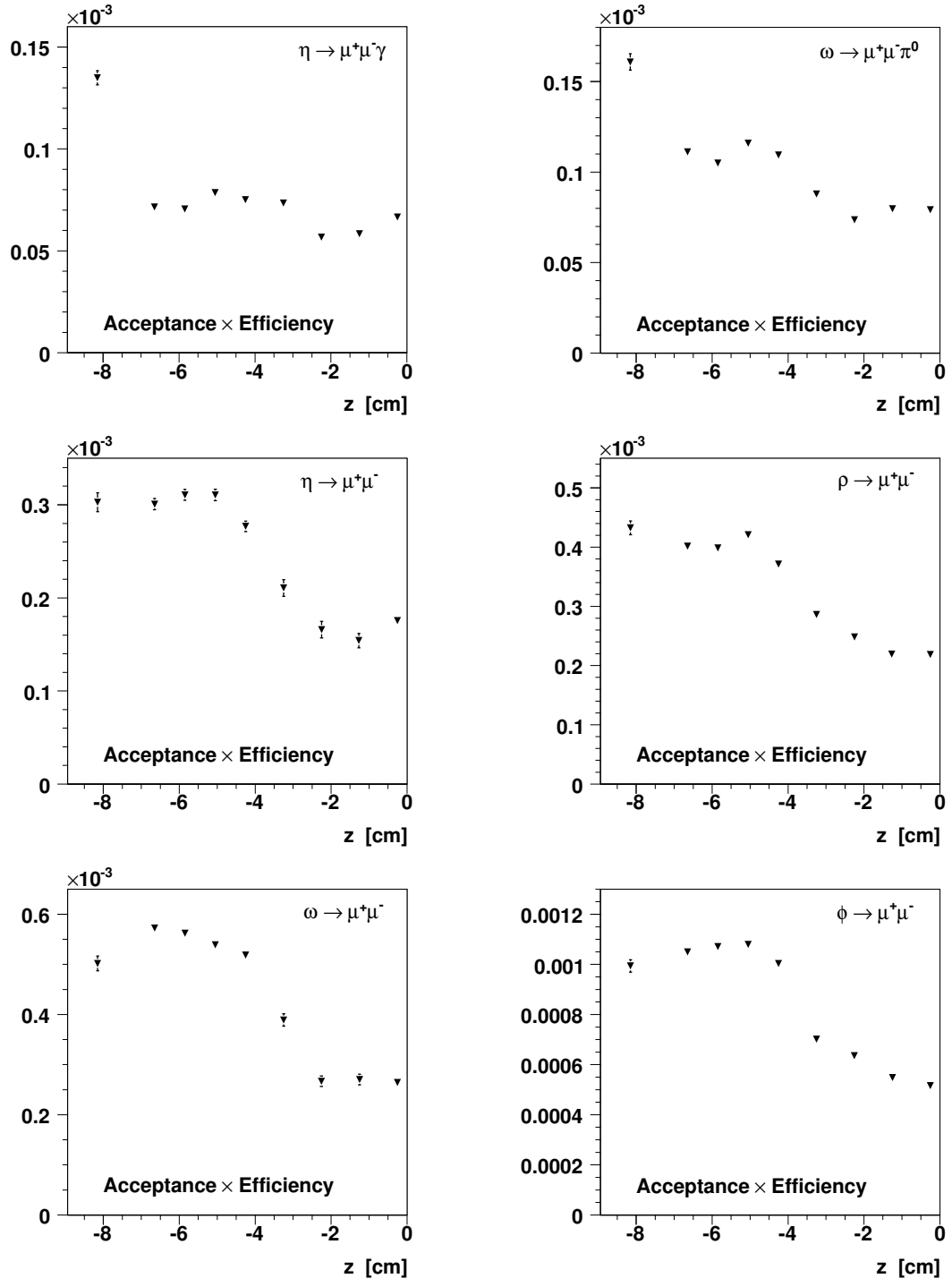

Figure 5.5: *Full phase space acceptance × efficiency factors, for the relevant processes involved in this analysis. The z-increasing order of the targets is: Al, U, W, Cu, In, Be1, Be3, Be3, Pb. The Al target was not considered in the present analysis.*

5.2.2 Mass Spectrum Target-Integrated

In addition to the single-target mass spectra, the target-integrated mass spectrum is also considered when considering observables for which no target-dependence is expected, as for the case of the electromagnetic transition form factors (see Chapter 8). A point to be carefully considered, when the target-integrated sample is built, is the way in which the shape of the MC histograms and the acceptance $\times$ efficiency factors are evaluated.

Proper weights must be defined when summing over the single targets, as it is explained in details in the the following paragraphs.

In first place, we consider the target-integrated acceptance $\times$ efficiency factors. In this case, we note that if each target had the same probability to produce a dimuon for the given process, we could actually average over the factors for each target. But in general, as in our case, the probability to produce a dimuon for a given process depends on the target, being proportional to some weight w_i. The weights w_i depend upon the following factors:

- the beam intensity arriving each target, which decreases going downstream because of the beam attenuation in the upstream targets;
- the number of scattering nuclei which a proton of the beam finds along his path when traversing each target, thus depending on the thickness and the density of the targets;
- the production cross section of the mother particle for the considered process, which scales proportionally to A^{α}.

The first two points define what we call the "target-luminosity" factors $\mathscr{L}_i$, i.e. factors which are proportional to the probability of having a proton-nucleus interaction within each target:

$$\mathscr{L}_i \propto \frac{\exp\left(-\sum_{j<i}\lambda_i\right)\cdot\left(1-e^{-\lambda_i}\right)}{A^{\alpha_{\text{inel}}}}\,, \tag{5.2}$$

where λ_i represents the thickness of the i-th target, expressed in terms of number of interaction lengths for a proton. In this way, $1-e^{-\lambda_i}$ is the fraction of protons interacting with the i-th target, and $\exp(-\sum_{j<i}\lambda_i)$ is the fraction of beam which arrives the i-th target, after having being partially absorbed by each of the j-th upstream targets. Dividing by $\sigma_{\text{inel,p-A}} = A^{\alpha_{\text{inel}}}$, with $\alpha_{\text{inel}} = 0.7186 \pm 0.0007$, we recover the number of scattering nuclei, see also [50]. The $\mathscr{L}_i$ factors will play a crucial role in the study of the nuclear dependence of the production cross sections, allowing us to properly "equalize" the extracted particle yields for each target. They are shown in Table 5.1, arbitrarily normalized to 1.

In order to include the dependence on the production cross section, one has in addition to consider a reasonable hypothesis for the α parameters of each particle. As we will see, these parameters are determined within this same analysis, thus defining

Target	Events	σ_ω [MeV/c^2]	σ_ϕ [MeV/c^2]	$\mathscr{L}_{\text{tgt}}$ [a.u.]
Be	8 674	33 ± 4	32 ± 3	0.6680
Cu	13 305	30 ± 2	31 ± 3	0.1135
In	13 041	29 ± 4	34 ± 3	0.0662
W	16 620	30 ± 2	35 ± 3	0.0559
Pb	11 106	27 ± 3	32 ± 3	0.0570
U	15 952	38 ± 5	40 ± 4	0.0395

Table 5.1: *Statistics available for each production target and other informations relevant for the analysis.*

a self-consistent approach. In any case, even large uncertainties on the α parameters only marginally affect the weights w_i, so that the impact on the final averaged value for the acceptance $\times$ efficiency factors is almost negligible.

Once the weights w_i are known for each process, being proportional to the probability for the given process to take place in each target, the target-integrated acceptance $\times$ efficiency factor can be obtained as a weighted average on the acceptance $\times$ efficiency factors evaluated for the single targets:

$$\left(\frac{\text{rec}}{\text{gen}}\right)_{\text{tot}} = \frac{w_1 \cdot \left(\frac{\text{rec}}{\text{gen}}\right)_1 + \ldots + w_9 \cdot \left(\frac{\text{rec}}{\text{gen}}\right)_9}{w_1 + w_2 + \ldots w_9} = \frac{\sum_i w_i \cdot \left(\frac{\text{rec}}{\text{gen}}\right)_i}{\sum_i w_i} ,$$

i.e. a weighted average of the $(\text{rec}/\text{gen})_i$ ratios for the single targets, where the weights are the w_i evaluated as described above.

Weighting the Reconstructed MC Mass Histograms

The target-integrated reconstructed MC mass histogram must also be built properly weighting the histograms for the single targets. In this case, however, we must perform a further step with respect to the previous discussion on the acceptance $\times$ efficiency factors, because the weight now also accounts for the $\left(\text{rec}/\text{gen}\right)_i$ of the targets. As a result, the target-integrated reconstructed MC mass histogram is built weighting the histograms for the single targets, normalized to 1, using as weights the factors $w_i \cdot \left(\text{rec}/\text{gen}\right)_i$ instead of w_i only.

5.2.3 Fit on the Raw Mass Spectrum

The comparison between the real mass spectrum and the superposition of the MC spectra, either for a single target or a target-integrated analysis, is performed by opti-

mizing the normalization β_i of each MC process.

If the MC histograms used as input for the fit are normalized to unity, the β_j parameters correspond to the numbers of reconstructed events estimated for each process. Correcting these numbers for their acceptance × efficiency factors, we get the number of generated events for each given process: from here, dividing by the associated branching ratio, the yield of the parent particles can be evaluated. For instance, the yield of the ϕ meson is evaluated from its 2-body decay as follows:

$$N_\phi = \frac{\beta_{\phi\to\mu\mu}}{A_{\phi\to\mu\mu}\cdot BR_{\phi\to\mu\mu}} \,. \tag{5.3}$$

The acceptance × efficiency factors are always defined in the full phase space, unless the fit is restricted to a particular kinematic region (e.g. in a particular bin of p_T): in this latter case, both the acceptance × efficiency and the output yields refer to the kinematic region of the fit. According to the conditions under which the fit is performed (single-target or target-integrated, in full phase space or in a particular kinematic region), dedicated procedures are considered, as follows.

Target-Integrated, Full Phase Space

In this case the full available statistics is exploited: all the processes can reliably independently normalized, apart from the contribution of the Dalitz decay of the η', whose cross section is kept fixed to the one of the ω meson. This procedure is adopted either considering or ignoring the selections imposed by the dimuon-target association criterion. In Figure 5.6 we show the fit of the target-integrated mass spectrum, in the full phase space, both excluding (top panels) and including (bottom panels) the target identification for the dimuons. Labels are also shown in order the various MC processes can be identified and their contribution appreciated.

Single Target, Full Phase Space

Here the statistics is still sufficiently large to permit a reliable normalization of the Dalitz decay of the η and the 2-body decays of the ρ, ω and ϕ mesons, for which the dependence on the nuclear number A can be studied. The open charm is also left free, being mainly constrained by the mass region above the ϕ mass. Concerning the decays $\eta \to \mu^+\mu^-$ and $\omega \to \mu^+\mu^-\pi^0$, they are fixed to the $\eta \to \mu^+\mu^-\gamma$ and $\omega \to \mu^+\mu^-$ decays, respectively, through their relative branching ratios. Since these ratios are clearly independent on the nuclear number A, they are fixed to the values obtained performing a fit on the target-integrated spectrum. The ratio $\sigma_{\eta'}/\sigma_\omega$ is also fixed, as in the previous case.

Single-Target, Differential in p_T

In this case the available statistics only allows one a reliable evaluation of the yield of the Dalitz decay of the η and the 2-body decays of the ω and ϕ mesons. The

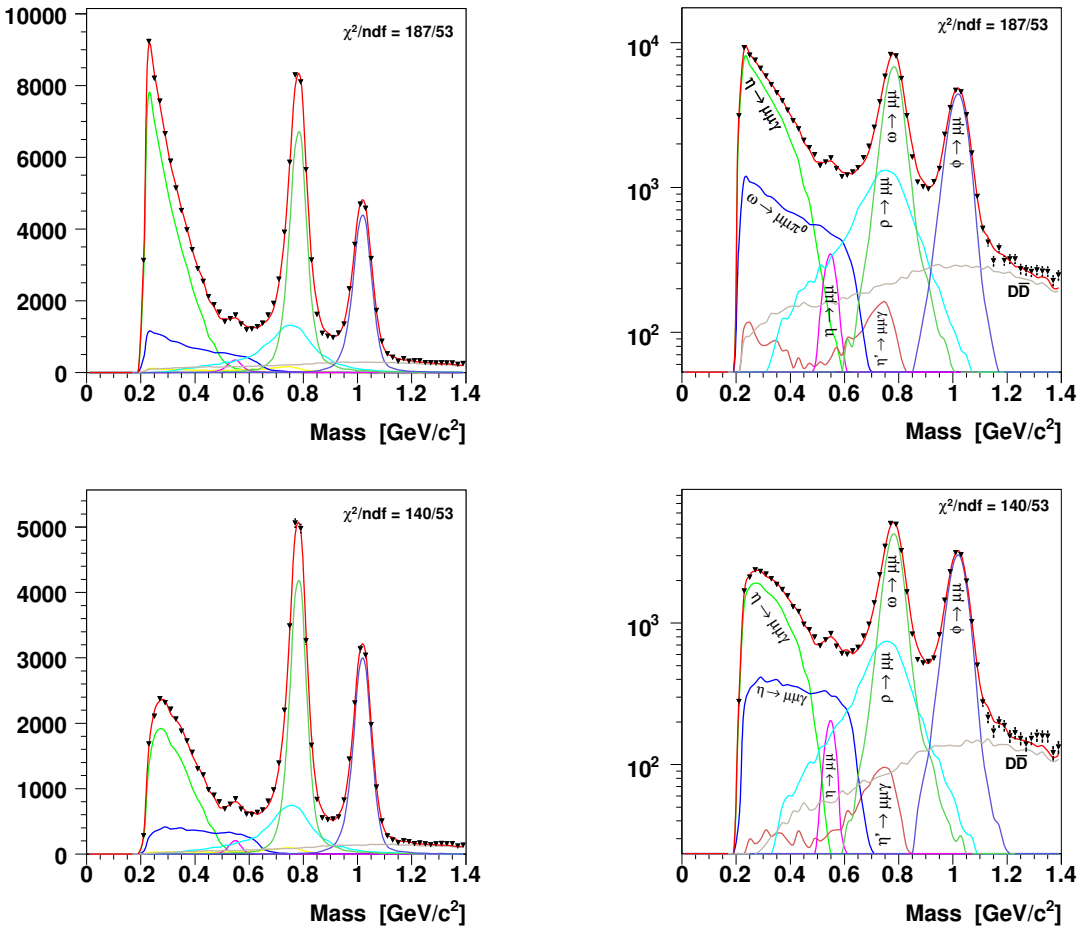

Figure 5.6: *Target-integrated raw pass spectra without requiring (top panels) and requiring (bottom panels) the identification of the production target for the dimuons. The superposition of the MC processes describing the data is also shown, where each process can be identified by the corresponding label.*

open charm contribution is left free as usual, while the ρ contribution is fixed to the ω using the ratio $\sigma_\rho/\sigma_\omega$ estimated on the single-target fits performed in full phase space. The relative branching ratios for the minor decays of the η and ω mesons are kept fixed as in the previous case, as also the ratio $\sigma_{\eta'}/\sigma_\omega$.

6

Transverse Momentum Spectra

In this Chapter we describe the analysis of the transverse momentum spectra for the vector mesons ω and ϕ and for the pseudoscalar meson η. For the η meson, its 2-body decay being strongly suppressed (see Chapter 4), we rely on the measure of its Dalitz decay $\eta \to \mu^+\mu^-\gamma$. However, since the third body is not measured in NA60, the kinematics of the parent decaying meson is not fully recovered, and the p_T distribution of the η has then to be inferred from the p_T distribution of the detected muon pair.

6.1 Fit on the Raw Mass Spectra

The preliminary step for the analysis of the p_T distributions consists in dividing the real dimuon sample, target by target, into p_T bins of 200 MeV. The available statistics is significant up to $p_T \sim 2.0$ GeV/c. The same selection is then applied to the MC spectra for all the sources described in Chapter 4, as well as for the contribution accounting for the combinatorial background.

For each target and p_T bin, a fit is then performed on the raw mass spectrum. In this way, the contributions coming from the decays of the η, ω/ρ and ϕ mesons can be evaluated, and a raw p_T spectrum can be extracted for each process. The raw p_T spectrum can then be corrected for the acceptance $\times$ efficiency as a function of p_T, as given by the MC simulations. It should be noted that, for sufficiently narrow p_T bins, this correction is independent on the p_T function used as input for the MC simulations, apart residual smearing effects which can be neglected since the bin width considered here is larger than the p_T resolution of the apparatus.

For this analysis, the fits on the mass spectrum have been performed optimizing the yield of the $\eta \to \mu^+\mu^-\gamma$, $\omega \to \mu^+\mu^-$ and $\phi \to \mu + \mu^-$ processes. The normalization of the small open charm contribution was also left free, while the other four

ingredients of the hadronic cocktail were kept fixed by means of four numerical parameters. These parameters have been varied defining several configurations of input parameters for each fit, so that the uncertainty on their values could propagate in the systematic uncertainty on the final results. The procedure and the criteria followed for the evaluation of the systematics on the results for the p_T distribution, are reported in details in the next Sections.

In order to give an idea of the profile of the mass spectrum in each bin of p_T, we show in Figure 6.1 the fit on the mass spectrum in each p_T bin, for one of the targets available for the present analysis − namely the Indium target.

6.1.1 Acceptance × Efficiency Correction vs p_T

The p_T profile of the acceptance × efficiency results from a complex convolution of several factors: the geometric acceptance of the vertex telescope, the geometric requirements embedded in the trigger logic of the muon spectrometer (which asks for the two muons to belong to different sextants), and the combination of the magnetic fields provided by the dipole magnet in the vertex region and the toroidal magnet in the muon spectrometer after the absorber. A non-negligible effect due to the application of the dimuon-target selection also contributes in defining the level and the shape of the acceptance.

In Figure 6.2 we show the acceptance as a function of p_T, for the dimuons coming from the three processes $\eta \to \mu^+\mu^-\gamma$, $\omega \to \mu^+\mu^-$ and $\phi \to \mu + \mu^-$. For each process, the p_T acceptance is shown for the Uranium, Indium and Lead targets, respectively sitting in the initial, central and final part of the target system. As one can see, the acceptance profiles for the three targets share common trends; the Pb target, on the other hand, has a significantly smaller acceptance with respect to the other two targets, both for the $\omega \to \mu^+\mu^-$ and $\phi \to \mu + \mu^-$ decays, in the whole p_T range with the exception of the last two bins.

The p_T acceptance of the NA60 apparatus in the 2004 p-A run, for the low mass dimuons, decreased by a factor as large as ~ 10 with respect to the performances of the In-In run. This was due to a combination of several factors, the most important being the replacement of 40 cm of graphite with 40 cm of iron in the final part of the hadron absorber: in addition to enhance the fraction of low mass (and low p_T) dimuons stopped inside the absorber, this results in a slightly degraded kinematics for the muons measured in the muon spectrometer, which in turn reduces the performances of the matching with the vertex tracks. Other factors contributing to the loss of acceptance are the reduced tracking efficiencies both for the muon spectrometer (due to 5 MWPC broken planes) and the vertex spectrometer (one tracking plane permanently switched off and the other having much reduced efficiencies with respect to the In-In run, because of aging effects), as well as the strong selections imposed in the analysis for the identification of the production target, because of the high level of pile-up during the p-A run.

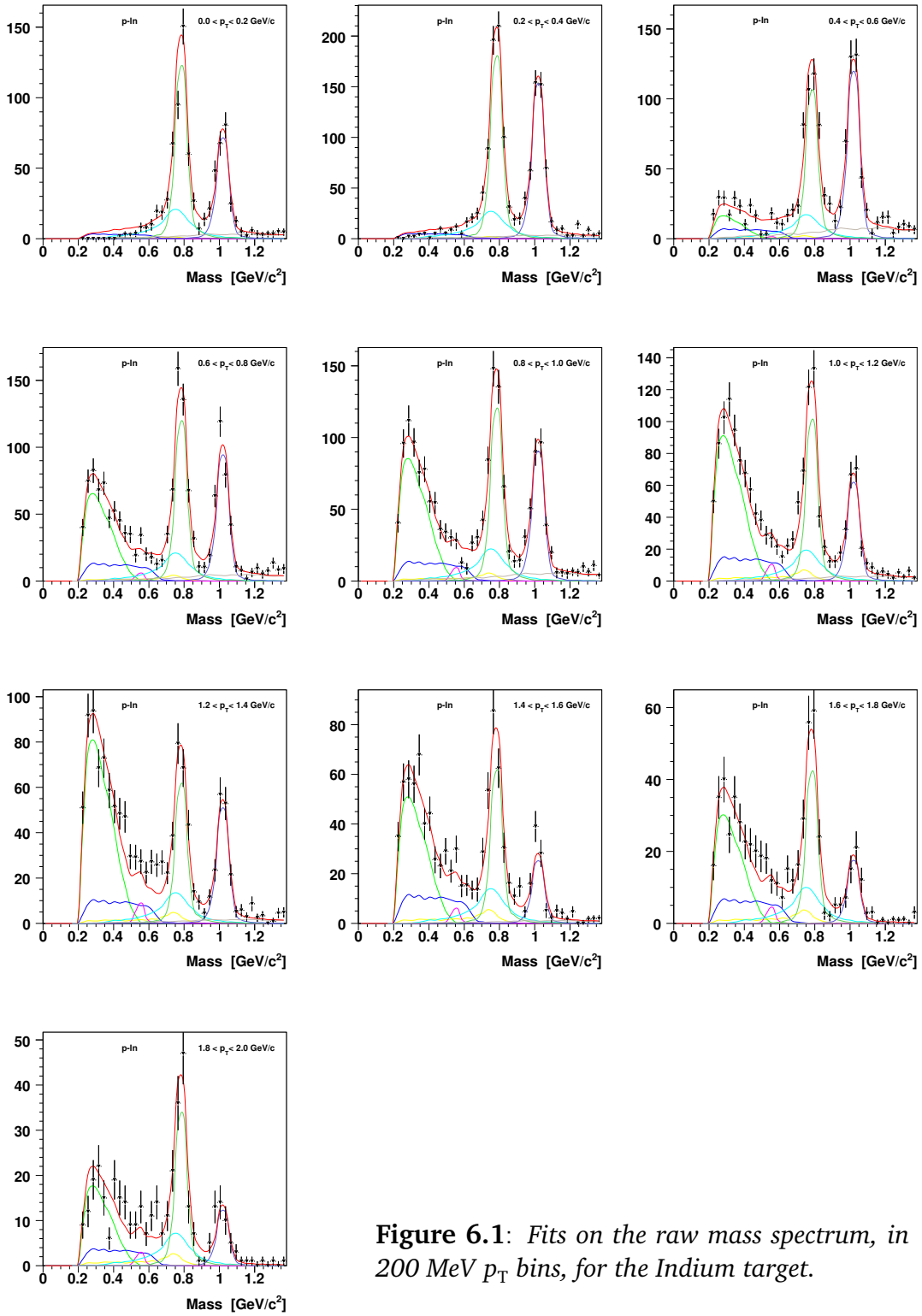

Figure 6.1: *Fits on the raw mass spectrum, in 200 MeV p_T bins, for the Indium target.*

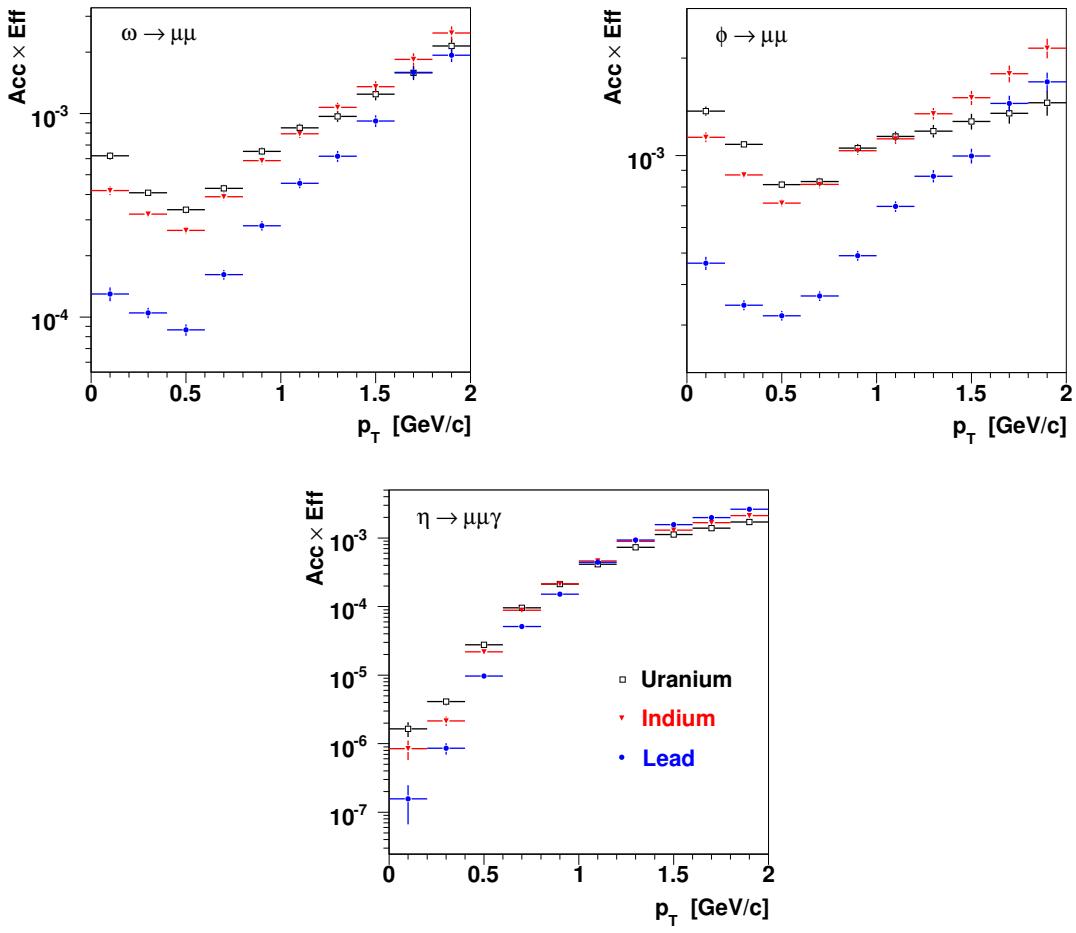

Figure 6.2: *Acceptance × efficiency profiles for the Uranium, Indium and Lead targets, for the three processes* $\eta \to \mu^+\mu^-\gamma$, $\omega \to \mu^+\mu^-$ *and* $\phi \to \mu + \mu^-$.

6.2 Evaluation of the Systematic Uncertainties

In the previous Section we described how the corrected p_T spectra are build up, starting from the fits on the raw mass spectra. As mentioned, the procedure which has been followed involves the definition of several parameters in order each mass spectrum fit to be performed. The resulting "input configuration" has been varied in order the systematic uncertainties on the results to be evaluated, with the various choices of the input parameters, whose role is described below. The details given in this section also hold for the analyses presented in the next Chapters.

Cross Section Ratio $\sigma_{\eta'}/\sigma_{\omega}$

The contribution of the Dalitz decay of the η' mesons, namely through the process $\eta' \to \mu^+\mu^-\gamma$, accounts for a very small fraction of the total dimuon spectrum, because of its small production cross section. Because of its small yield and its continuum shape, without any dominant structure apart from the broad peak at the ρ mass (due to the contribution of the ρ to the η' form factor), the fit on the reconstructed mass spectrum is not sensible to this contribution. So one has to rely on the prediction of the models: in particular, the statistical model predicts a $\sigma_{\eta'}/\sigma_{\omega} = 0.12$ in cold nuclear matter [28].

For each choice of the input configuration, the ratio $\sigma_{\eta'}/\sigma_{\omega}$ is translated to a ratio between the processes $\eta' \to \mu^+\mu^-\gamma$ and $\omega \to \mu^+\mu^-$; this latter is then properly scaled for each p_{T} bin using the p_{T} distributions used as input in the MC for the generation of the ω and η' kinematics. Values $\sigma_{\eta'}/\sigma_{\omega} = 0.06$, 0.12, 0.18 (integrated over p_{T}) have been considered for the evaluation of the systematics.

Combinatorial Background Normalization

The effect of the uncertainty on the estimation of the combinatorial background has been studied by varying the level of the combinatorial background to be subtracted from the mass spectrum before this latter is fitted with the superposition of the hadronic sources.

The uncertainty on the normalization of the combinatorial background mainly reflects the uncertainty on the value of the charge correlation factor, as well as on its possible dependence on p_{T}. The combinatorial background component has then been scaled by a factor R_{BKG}, which has been varied within a broad range of values. In this case, variations up to $\sim 20\%$ have been considered for the R_{BKG} factor, with respect to the "default" value $R_{\mathrm{BKG}} = 1.20$.

Normalization of the Open Charm Contribution

Concerning the contribution of the open charm process to the mass spectrum, it should be noted that it is the only source, among those included in the fit, giving a significant contribution to the mass region above the mass of the ϕ: in this way, the fit optimizes the level of the open charm process basically by maximizing its contribution in the mass region between 1.2 and 1.4 GeV/c^2. In doing so, our estimation of the open charm level is biased by the fact that we are neglecting any other possible source, in particular the Drell-Yan, being relevant in the mass spectrum above the ϕ mass but giving no appreciable contribution for lower masses. In order to study the corresponding systematic effects, we have repeated the analysis fixing the open charm contribution to 80% and 60% of the level which is obtained when its contribution is left free.

Cross Section Ratio $\sigma_\rho/\sigma_\omega$

Performing the fit in several p_T bins strongly reduces the statistics available for each target, resulting in the impossibility of properly disentangling the ρ contribution under the ω peak. This is the reason because we decided to fix the ratio $\sigma_\rho/\sigma_\omega$ when performing the fits on the mass spectra as a function of p_T. The ratio $\sigma_\rho/\sigma_\omega$ is experimentally known to be close to the unity, and this same analysis has studied its variation as a function of the production target, integrated over p_T: the results, reported in the next Chapter, show that the $\sigma_\rho/\sigma_\omega$ is approximately independent on the production target, and its value is compatible with the hypothesis $\sigma_\rho/\sigma_\omega = 1$.

In this case, the parameter has been varied within $\sim$ 10%. This uncertainty is only relevant for the analysis of the p_T spectrum for the ω meson, hardly affecting the results for the ϕ.

Relative Branching Ratios for the η and ω Mesons

The normalization of the $\eta \to \mu^+\mu^-$ and $\omega \to \mu^+\mu^-\pi^0$ processes also needs a considerable amount of statistics to be properly fixed by the fit. These two processes cannot be left free, then, when performing the fit on the mass spectrum target by target or, as in the present case, even in various bins of p_T.

For this reason, the relative branching ratios $BR(\eta \to \mu\mu)/BR(\eta \to \mu\mu\gamma)$ and $BR(\omega \to \mu\mu\pi^0)/BR(\omega \to \mu\mu)$ have been fixed to the values cited by the Particle Data Group (PDG). The uncertainty on these ratios is propagated as a systematic error to the final results.

On this regard, it has already been pointed out (see Chapter 4) that the analysis of the peripheral In-In data recently reported a updated value for the $\omega \to \mu^+\mu^-\pi^0$ branching ratio, now included in the 2010 edition of the PDG review. The NA60 In-In value corrects the 2008 one by a factor $\sim$ 1.8, so that the new value cited in the 2010 PDG review is $BR(\omega \to \mu\mu\pi^0) = 1.3 \pm 0.4$, approximately 35% larger then the 2008 edition.

In the present analysis we optimize to our target-integrated data both the correction factors to be applied to the $\eta \to \mu^+\mu^-$ and $\omega \to \mu^+\mu^-\pi^0$ branching ratios, considering variations as large as 50% for the evaluation of the systematics. Concerning the correction factor for the $\omega \to \mu^+\mu^-\pi^0$ branching ratio, in addition, a dedicated analysis will be reported in Chapter 8, where its measurement will also be described and reported; on the contrary, a detailed analysis for the $\eta \to \mu^+\mu^-$ branching ratio is still under investigation so that no measurement will be quoted in this work.

Matching χ^2

Another parameter defining the input configuration for the fit on the raw mass spectrum is the matching χ^2 upper cut for the single muons composing the dimuons. Besides the standard cut $\chi^2_{\text{match}} < 3.0$, described and justified in Chapter 3, the alter-

native options $\chi^2_{\text{match}} < 2.5$ and $\chi^2_{\text{match}} < 2.0$ have also been considered. It should be noted that, in this case, the choice of the parameter must be coherently propagated in the evaluation of the acceptance × efficiency correction, as well in determining the shape of the MC histograms to be used in the fit of the mass spectrum.

Generation Settings for the MC

The last systematic check has been performed varying the way in which the production vertices are chosen when performing the MC simulations with the overlay technique, as described in Chapter 4. This check basically accounts for the systematic uncertainties on the acceptance × efficiency factors considered in the analysis.

6.2.1 Computing the Systematic Uncertainties

The systematic uncertainty for a given measured quantity could be defined as the RMS, or the standard deviation, or any other parameter describing the dispersion of the available measurements for the considered quantity. Although, it is quite clear that the estimation of the systematic uncertainty resulting from this definition is strongly biased by the choice of the systematic checks considered within the analysis. One may, for instance, consider 10 different values of a parameter having no influence at all on the final results, and 10 values for a parameter which − on the contrary − induces strong fluctuations: this would result in a distribution of values strongly peaked around a given value, although only a part of the considered checks are relevant for the evaluation of the systematics.

A possible way to avoid that the arbitrariness in the choice of the systematic checks could bias the estimation of the resulting systematic uncertainty, consists in defining a criterion which separately considers each systematic check separately, discarding it if not relevant for the evaluation of the systematics. A possible criterion has been proposed by R. Barlow (for example in [27]), and consists of the following steps, to be performed for each value x_i coming out from an independent systematic check:

- the value x_i is compared with the final value X, and the quantity $\Delta = |x_i - X|$ is defined;
- the statistical errors associated to x_i and X are also compared, and the quantity σ_Δ is defined as $\sigma^2_\Delta = |\sigma^2_{x_i} - \sigma^2_X|$
- if the discrepancy Δ between the i-th check and the final value is smaller than σ_Δ, the x_i value is assumed to be in agreement with the final value X, and nothing is done;
- if, on the contrary, Δ is found to be *larger* than $n\sigma_\Delta$, the discrepancy between x_i and X is tagged as significant, and Δ contributes in quadrature to the total systematic uncertainty on X.

6.3 ϕ and ω p_T Distributions

The ϕ and ω p_T spectra resulting after the correction for the acceptance $\times$ efficiency are shown in Figures 6.3–6.4 as a function of the transverse mass m_T, and in Figures 6.5–6.6 as a function of p_T^2. These spectra have been compared to the theoretical distributions given by the models, as explained in the following.

6.3.1 Fit with the Exponential Function

The first comparison is performed considering the thermal-like function already cited in Chapter 1:

$$\frac{1}{p_T}\frac{dN}{dp_T} = \frac{1}{m_T}\frac{dN}{dm_T} = 2\frac{dN}{dp_T^2} \propto \exp\left(-\frac{m_T}{T}\right) . \tag{6.1}$$

According to this parametrization, the transverse mass of the particle m_T, or, better, the quantity $(m_T - m_0)$, should be distributed according to a pure exponential law, with an effective "temperature" T.

Performing a fit on the p_T distributions for the ω and ϕ mesons, one can immediately appreciate how the thermal hypothesis clearly fails in describing the whole spectra up to 2 GeV/c. The observed m_T spectra for the ω and the ϕ are reported in Figure 6.3 and Figure 6.4: in both cases, they systematically show a deviation from a pure exponential trend for high m_T, with the only exception of the m_T spectrum of the ϕ meson in the Pb target, for which possible systematic effects related to the acceptance and reconstruction efficiency correction (it is the last target before the vertex spectrometer) are still under investigation. For each spectrum, the fit with the exponential function is performed up to the $(m_T - m_0)$ value corresponding to $p_T = 1.4$ GeV/c, where the thermal hypothesis seems to describe the data reasonably well (solid, red line); the extrapolation of the fit function up to the upper end of the available m_T range is shown with a dashed, blue line, helping to appreciate the contribution of the hard tail at high p_T.

The T values defined from the fits shown above are compiled in Table 6.1, where both statistical and systematic uncertainties are reported.

6.3.2 Fit with the Power Law

The results from the fit with the exponential function can be interpreted as an evidence for some different mechanism being responsible for the high-p_T component of the observed spectra. The superposition of a thermal-like distribution at low p_T and a hard tail at high p_T can be described by means of the following function, used for example by the HERA-B Collaboration to describe the p_T^2 spectrum of the ϕ meson [3]:

$$\frac{dN}{dp_T^2} \propto \left(1 + \frac{p_T^2}{p_0^2}\right)^{-\beta} . \tag{6.2}$$

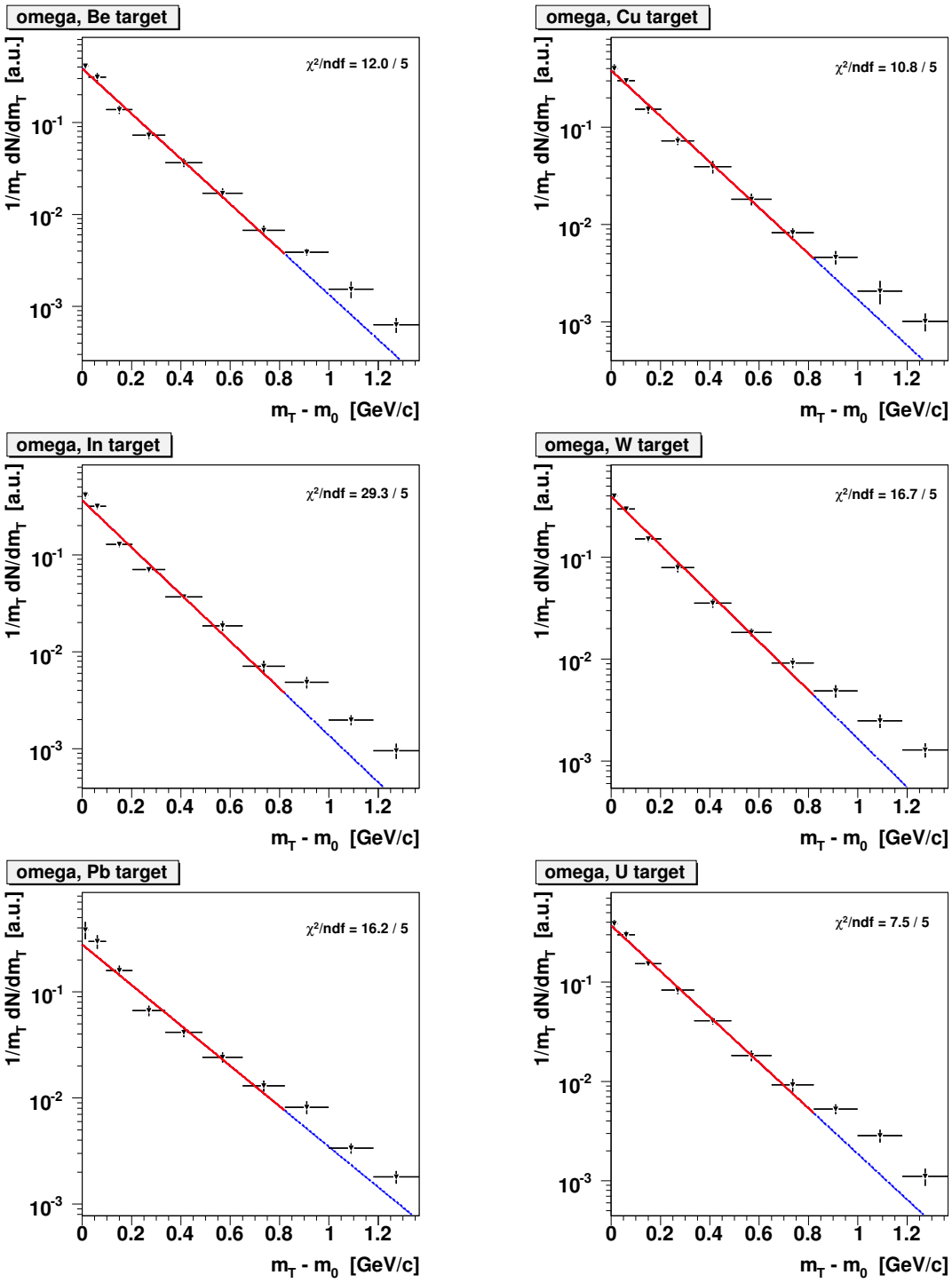

Figure 6.3: *Fits on the acceptance-corrected m_T spectra of the ω, for each production target.*

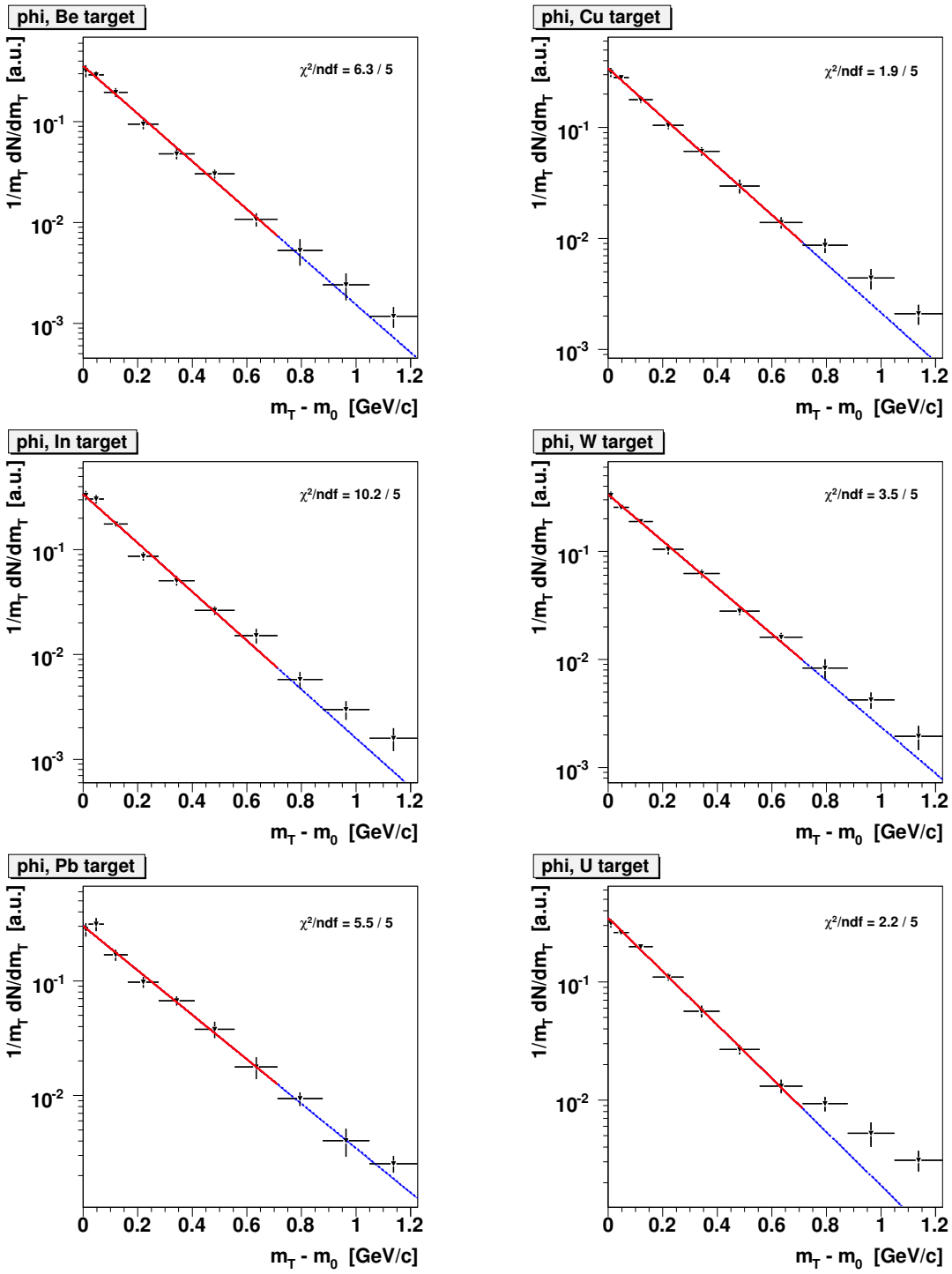

Figure 6.4: *Fits on the acceptance-corrected m_T spectra of the ϕ, for each production target.*

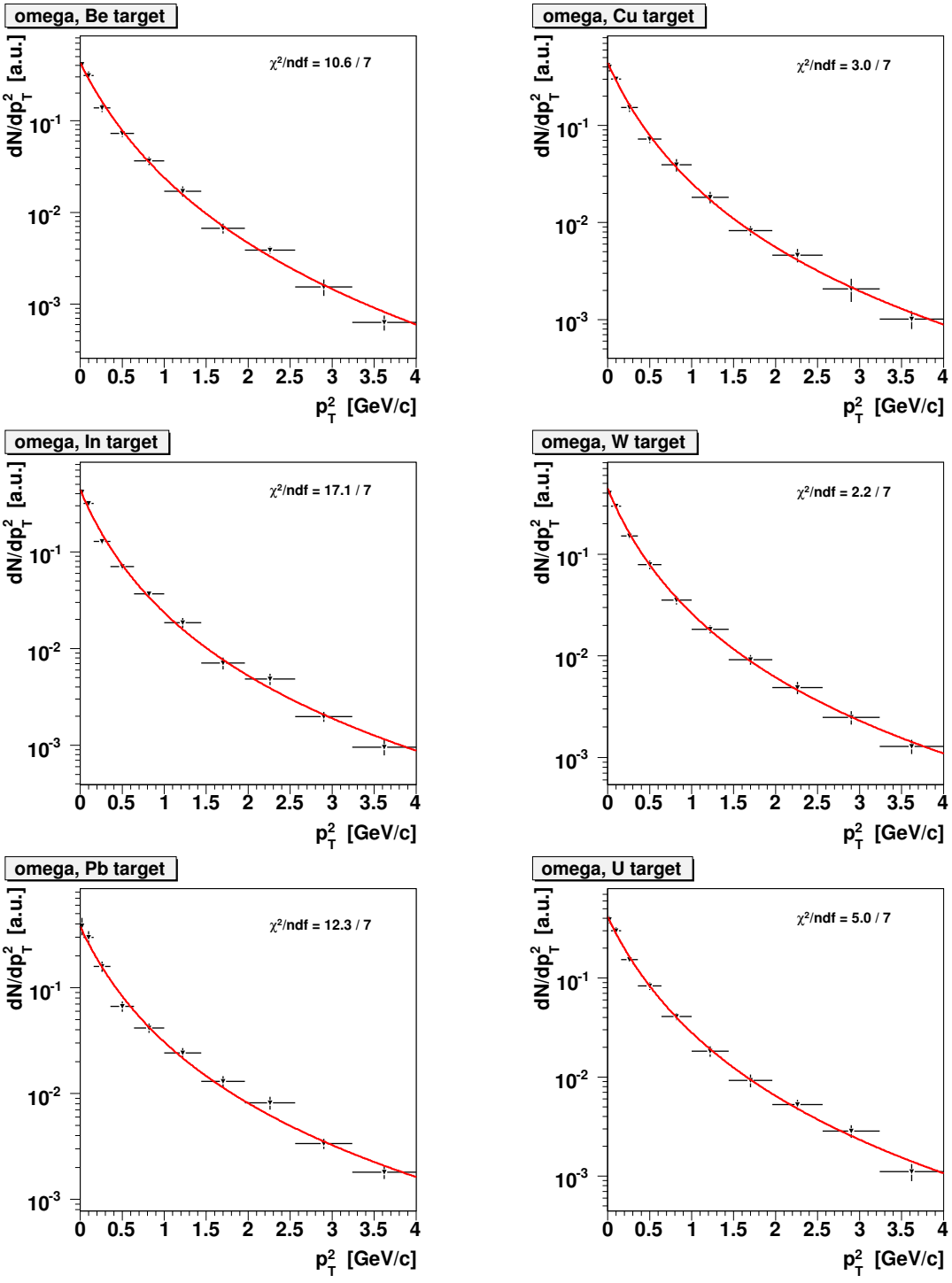

Figure 6.5: *Fits on the acceptance-corrected p_T^2 spectra of the ω, for each production target.*

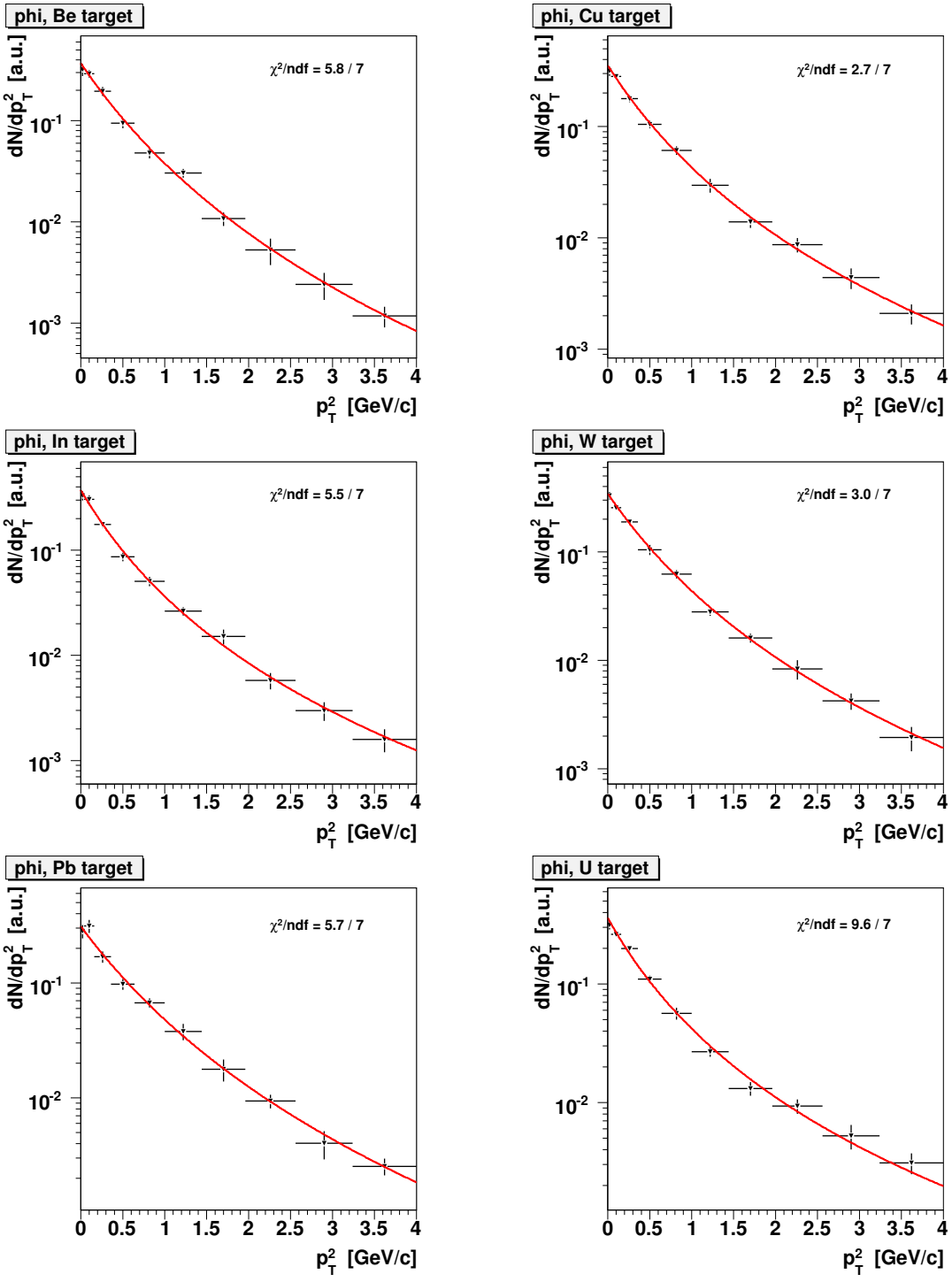

Figure 6.6: *Fits on the acceptance-corrected p_T^2 spectra of the ϕ, for each production target.*

As already noted in Chapter 1, this is a standard form for a mixture of soft $(1+\ldots)$ and hard processes $(p_T^{-\beta})$.

The dN/dp_T^2 distributions and the fits are reported in Figure 6.5 and Figure 6.6, respectively for the ω and ϕ mesons. As one can see, the fits successfully extend up to the upper end of the available p_T^2 range, suggesting that the functional form (6.2) is adequate to describe the dN/dp_T^2 distribution in the whole range considered in the present analysis.

As for the T values coming out from the exponential fit, the β and p_0^2 parameters are listed in Table 6.1 with their statistical and systematic uncertainties.

6.3.3 Results for the ω and ϕ Mesons

The results of the analysis on the transverse momentum spectra for the ω and ϕ mesons are compiled in Table 6.1. The fit parameters are presented with their statistical and systematic uncertainties. In the case of the T parameters, the evaluation of the systematic uncertainty also considers two choices for the upper limit of the m_T range on which the fit with the exponential function (6.1) is performed: this accounts for the arbitrariness with which this upper limit is chosen, since we have no way to define with precision the limits of the p_T range where the thermal-like part of the distribution dominates on the hard tail.

The final values for the T, β and p_0^2 have been estimated as the mean values of the available systematic checks. The same procedure has been followed for the evaluation of their final statistical uncertainty.

6.3.4 Discussion of the Results

The analysis of the transverse momentum spectra for the ω and ϕ mesons clearly shows how the observed p_T distribution for both the particles cannot be explained by the exponential function (6.1) in the full p_T range accessed. On the contrary, the full p_T range is well described by the power-law parametrization (6.2).

No significant trend for the p_0^2 or β parameter, as a function of the production target, can be deduced from the fit results within the statistical and systematic uncertainties. To get more insight on this aspect, in Table 6.2 we compile the mean value of p_T for each target, as extracted from the corresponding power-law fit function. The errors associated to each value of $\langle p_T \rangle$ reflect the statistical and systematic uncertainties on the p_0^2 or β parameters.

No definite trend as a function of the target can be identified here, too. This justifies the comparison between the target-integrated values − profiting from a better statistical accuracy:

$$\langle p_T \rangle_{\omega}^{\text{NA60, p-A}} = 0.61 \pm 0.03 \pm 0.03 \text{ GeV}/c \qquad \langle p_T \rangle_{\phi}^{\text{NA60, p-A}} = 0.70 \pm 0.04 \pm 0.02 \text{ GeV}/c \ .$$

We can conclude, thus, that we observe the mean p_T for the ϕ meson to be higher than that of the ω meson, while no evidence of target-dependence is found.

Comparison with NA27 and HERA-B

The results obtained for the p_T spectra of the ϕ and ω mesons can be compared with the available experimental results. The NA27 Collaboration, for instance, measured the η, ρ, ω and ϕ production in p-p collisions at $\sqrt{s} = 27.5$ GeV [76]. Their p_T points for the η meson will be considered in the next Section; in the original paper, they have been fitted with the same power-law (6.2) considered in this work. On the contrary, no data point is shown for the p_T of the ρ, ω and ϕ mesons, for which only the fit results are given, relative to the function:

$$\frac{dN}{dp_T^2} \propto e^{-\delta p_T^2} . \tag{6.3}$$

The quoted values for the δ parameter are: $\delta_\rho = 2.59 \pm 0.10$ (GeV/c)$^{-2}$, $\delta_\omega = 2.25 \pm 0.16$ (GeV/c)$^{-2}$, $\delta_\phi = 2.98 \pm 0.35$ (GeV/c)$^{-2}$. From here, we have evaluated

Target		T [MeV]	p_0^2 [GeV^2/c^2]	β
ω	Be	$179 \pm 4 \pm 7$	$0.98 \pm 0.11 \pm 0.13$	$4.07 \pm 0.24 \pm 0.27$
	Cu	$185 \pm 4 \pm 10$	$0.79 \pm 0.10 \pm 0.12$	$3.45 \pm 0.22 \pm 0.24$
	In	$184 \pm 4 \pm 7$	$0.69 \pm 0.09 \pm 0.08$	$3.27 \pm 0.20 \pm 0.15$
	W	$185 \pm 4 \pm 11$	$0.66 \pm 0.07 \pm 0.02$	$3.08 \pm 0.16 \pm 0.12$
	Pb	$223 \pm 10 \pm 22$	$0.74 \pm 0.14 \pm 0.08$	$2.94 \pm 0.24 \pm 0.17$
	U	$188 \pm 4 \pm 10$	$0.82 \pm 0.10 \pm 0.10$	$3.40 \pm 0.21 \pm 0.23$
	ALL	$\mathbf{188 \pm 2 \pm 9}$	$\mathbf{0.76 \pm 0.03 \pm 0.05}$	$\mathbf{3.31 \pm 0.07 \pm 0.13}$
ϕ	Be	$183 \pm 6 \pm 6$	$1.83 \pm 0.42 \pm 0.23$	$5.27 \pm 0.83 \pm 0.46$
	Cu	$198 \pm 6 \pm 6$	$1.50 \pm 0.31 \pm 0.09$	$4.13 \pm 0.55 \pm 0.16$
	In	$188 \pm 6 \pm 13$	$1.21 \pm 0.22 \pm 0.10$	$3.90 \pm 0.43 \pm 0.22$
	W	$202 \pm 6 \pm 5$	$1.73 \pm 0.33 \pm 0.08$	$4.50 \pm 0.56 \pm 0.19$
	Pb	$222 \pm 9 \pm 16$	$2.11 \pm 0.58 \pm 0.43$	$4.90 \pm 0.90 \pm 0.61$
	U	$192 \pm 5 \pm 1$	$1.14 \pm 0.21 \pm 0.19$	$3.44 \pm 0.39 \pm 0.41$
	ALL	$\mathbf{193 \pm 2 \pm 5}$	$\mathbf{1.27 \pm 0.10 \pm 0.07}$	$\mathbf{3.81 \pm 0.17 \pm 0.07}$

Table 6.1: *Fit parameters for the p_T spectra of the ω and ϕ mesons.*

$\langle p_T \rangle$ [GeV/c]		
Tgt	ω	ϕ
Be	$0.57 \pm 0.04 \pm 0.05$	$0.64 \pm 0.11 \pm 0.06$
Cu	$0.60 \pm 0.05 \pm 0.06$	$0.70 \pm 0.11 \pm 0.03$
In	$0.59 \pm 0.05 \pm 0.04$	$0.66 \pm 0.09 \pm 0.04$
W	$0.62 \pm 0.05 \pm 0.03$	$0.70 \pm 0.10 \pm 0.03$
Pb	$0.69 \pm 0.10 \pm 0.06$	$0.72 \pm 0.15 \pm 0.10$
U	$0.62 \pm 0.05 \pm 0.06$	$0.73 \pm 0.11 \pm 0.11$
ALL	$\mathbf{0.61 \pm 0.03 \pm 0.03}$	$\mathbf{0.70 \pm 0.04 \pm 0.02}$

Table 6.2: $\langle p_T \rangle$ *for each production target, as obtained from the power-law fit functions.*

the mean p_T for each particle, and the following results have been found:

$$\langle p_T \rangle_\rho^{\text{NA27}} = (0.551 \pm 0.011)\ \text{GeV}/c \qquad \text{(p-p)}$$
$$\langle p_T \rangle_\omega^{\text{NA27}} = (0.591 \pm 0.021)\ \text{GeV}/c \qquad \text{(p-p)}$$
$$\langle p_T \rangle_\phi^{\text{NA27}} = (0.513 \pm 0.030)\ \text{GeV}/c \qquad \text{(p-p)}.$$

As one can see, the $\langle p_T \rangle$ for the ω extracted from the fit function of NA27 agrees with the estimate obtained in the present analysis. Disagreement is found, instead, for the $\langle p_T \rangle$ of the ϕ, both quantitatively and qualitatively: quantitatively, since our measurement is at more that 4 (statistical) standard deviations from the NA27 one; qualitatively, since we observe $\langle p_T \rangle_\phi > \langle p_T \rangle_\omega$ while the NA27 results indicate that $\langle p_T \rangle_\phi < \langle p_T \rangle_\omega$.

Concerning the p_T measurement for the ϕ meson, we can also compare our measurement with the one by the HERA-B Collaboration [3], which also measured ϕ production (in the K^+K^- channel) in p-C, p-Ti and p-W collisions at $\sqrt{s} = 41.6$ GeV. Keeping in mind the different energies, it is still interesting to compare our p_T measurements to the HERA-B ones, since the p_T distributions are described in both cases with the power-law function (6.2).

As an evidence, no definite trend is observed for the mean p_T of the ϕ as a function of the target, within the cited errors by HERA-B:

$$\langle p_T \rangle_\phi^{\text{HERA-B}} = (0.66 \pm 0.09)\ \text{GeV}/c \qquad \text{(p-C)}$$
$$\langle p_T \rangle_\phi^{\text{HERA-B}} = (0.66 \pm 0.14)\ \text{GeV}/c \qquad \text{(p-Ti)}$$
$$\langle p_T \rangle_\phi^{\text{HERA-B}} = (0.72 \pm 0.09)\ \text{GeV}/c \qquad \text{(p-W)}.$$

As one can notice, all these values are fully compatible with the mean p_T for the ϕ measured in the present analysis. In particular, for the Tungsten target common to both NA60 and HERA-B data, we get:

$$\langle p_T \rangle_\phi^{\text{HERA-B, p-W}} = (0.72 \pm 0.09)\ \text{GeV}/c \qquad \langle p_T \rangle_\phi^{\text{NA60, p-W}} = (0.70 \pm 0.10 \pm 0.03)\ \text{GeV}/c\ .$$

This result is coherent with the fact that the p_0^2 and β parameters measured by HERA-B are compatible with the parameters shown in Table 6.1 for the present analysis. In particular, for the Tungsten target we have:

$$p_0^2(\text{NA60}) = 1.73 \pm 0.33 \pm 0.08\ \ (\text{GeV}/c)^2 \qquad p_0^2(\text{HERA-B}) = 1.65 \pm 0.14\ \ (\text{GeV}/c)^2$$

$$\beta(\text{NA60}) = 3.81 \pm 0.17 \pm 0.07 \qquad \beta(\text{HERA-B}) = 4.20 \pm 0.14\ .$$

6.4 Transverse Momentum Spectrum for the η Meson

As extensively pointed out, the measurement of the p_T spectrum for the η meson has to be inferred from the p_T spectrum of the dimuon produced in the Dalitz decay $\eta \to \mu^+\mu^-\gamma$. This latter, in turn, can only measured for $p_T > 0.6$ GeV/c, because under this limit the acceptance becomes so small that the process cannot be identified at all in the raw mass spectrum.

The corrected p_T spectrum for the η-Dalitz dimuon cannot be directly fitted with the theoretical parametrizations describing the p_T of the mother particle. In this case, thus, one has to generate several p_T distributions for the parent η meson, each characterized by a pair of parameters (p_0^2, β); for each of them, the corresponding p_T distribution for the dimuon of the Dalitz decay can be extracted with a MC simulation of the decay; at the end, the MC p_T distribution for the η-Dalitz dimuon which best fits the corresponding distribution extracted from the data, defines the pair of parameters (p_0^2, β) corresponding to the "correct" p_T spectrum for the parent decaying η meson.

6.4.1 Measured p_T Spectrum for the η-Dalitz Dimuon

As a first step, the corrected p_T spectrum for the η-Dalitz dimuon has been extracted from the data, following exactly the same procedure described for the p_T spectra of the ω and ϕ mesons − with the only relevant difference that in this case the p_T spectrum is limited to the range $p_T > 0.6$ GeV/c. On the basis of the ω and ϕ results, any possible dependence on the production target is neglected here, so that the target-integrated p_T spectrum of the η Dalitz dimuon is directly considered here.

In this case, the systematic uncertainty has been directly evaluated for the content of each p_T bin. For each bin, the content and the statistical error are averaged over the values available from the systematic checks, while the systematic uncertainty is evaluated filtering the systematic checks with the same Barlow's criterion described in Section 6.2.1.

This procedure gives a final p_T spectrum in which the error bars associated to the content of each bin are the sum in quadrature of the final statistical and systematic uncertainties. This final p_T spectrum is then compared with the MC p_T spectra, each corresponding to a different pair of parameters (p_0^2, β) defining the p_T of the parent η meson, in order to find the best match.

6.4.2 χ^2 Plot for the η-Dalitz Dimuon p_T Spectrum

In order to have an estimation of the parameters (p_0^2, β) defining the best match between the MC and observed p_T distribution for the η-Dalitz dimuon, a grid of 80×80 (p_0^2, β) pairs of parameters have been considered. For the p_0^2 parameter, the range $0.10 \leq p_0^2 < 4.10$ has been probed, with 0.05 GeV$^2/c^2$ steps. For the β parameter, the range $2.0 \leq \beta < 10$ has been considered, covered with 0.1 wide steps.

For each pair of parameters considered, the MC p_T spectrum is compared with the one extracted from the real data, and the quality of the comparison has been evaluated in terms of the χ^2 quantity defined as:

$$\chi^2 = \sum_i \frac{(\mathrm{MC}_i - \mathrm{Real}_i)^2}{\sigma^2_{\mathrm{Real}_i}} , \tag{6.4}$$

where the index i defines the i-th bin of the MC and real histogram, and the sum is defined over the bins included in the range $p_T > 0.6$ GeV/c for which we have a significant acceptance coverage, see Figure 6.2. The plotted quantity is actually the χ^2 divided by the number of bins involved in the sum, i. e. the "reduced χ^2". At the end of the procedure, the χ^2 surface shown in Figure 6.7 has been found. From the analysis of this plot one should infer the (p_0^2, β) pair which minimizes the difference between the MC and the real distributions, looking at the minimum of the χ^2 surface. The minimum is approximately located in the point indicated by the white star: the final results are:

$$p_0^2 = 2.50 \pm 0.40 \ \ [\mathrm{GeV}/c]^2 \qquad \beta \simeq 6.10 \pm 0.50 ,$$

where the errors are obtained considering the region for $\chi^2/\mathrm{ndf} < 1$. Actually, as the figure clearly shows, the position of the minimum is only loosely constrained, since several (p_0^2, β) pairs, distributed along a diagonal band, share approximately the same degree of compatibility with the distribution extracted from the data. The reason for this should be probably related to the fact that we are comparing MC and data in the range $p_T > 0.6$ GeV/c: the lower limitation cuts off the region around the maximum of the p_T distribution from the comparison, and it translates in a large uncertainty on the evaluation of the best (p_0^2, β) parameters. The ambiguity could only be removed gaining access to the region between 0.3-0.5 GeV/c, where the turning point of the p_T distribution for the η-Dalitz dimuon is approximately located.

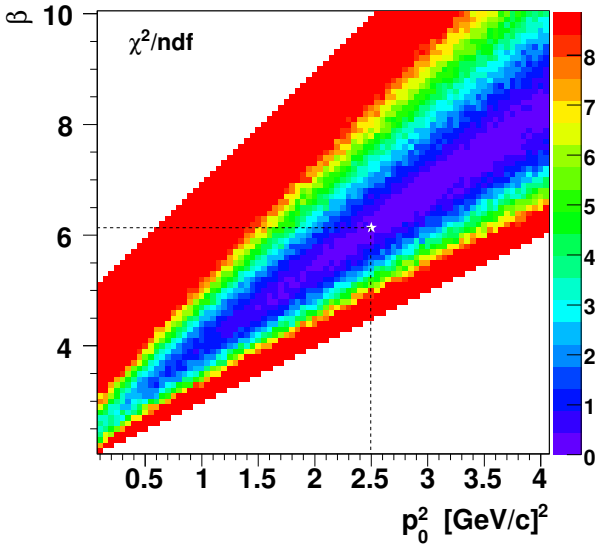

Figure 6.7: *χ^2 plot for the p_T distribution of the η-Dalitz dimuon. The "best" (p_0^2, β) are distributed on a minimum "valley", extending all along the plot.*

6.4.3 Discussion of the Results

Our observations for the p_T of the η meson can be compared with a number of experimental points coming from various experiments, these latter ranging over a large interval of p_T. We consider here the collection of data points reported in [75], where they have been translated to $\sqrt{s} = 29.1$ GeV assuming a Bourquin-Gaillard parametrization for the scaling of p_T with $\sqrt{s}$. Since our data sample is taken at $\sqrt{s} = 27.5$ GeV, the comparison with the data points from [75] is reasonable. The data considered in this collection all refer to the $\gamma\gamma$ decay channel for the η, and have been collected by:

- Kourkoumelis et al. [45], who measured the η in p-p collisions at various center of mass energies. They provide four data points in the range $3 < p_T < 6$ GeV/c;
- the AMS Collaboration [7, 8, 9], which measured the η in p-p collisions at $\sqrt{s} = 63$ GeV. Their measurements provide 10 data points in the range $2 < p_T < 4$ GeV/c;
- the UA6 Collaboration [17], which measured the η both in p-p and p-$\bar{\text{p}}$ collisions at $\sqrt{s} = 24.3$ GeV. Four data points are provided in the range $2.5 < p_T < 3.5$ GeV/c;
- the Helios Collaboration, which studied the η meson in proton-nucleus collisions at $\sqrt{s} = 29.1$ GeV, providing six points for $p_T < 1.5$ GeV/c [75];
- the NA27 Collaboration, with 13 data points below 1.6 GeV/c measured in p-p collisions at $\sqrt{s} = 27.5$ GeV [76].

The entire collection of data points covers the p_T range from 0 to 6 GeV/c, and is shown in the left panel of Figure 6.8. On the data, a fit has been performed with the power-law function already used for describing the p_T spectra of the ω and ϕ mesons. As it can be seen, the function provides an excellent description of the data points, in the whole p_T range. The extracted parameters are:

$$p_0^2 = 1.7 \pm 0.3 \ \ (\mathrm{GeV}/c)^2 \qquad \beta = 6.3 \pm 0.5 \ .$$

As one can see, these values agree within their uncertainties with those estimated in the present analysis. The agreement is confirmed by the comparison between the MC p_T distribution, defined by the above parameters, and our data points for the $\eta \to \mu^+\mu^-\gamma$ decay, shown in the right panel of Figure 6.8 (where the error band of the MC reflects the errors on the p_0^2 and β parameters). The agreement between the data and the MC becomes satisfactory towards the hard-p_T limit of the broad error band.

We can conclude, then, that our measurement of the p_T for the η meson, as inferred from the p_T distribution of the Dalitz dimuon in the $\eta \to \mu^+\mu^-\gamma$ decay, is in agreement with the trend defined by the available experimental points. Since these latter provide a direct measure of the p_T distribution for the η meson, covering a range of p_T far beyond the limited one available for this analysis, we decided to assume the result of the fit shown in the left panel of Figure 6.8 as the input for the p_T distributions for the MC simulations.

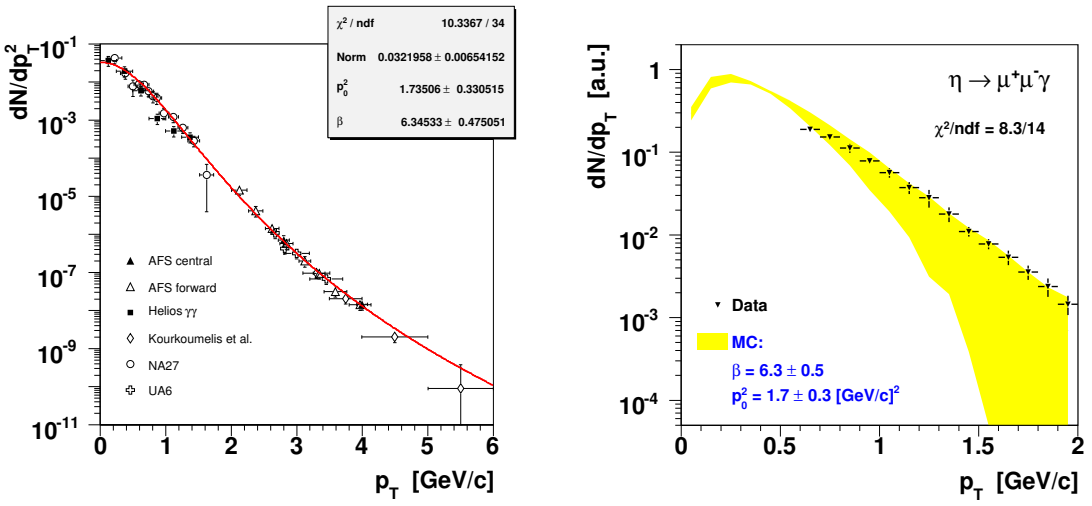

Figure 6.8: *In the left panel we show the fit on the available p_T measurements for the η. In the right panel, we compare the measured p_T distribution for the Dalitz dimuon in the $\eta \to \mu^+\mu^-\gamma$ decay with the MC prediction extracted from the previous fit.*

7

Relative Production Cross Sections for the Light Neutral Mesons

In this Chapter we present the results for the relative production cross sections of the η, ρ, ω and ϕ, as a function of the nuclear production target. This analysis allows one to characterize the nuclear dependence of the production cross sections for the light neutral mesons, as well as for their ratios. The study is first carried out integrating over p_T; then, in a second moment, the same analysis is performed in various p_T bins, so that the nuclear dependence of the production cross sections can be studied as a function of p_T.

7.1 Analysis Procedure

As already seen in the previous Chapter, where the p_T spectra of the η, ω and ϕ mesons have been studied, the first step of the analysis involves a fit on the raw mass spectrum, target by target. Integrating over p_T, we are left with six independent fits, respectively for the Be, Cu, In, W, Pb and U production targets.

The corresponding available statistics can be found in Table 5.1. It turns out that the number of events available for each target is large enough to allow the ρ contribution (via its 2-body decay $\rho \to \mu^+\mu^-$) to be independently normalized: in this way were able to study the nuclear dependence of the ratio $\sigma_\rho/\sigma_\omega$, thus investigating its possible dependence on the production target − which cannot be excluded *a priori*, although available experimental measurements largely support a $\sigma_\rho/\sigma_\omega = 1$ scenario.

The situation is different for the normalization of the $\eta \to \mu^+\mu^-$ and $\omega \to \mu^+\mu^-\pi^0$ contributions. These processes have been fixed to the major partner decays $\eta \to$

$\mu^+\mu^-\gamma$ and $\omega \to \mu^+\mu^-$, respectively, by a fit on the target-integrated spectrum, since these factors do not depend on the production targets.

The production cross section of the η' being fixed to the one of the ω, we are left with 5 free parameters, one more than in the analysis of the p_T spectra: these parameters basically accounts for the yields of the η, ρ, ω and ϕ mesons, and the normalization of the open charm contribution. As for the combinatorial background, its contribution is given in shape and normalization by the opposite-sign dimuon mass distributions obtained from the mixed event procedure described in Chapter 5.

7.1.1 Fits on the Raw Mass Spectra

The fits on the raw mass spectra, target by target, integrated over p_T, are shown in Figure 7.1. As one can see, the comparison between the MC cocktail profile and the data points is satisfactory over the whole mass range. In particular, the clear structures corresponding to the 2-body decays of the ω and ϕ mesons, as well as the Dalitz decay of the η, offer a good constraint for the estimation of the yield for the η, ω and ϕ mesons. The ρ 2-body decay, as already widely noted, does not dominate in any region of the spectrum: nevertheless, its contribution appears to be essential in order to achieve a good description of the regions at the sides of the ω peak.

The yields extracted from the fits on the raw mass spectra are corrected for the acceptance $\times$ efficiency factors, evaluated in the full phase space. In this way it is possible to get the corrected yields for the η, ρ, ω and ϕ mesons, defined in the full phase space, for each production target. These numbers are then properly corrected for the target-luminosity factors, compiled in Table 5.1: as seen in Chapter 5, these numbers account for the number of nuclei which a proton of the beam finds along its path, inside each target.

7.1.2 Evaluation of the Systematics

The final values for the relative production cross sections of the η, ρ, ω and ϕ mesons have been evaluated, together with their associated systematic uncertainties, following the same procedure described for the analysis of the p_T spectra. As explained in the previous Chapter, the evaluation of the systematics is performed by repeating the fits on the raw mass spectra, each time varying the input configuration, this latter being defined by the set of parameters which are kept fixed in the fit procedure.

The parameters defining the input configuration are chosen in the same way as for the analysis of the p_T spectra, apart from the ratio between the production cross sections of the ρ and ω mesons, which has been left free when the analysis is performed in full p_T. They are:

- cross section ratio $\sigma_{\eta'}/\sigma_\omega$;
- combinatorial background normalization;

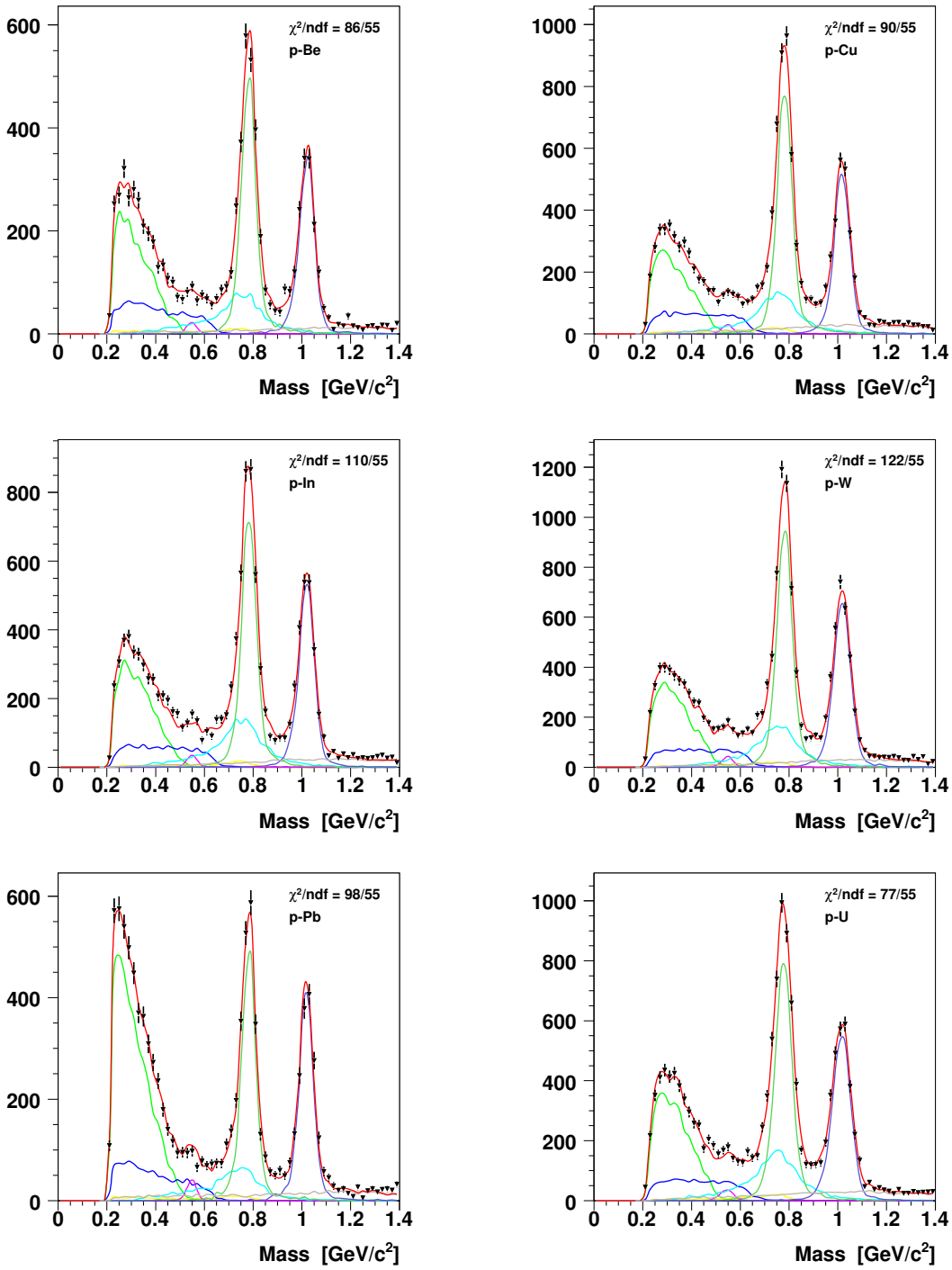

Figure 7.1: *Fits on the p_T-integrated raw pass spectra, for each production target.*

- normalization of the open charm contribution;
- relative branching ratios for the η and ω mesons;
- matching χ^2 for the single muons;
- generation settings for the MC.

A description of the role of each parameter involved in the input configuration can be found in the previous Chapter, within the discussion of the evaluation of the systematics for the analysis of the p_{T} spectra.

As in the case of the analysis of the p_{T} spectra, it should be noted that the parameters defining the input configuration have been varied one at a time. For each considered configurations, the yield as a function of the nuclear number A is extracted for the η, ρ, ω and ϕ mesons. In this case, the systematic uncertainties have been evaluated as the spread of the available systematic checks.

7.2 Particle Ratios

Following a common practice, ratios are defined with respect to the cross section of the ω meson. This choice is justified by the fact the the ω is the lightest neutral meson (apart π^0, which is not detectable in the $\mu\mu$ channel, and the ρ, whose contribution is much more difficult to constrain) being composed of "ordinary" quarks u and d, then providing a natural reference in collisions where the initial state only contains u and d valence quarks.

The ratio ϕ/ω has been indeed widely used as an indicator of enhanced strangeness production in nuclear collisions, due to the almost pure strange content of the ϕ meson. As it will be discussed in the last Section, enhancement of strange production has been observed in nuclear collision systems of increasing size. In order to establish a robust ground for these observations, the trend for strangeness production must be studied in proton-nucleus collisions also, as a function of the size A of the nucleus.

The same motivation justifies the interest in studying of the η/ω ratio as a function of A. The quark composition of the η meson also contains a strange component, although the η is not a pure $s\bar{s}$ as the ϕ meson. In this respect, any strangeness enhancement mechanism causing an increase of the ϕ/ω ratio should also cause an increase of the η/ω ratio.

On the contrary, no significant trend of the ρ/ω as a function of A is expected in p-A collisions. As it will be discussed in more details in the last Section, the available measurements indicate a ratio $\rho/\omega \simeq 1$ independent of A. Sharing the same quark composition, and having very similar masses, it seems reasonable to assume the ρ and ω production cross sections to be comparable − in absence of production mechanisms which could prefer one meson or the other.

The results on the observed particle ratios, described in the following, are summarized in Table 7.1.

7.2.1 ρ/ω and ϕ/ω Ratios

What we observe from our data confirms the expectations just mentioned above. The results for the ϕ/ω ratio clearly show that a rising trend as a function of A can be deduced for both the observables. The corresponding plot is shown in the right panel of Figure 7.2: the error bars account for statistical uncertainties; systematic uncertainties are also shown shadowed boxes. The mean values, averaged over the six available data points, are also shown as horizontal lines: a constant trend as a function of A is clearly ruled out for the ϕ/ω ratio, while a rising trend shines out from the plot.

Exactly the opposite conclusions can be drawn or the ρ/ω ratio, whose trend as a function of A is shown in the bottom panel of Figure 7.2: the red line again represents the mean value of the six points, one for each target material available. As it can be seen, not only the ρ/ω appears to be flat with A, but the value for the ratio comes out to be highly compatible with the hypothesis $\rho/\omega = 1$. Indeed, assuming the ratio to be independent of A, we can evaluate the $\rho/omega$ ratio from the fit on the target-integrated mass spectrum, obtaining the final estimation $\sigma_\rho/\sigma_\omega = 1.06 \pm 0.04$ (stat.) ± 0.07 (syst.).

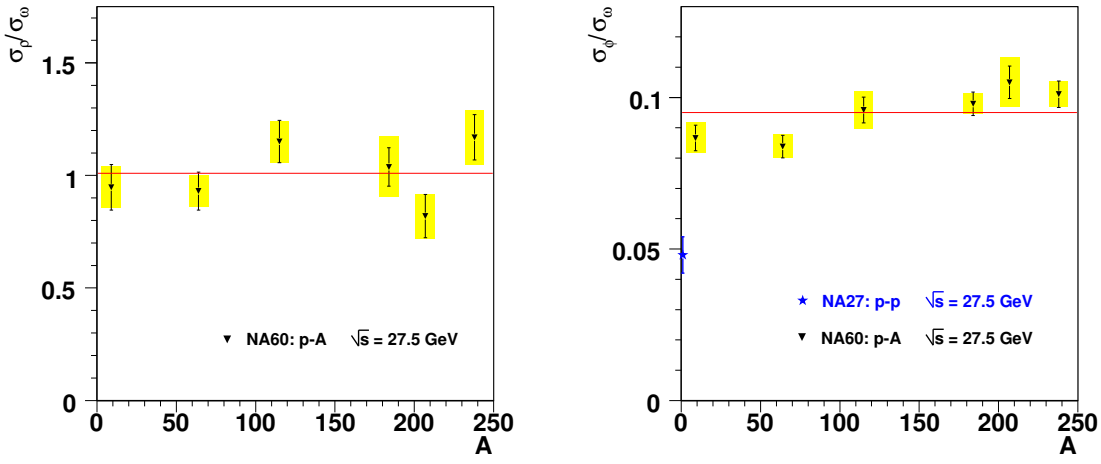

Figure 7.2: *Production cross section ratios $\sigma_\rho/\sigma_\omega$ and $\sigma_\phi/\sigma_\omega$ as a function of A. The ratios refers to the full phase space. Error bars and shadowed boxes account for statistical and systematic uncertainties, respectively.*

7.2.2 η/ω Ratio

The measurement of the η/ω ratio is affected by an additional uncertainty with respect to the measure of the ρ/ω and ϕ/ω ratios, due to the full phase space extrapolation of the acceptance $\times$ efficiency factor for the η meson. As it can be seen from the

left panel of Figure 6.8, in fact, we have only a limited p_T coverage for the $\eta \to \mu^+\mu^-\gamma$ process, from which we extract the yield for the η. The uncertainty resulting from the extrapolation to full-p_T directly propagates to the measurement of the η/ω ratio, and must be properly evaluated. On the contrary, it only marginally affects the measurement of the nuclear dependence of the η production cross section, considered in the next Section, since the extrapolation factor is common to all the targets and cancels out when normalizing to one of them.

A crude estimate for the uncertainty resulting from the full-p_T extrapolation can be obtained translating the error band on the MC p_T distribution in the left panel of Figure 6.8, to a corresponding uncertainty for the extrapolation factor from the measured range $0.6 < p_T < 2$ GeV/c to full-p_T. Performing such calculations, the error on the extrapolated full-p_T yield for the η (as measured from the $\eta \to \mu^+\mu^-\gamma$ decay) comes out to be $\sim 24\%$.

The resulting plot for the nuclear dependence of the η/ω ratio is shown in Figure 7.3, where the shadowed band accounts for the $\pm 24\%$ uncertainty, common to all the points, applied to the average value (represented by the horizontal line).

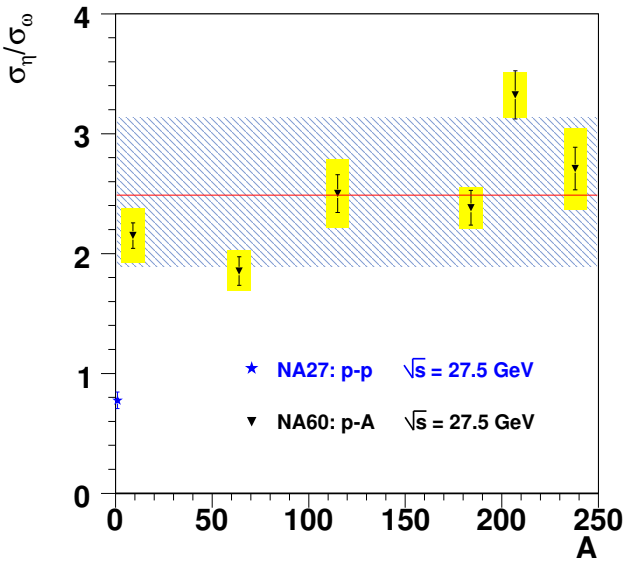

Figure 7.3: *Production cross section ratio $\sigma_\eta/\sigma_\omega$ as a function of A. The ratios refers to the full phase space. Error bars and shadowed boxes account for statistical and systematic uncertainties, respectively. The shadowed band accounts for the additional $\pm 24\%$ uncertainty, common to all the points, here applied to the average value, deriving from the error on the extrapolation of the yield for the η own to $p_T = 0$.*

Tgt	$\eta/\omega \pm 24\%$	ρ/ω	ϕ/ω
Be	$2.15 \pm 0.11 \pm 0.23$	$0.95 \pm 0.10 \pm 0.09$	$0.087 \pm 0.004 \pm 0.005$
Cu	$1.85 \pm 0.12 \pm 0.17$	$0.93 \pm 0.08 \pm 0.07$	$0.084 \pm 0.004 \pm 0.004$
In	$2.50 \pm 0.16 \pm 0.28$	$1.15 \pm 0.09 \pm 0.09$	$0.096 \pm 0.004 \pm 0.006$
W	$2.38 \pm 0.15 \pm 0.17$	$1.04 \pm 0.09 \pm 0.13$	$0.098 \pm 0.004 \pm 0.003$
Pb	$3.32 \pm 0.20 \pm 0.19$	$0.82 \pm 0.10 \pm 0.10$	$0.105 \pm 0.005 \pm 0.008$
U	$2.71 \pm 0.18 \pm 0.34$	$1.17 \pm 0.10 \pm 0.12$	$0.101 \pm 0.004 \pm 0.004$

Table 7.1: *Particle ratios for each production target. The additional ±24% systematic uncertainty on the η/ω ratio affects all the points in the same way.*

7.3 Nuclear Dependence of the Production Cross Sections

Besides allowing the study of the production cross section ratios for the considered mesons, the corrected yields could be exploited to evaluate the *absolute* production cross section for each particle, once the beam luminosity is known. Unfortunately, during the 2004 p-A run the three argonia counters, devoted to the measurement of the luminosity of the beam arriving the target system (see Chapter 2), were not properly calibrated. As a result, the estimation of the integrated beam luminosity for the runs considered in the present analysis is not available.

On the other hand, since the targets were simultaneously exposed to the beam during the data taking, they integrated the same luminosity − apart from the beam attenuation effects taken into account when evaluating the target-luminosity factors, see Chapter 5. This makes it possible to evaluate the *relative* production cross sections for the particles, i. e. their production cross sections for each available target, normalized to the lightest target available.

The relative production cross sections for the η, ω and ϕ mesons are shown in Figure 7.4, normalized to the Beryllium target. Having established a value $\sigma_\rho/\sigma_\omega$ compatible with 1, without any evidence of dependence on A, the cross section for the ρ is not shown in what follows. Parameterizing the nuclear dependence of the production cross sections with the power law

$$\sigma_{\mathrm{pA}} \propto \mathrm{A}^{\alpha} \,, \tag{7.1}$$

we are in the position to estimate the α parameter for the three mesons considered in the analysis. The fits are shown in Figure 7.4: the power law appears as a straight line in a double-logarithmic scale. The final values for the α parameters, together with their statistical and systematic uncertainties, are compiled in Table 7.2.

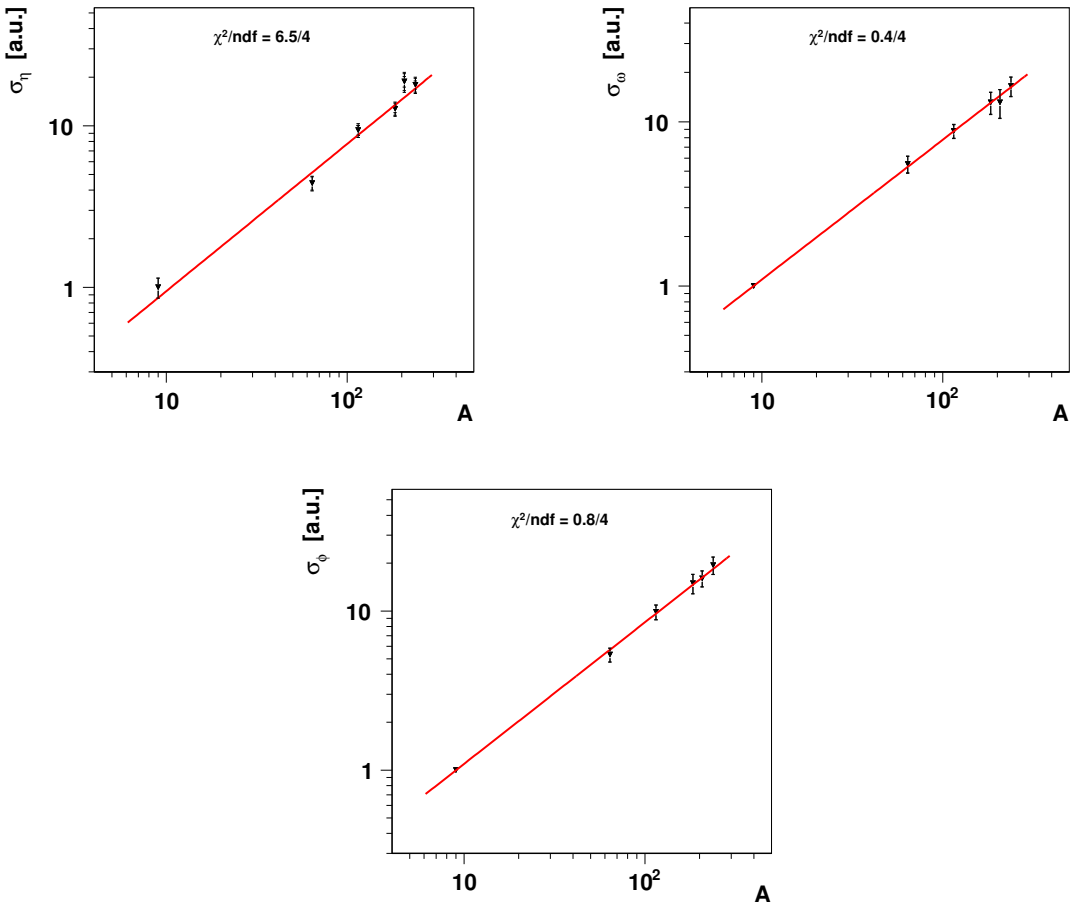

Figure 7.4: *Relative production cross section for the light mesons η, ω and ϕ, normalized to the Be target.*

7.3.1 Normalizing to the Cu Target

While it could appear reasonable to normalize the cross sections to the lightest target available in the data, the particular choice of the Be target is subject to a *caveat*, concerning the very nature of the Be nucleus. The Be nucleus, in fact, accounting for 9 nucleons only, is thought to be more similar to an incoherent superposition of single nucleons, rather than to a nuclear system having collective properties — as the heavier nuclei are.

As a consequence, if the nuclear identity exhibited by the Be nucleus is different from the one of the heavier nuclei, one may expect that the trend of the nuclear production cross sections as a function of A could deviate from the simple power law already for $A \leq 9$. In this case, normalizing the production cross sections to the Be target may bias the extracted α values: the next lighter target should then be taken into account for establishing the common normalization, and the Be point should be

excluded from the fit.

For this reason, we also considered the option to normalize the production cross sections to the Cu target, then leaving the Be target out from the fit range in which the power law A^{α} is compared to the data points. The resulting plots and fits are shown in 7.5: the result of the fit is extrapolated down to the Be point, in order to appreciate the mutual agreement with the previous results. The systematic uncertainties have been evaluated separately for the Be- and the Cu-normalization scenarios.

As one can see from Table 7.2, the effect of normalizing the production cross sections to the Cu target instead of the Be one (then excluding the Be target when evaluating the α parameters) goes in the direction to have α_{ϕ} and α_{η} closer to 1, and α_{ω} slightly closer to the "inelastic cross section" limit represented by $\alpha \simeq 0.72$. At the same time, removing the Be point has the remarkable effect to enlarge the statistical error for the α parameter extracted by the fit, because of the much reduced lever arm. In the last Section these results will also be discussed.

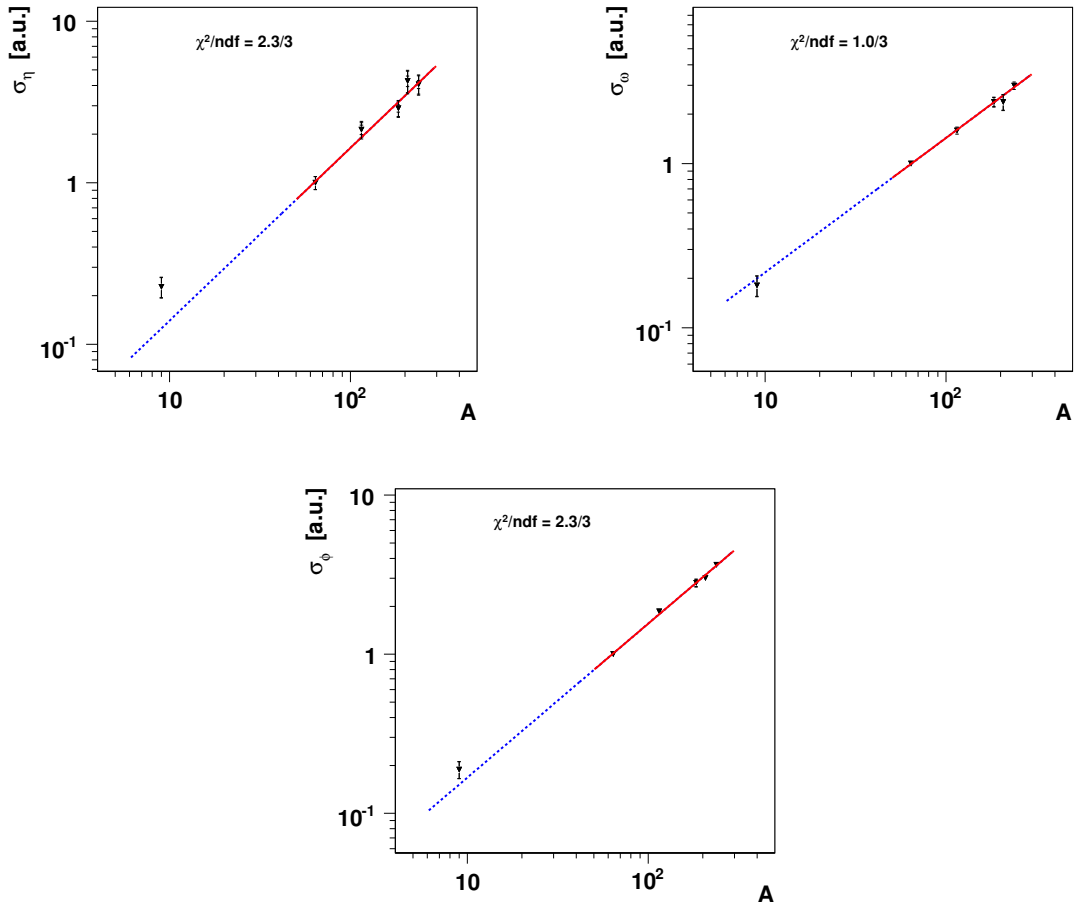

Figure 7.5: *Relative production cross section for the light mesons η, ω and ϕ, normalized to the Cu one.*

Removing the Pb Target

As already seen in the previous Chapter considering the p_T spectra of the ϕ and ω mesons, the particle yields extracted for the Pb target seem to be not properly evaluated, resulting there in p_T distributions qualitatively different from the ones observed in the other targets. For this reason, we also estimate the α parameter for the production cross sections removing the Pb point from the fit. The corresponding fit results, compiled in Table 7.2, show that removing the Pb target does not significantly affect the results for the α parameters, neither for the their values nor their errors. The reason for that is due to the position of the Pb point, falling between the W and the U ones, so that its displacement or exclusion do not dramatically alter the trend of the cross section as a function of A, which is still well constrained by the other two nearby targets.

	Normalized to Be	**Normalized to Cu**
with Pb	$\alpha_\eta = 0.935 \pm 0.048 \pm 0.060$	$\alpha_\eta = 1.036 \pm 0.078 \pm 0.067$
	$\alpha_\omega = 0.843 \pm 0.014 \pm 0.052$	$\alpha_\omega = 0.804 \pm 0.036 \pm 0.054$
	$\alpha_\phi = 0.904 \pm 0.011 \pm 0.043$	$\alpha_\phi = 0.962 \pm 0.026 \pm 0.031$
w/o Pb	$\alpha_\eta = 0.911 \pm 0.048 \pm 0.054$	$\alpha_\eta = 1.002 \pm 0.074 \pm 0.102$
	$\alpha_\omega = 0.853 \pm 0.014 \pm 0.051$	$\alpha_\omega = 0.834 \pm 0.038 \pm 0.052$
	$\alpha_\phi = 0.907 \pm 0.012 \pm 0.046$	$\alpha_\phi = 0.975 \pm 0.027 \pm 0.037$

Table 7.2: *Values of the α parameters describing the nuclear dependence for the η, ω and ϕ cross sections, integrated over the whole accessible p_T range.*

7.3.2 p_T Dependence of the α Parameters

As a final item for the analysis of the production cross sections, we present here a preliminary study of the p_T dependence of the α parameters for the ω and ϕ mesons. In this study we repeated exactly the same procedure which has been described in the previous Sections, this time splitting the data into p_T bins of 200 MeV/c, starting from $p_T = 0$ MeV/c.

For each slice of p_T, a final value for the α_ω and α_ϕ parameters has been obtained, together with their statistical and systematic uncertainties. In this way, a trend as a function of p_T can be established. As already seen for the p_T-integrated analysis, no significant variation of the results is observed when the Pb point is excluded from the analysis; we then decided to retain it for the analysis of the α parameters as a function of p_T. On the contrary, since the choice of the normalization target has shown to be

the source of non-negligible systematic variations of the values and the uncertainties for the α parameters, we still consider the two options − i. e. normalizing to the Be or the Cu target − in this last piece of the analysis.

The plots showing the p_T dependence of the α parameters are reported in Figure 7.6: in the left column the normalization on the Be target is considered, while in the right column the same plots are shown taking into account the normalization on the Cu target. For each plot, error bars and shadowed boxed account for the statistical and systematic uncertainties, respectively.

As it can be immediately noticed, the choice of the normalization target (Be or Cu) heavily influences the magnitude of the statistical uncertainties. On the other hand, one can probably conclude that for each particle the two plots corresponding to the different choices of the normalization target are compatible with each other, at least within the rather large total uncertainties. In any case, these plots clearly claim for an evidence of a rising trend of the α parameters as a function of p_T. This observation is in agreement with previous measurements available from other experiments, as it will be discussed in the last Section.

7.4 Discussion of the Results

In this Section we discuss the results obtained for the particle ratios and the nuclear dependence of the production cross sections. Concerning the particle ratios, only the NA27 measurements in p-p at $\sqrt{s} = 27.5$ GeV [76] can be compared to ours. Concerning the nuclear dependence of the production cross sections in proton-nucleus collisions, on the other hand, only the ϕ meson profits from a variety of published measurements, while no reference is currently available for the ω and η mesons.

7.4.1 Particle Ratios

The NA27 experiment measured the η, ρ, ω and ϕ production cross sections in p-p collisions at 400 GeV [76], from which we can extract the only available values of the $\sigma_\eta/\sigma_\omega$, $\sigma_\rho/\sigma_\omega$ and $\sigma_\phi/\sigma_\omega$ ratios directly comparable to our results. The measurements were done in the forward hemisphere. After extrapolation of the measured values to full phase space, they obtained the following values: $\sigma_\eta/\sigma_\omega = 0.77 \pm 0.07$, $\sigma_\rho/\sigma_\omega = 0.98 \pm 0.08$, $\sigma_\phi/\sigma_\omega = 0.048 \pm 0.006$.

The NA27 $\sigma_\rho/\sigma_\omega$ value is in perfect agreement with the one presented in this analysis, and both are compatible with the hypothesis $\sigma_\rho/\sigma_\omega = 1$ independently on the system size.

Concerning the $\sigma_\phi/\sigma_\omega$ ratio, the NA27 measurement is shown together with the NA60 points in the left panel of Figure 7.2. The comparison shows that a strangeness enhancement is observed going from p-p to p-A collisions, further enhancing as a function of A.

The comparison between the NA27 and NA60 points for the η/ω leads to similar conclusions as for the ϕ/ω ratio, as shown in Figure 7.3. Given the strange component in the quark composition of the η, strangeness enhancement from p-p to p-A collisions can also explain the observed difference between the η/ω ratio measured by NA27 and NA60.

The HELIOS-I experiment has measured the $\eta/(\rho+\omega)$ ratio in p-Be collisions at $\sqrt{s} = 29.1$ GeV [10], through the detection of both dielectrons and dimuons, including the capability to fully reconstruct the Dalitz decays. HELIOS-I used a $(1+\cos^2\theta)$ decay angle distribution to extrapolate their ρ and ω measurements to full phase space, obtaining $\sigma_\eta/(\sigma_\rho+\sigma_\omega) = 0.54 \pm 0.05$ from the e^+e^- data and 0.52 ± 0.06 from the $\mu^+\mu^-$ data. If Helios-I had assumed that the ρ and ω mesons ave a uniform dimuon decay angle distribution, as we did in this analysis, their full phase space ρ and ω cross sections would be around 20% lower, resulting in a $\sigma_\eta/(\sigma_\rho+\sigma_\omega)$

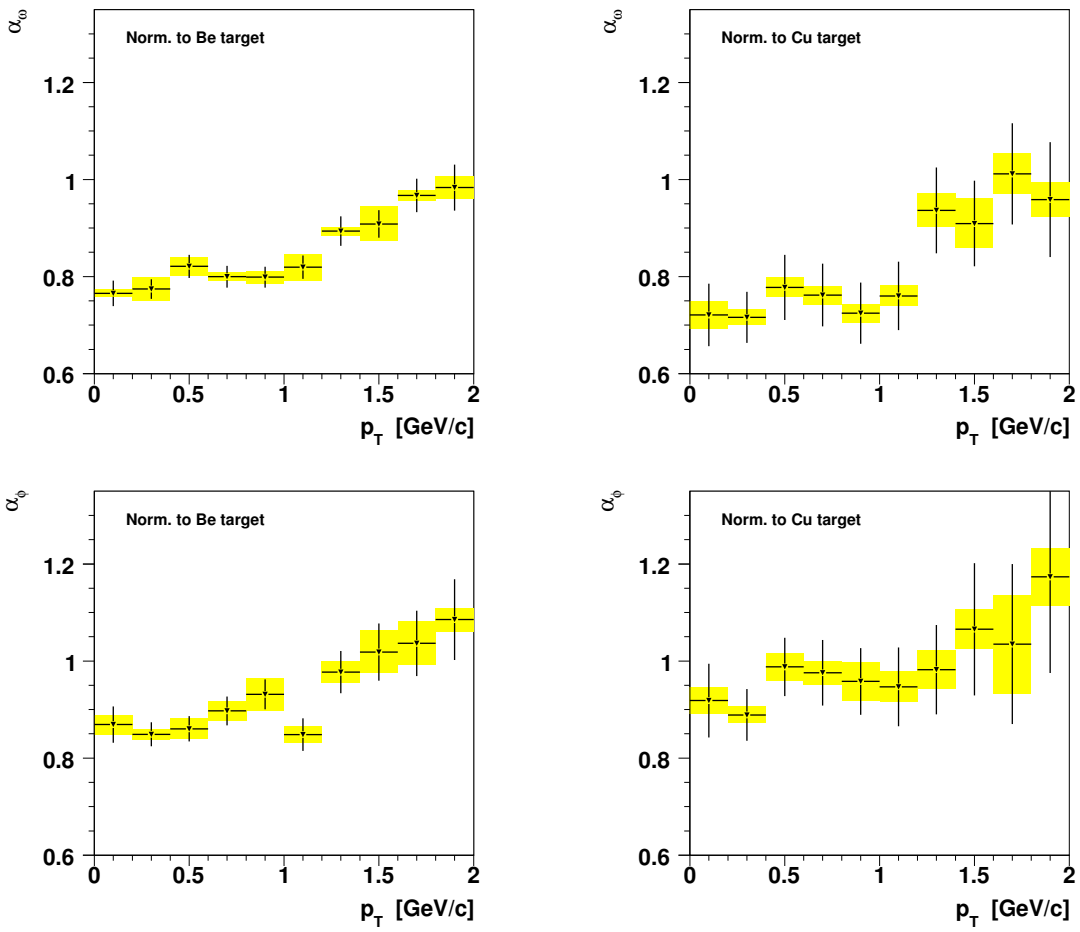

Figure 7.6: *p_T dependence of the α parameter for the ω and ϕ mesons.*

ratio around 0.64 ± 0.06 if one neglects the ρ/ω interference effect which was studied by HELIOS-I. From our p-Be measurement we derive a $\sigma_\eta/(\sigma_\rho + \sigma_\omega)$ ratio of 1.07 $\pm$ 0.11 (stat.) $\pm$ 0.21 (syst.); taking into account the additional $\pm$24% uncertainty coming from the extrapolation of the measurement down to $p_T = 0$, we can conclude that our measurement is still compatible within the resulting uncertainty with the $\sigma_\eta/(\sigma_\rho + \sigma_\omega) = 0.64 \pm 0.06$ Helios-I value.

7.4.2 Nuclear Dependence of the Production Cross Sections

Concerning the nuclear dependence of the production cross sections for the light neutral mesons, several values from previous experiments are available for the ϕ meson, although at energy regimes often significantly different from the ones considered in the present analysis.

The α parameter for the ϕ meson has been measured by the NA11 Collaboration, at the CERN-SPS, studying collisions of 120 GeV protons on beryllium and tantalum targets, using $\phi \rightarrow K^+K^-$ decays [23]. They obtained a value $\alpha_\phi = 0.86 \pm 0.02$ (with a systematic uncertainty estimated to be around three times smaller than the statistical one) for ϕ mesons produced in the phase space window $0 < x_F < 0.3$ and $p_T < 1$ GeV/c.

The BIS-2 Collaboration, at Serpukhov, measured the α value of the ϕ mesons produced in collisions induced by neutrons, of energies betweem 30 and 70 GeV, colliding with carbon, aluminum and copper targets, studying the $\phi \rightarrow K^+K^-$ decays [13]. They obtained $\alpha_\phi = 0.81 \pm 0.06$, for ϕ mesons produced with $x_F > 0$ and $p_T < 1$ GeV/c. (without mentioning systematic errors).

More recently, the HERA-B experiment at DESY studied the ϕ meson in p-C, p-Ti and p-W collisions at $\sqrt{s} = 41.6$ GeV [3], as we already mentioned in the previous Chapter discussing the results for the transverse momentum spectra. HERA-B found a value $\alpha_\phi = 0.96 \pm 0.02$, in the phase space covered by the detector, $-0.7 < y_{cms} < 0.25$ and $0.3 < p_T^2 < 12$ (GeV/c)^2. Extrapolating the measurements to zero p_T, the value for α_ϕ decreases to $\alpha_\phi = 0.91 \pm 0.02$ (where the error includes the systematic uncertainty). The analysis also clearly showed a that the value of α increases with p_T, reaching 1.1 at $p_T^2 \sim 10$ (GeV/c)^2, in agreement with the behavior observed by Cronin *et al.* for charged kaons [42]. The comparison between the trend of α_ϕ vs p_T, as observed by NA60 (present analysis, normalizing to Be) and HERA-B, shows a remarkable agreement in the common range of p_T, both qualitatively and quantitatively, see Figure 7.7.

The KEK-PS E325 experiment [71] also measured the α parameter for the ϕ meson, studying its e^+e^- decay in p-C and p-Cu collisions at $\sqrt{s} = 5.1$ GeV. In the region of $0.9 < y < 1.7$ and $p_T < 0.75$ GeV/c they found $\alpha_\phi = 0.937 \pm 0.049 \pm 0.018$. This same analysis also provides a measurement for the α parameter of the ω mesons: $alpha_\omega = 0.710 \pm 0.021 \pm 0.037$, compatible with the value of α for the total inelastic p-A cross section and significantly lower than our result.

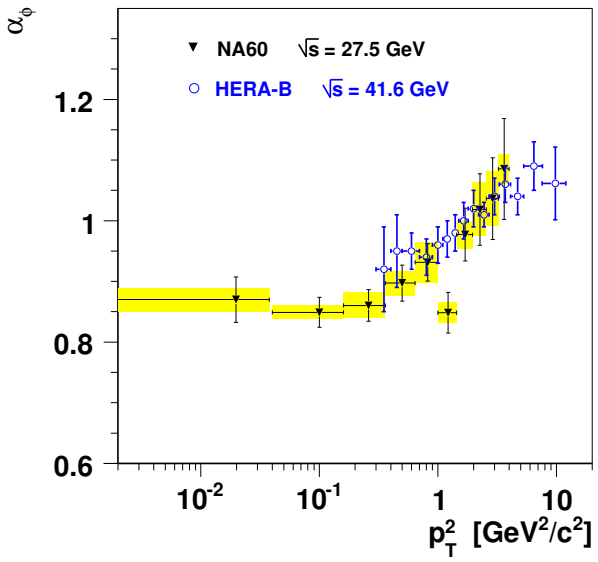

Figure 7.7: *Comparison between the trend of α_ϕ as a function of p_T as observed by NA60 (present analysis, normalizing to the Be target) and HERA-B [3].*

As a general remark on the the available values for the α parameter of the ϕ meson, compiled in Table 7.3, we must notice that a comparison between the different quoted values to one another is rather difficult, due to various factors:

- the difference in the kinematical region covered by the experiment: this is particularly relevant for the p_T coverage, since a non negligible rising trend of α with p_T has been explicitly observed both within the present analysis and the analysis of the HERA-B data;

Experiment	Beam	Targets	α_ϕ
KEK-PS E325	p, 12 GeV	C, Cu	$0.937 \pm 0.049 \pm 0.018$
BIS-2	n, 30–70 GeV	C, Al, Cu	0.81 ± 0.06
NA11	p, 120 GeV	Be, Ta	0.86 ± 0.02
NA60	p, 400 GeV	Be, Cu, In, W, Pb, U	$0.904 \pm 0.011 \pm 0.043$
NA60	p, 400 GeV	Cu, In, W, Pb, U	$0.962 \pm 0.026 \pm 0.031$
HERA-B	p, 920 GeV	C, Ti, W	0.91 ± 0.02

Table 7.3: *α parameter for the ϕ meson measured in the present analysis, compared to the values previously published by other experiments.*

- the difference in the collisional systems and energies considered: the energy available for the collisions determines the average p_{T} for the produced particles, which in turn influences the observed value of the α parameter;
- all the experiments considered here extract the α parameter considering two or at most three different targets: this results in a poor reliability of the measurement, especially when one of the targets is relatively light as carbon or beryllium.

Differently from the case of the ϕ, we finally note how a general lack of published measurements for the η and ω mesons in p-A collisions does not allow any comparison with their α values found within the present analysis. The only available value for the ω meson, by the KEK-PS E325 Collaboration, has been obtained at such different energies from the present analysis, that any comparison is probably not relevant at all.

8

Electromagnetic Transition Form Factors for the η and ω Mesons

The last item of the analysis presented in this thesis concerns the measurement of the electromagnetic transition form factors of the η and ω mesons. As already noticed in Chapter 1, the interest on this measurement goes beyond the traditional realm of the nuclear experimental physics. This demonstrates how a high precision experiment like NA60, although designed to cover specific items in the field of nuclear physics, could still give significant contributions on experimental cases more related to particle physics – as for the electromagnetic transition form factors of the η and ω mesons.

This analysis, exploiting the high-statistics event sample collected by NA60 in proton-nucleus collisions, complements and improves the results of the precursory study performed on the peripheral Indium-Indium events within the same NA60 experiment, recently published in [22]. Remarkably enough, we note here that the results for the electromagnetic transition form factors of the η and ω mesons, obtained in the analysis of the peripheral In-In data, were the first results ever, from a heavy-ion experiment, entering the Review of Particle Properties published by the Particle Data Group [55].

8.1 Analysis Procedure

As already seen studying the transverse momentum spectra and the nuclear dependence of the production cross sections, the present analysis also starts by considering the raw mass spectrum. With respect to the analyses presented in the previous Chapters, however, here we exploit the full available statistics resulting by integrating over the production targets and the full phase space. The reason for that is very simple indeed: we are now measuring particles properties – the electromagnetic transition

form factors − which for their very nature do not depend on the production from a given nuclear target.

The description of the raw mass spectrum in terms of the cocktail of MC process, now allows us to isolate the processes of interest for the measurement of the electromagnetic form factors, by subtracting the other processes using the same normalizations fixed by the fit on the mass spectrum. The resulting mass spectrum, corrected for the acceptance × efficiency profile as a function of the mass, will finally be compared with the superposition of the theoretical line shapes for the retained processes, from which the form factors will be evaluated.

8.1.1 The Fit on the Raw Mass Spectrum

The full, target-integrated event sample has already been shown in Chapter 5. As it was mentioned there, integration over the targets can be performed both *with* or *without* the selection imposed by the target identification for the dimuons. In principle, when we are not interested in considering the production target, there is no reason to still filter the dimuon sample with the target identification criterion. On the other hand, the selection imposed by the dimuon-target association criterion may be regarded to as a sort of "quality selection" for the dimuons, defining a special sample of events which could be used to validate the results given by the full sample. For this reason, the same analysis has been carried out both including and excluding the target identification for the dimuons.

The fits on the raw mass spectrum are reported in Figure 8.1, from which we can conclude that the superposition of the MC processes satisfactorily describes the profile of the observed mass spectrum. All the details visible in the mass spectrum are reproduced by the MC cocktail, from the resolution of the prominent ω and ϕ peaks to the continuum shape of the η Dalitz decay, to the small peak due to the 2-body decay of the η. The shape of the ρ contribution accounts for the asymmetry of the sides of the ω peak, and the normalization of the continuum contribution of the open charm process is essentially normalized by the mass region above the ϕ peak.

8.1.2 Isolating the Processes of Interest

The parameters optimized by the fit procedure fix the level of each process contributing to the low mass spectrum. In this way we are in the position to subtract, from the real mass spectrum, those processes which are not of interest for the measure of the form factors of the η and ω mesons − using exactly the normalizations fixed from the fit to the real data. This procedure has been adapted from the analogous analysis of the form factors performed on the NA60 peripheral In-In data, explained in [22].

We subtract from the raw mass spectrum all the MC processes with the exception of the Dalitz decays of η and ω, and the two-body decay of the ρ. It should be noticed here that the ω and ϕ peaks stand, in any case, completely outside of the

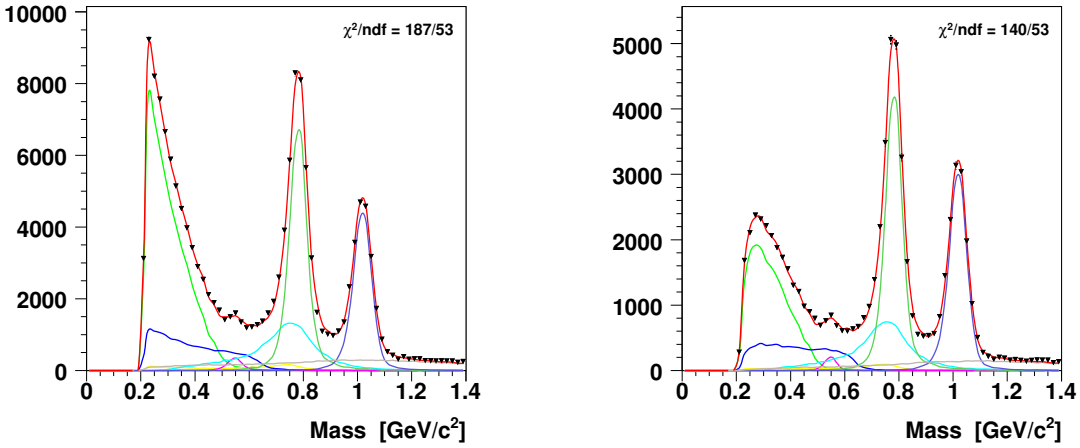

Figure 8.1: *Target-integrated raw pass spectra excluding (left panel) and including (right panel) the identification of the production target for the dimuons. The superposition of the MC processes describes the observed data points.*

mass window relevant for the study of the η and ω Dalitz decays, i.e. the window $0.2 < M < 0.65$ GeV/c^2. The sole reason for their subtraction is the isolation of the broad vector meson ρ, which is normally masked by the much narrower ω at nearly the same mass, making it then much easier to control the systematics due to a small contribution from the low-mass tail of the ρ itself in the mass region of interest here. Within the mass region of interest, the well resolved $\eta \to \mu^+\mu^-$ channel is also subtracted, using again the normalization fixed by the fit. The remaining sources, the η' Dalitz decay and the open charm, being only on a level of a few percents each of the total yield, are finally taken out.

The remaining samples after all subtractions are reported in Table 8.1, together with the corresponding statistics exploited in the analysis of the NA60 peripheral In-In data [22] and the analysis of the Lepton-G data [35, 34, 47].

The mass spectrum resulting after the subtraction of the non-interesting processes is shown in Figure 8.2, both excluding and including the identification of the production target for the dimuons. The mass spectrum is still dominated by the prominent structure of the η Dalitz decay − although significantly suppressed when the target identification is required − and the broad peak of the ρ meson can now also be easily identified.

8.1.3 Acceptance × Efficiency Correction

The mass spectrum resulting after the subtraction procedure, now only accounting for the $\eta \to \mu^+\mu^-\gamma$, $\omega \to \mu^+\mu^-\pi^0$ and $\rho \to \mu^+\mu^-$ contributions, is then corrected for the

Experiment	$\eta \to \mu^+\mu^-\gamma$	$\omega \to \mu^+\mu^-\pi^0$
NA60 p-A (tgt identification OFF)	53 000	15 000
NA60 p-A (tgt identification ON)	17 000	7 000
NA60 In-In periph.	9 000	3 000
Lepton-G	600	60

Table 8.1: *Comparison between the available statistics for the present analysis, the analysis of the NA60 peripheral In-In data [22] and the analysis of the Lepton-G data [35, 34, 47].*

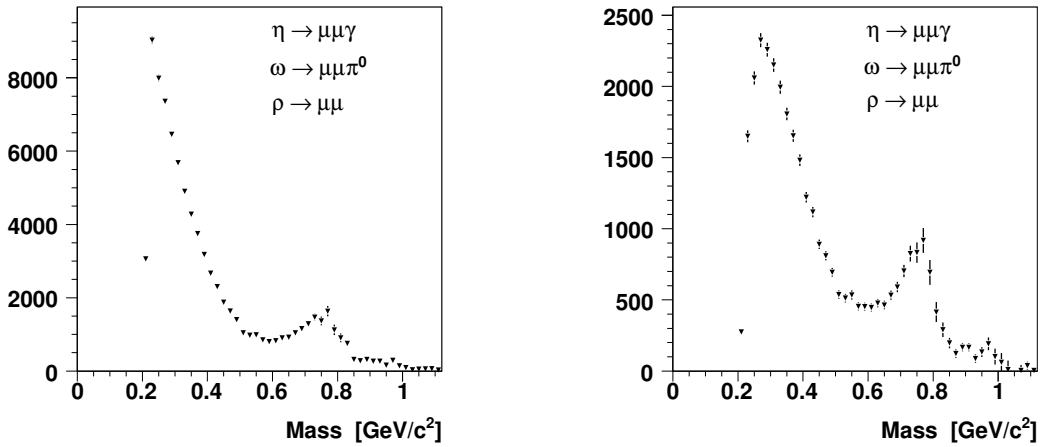

Figure 8.2: *Mass spectra resulting after isolating the processes of interest for the measure of the electromagnetic form factors. As usual, the two panels account for excluding (left panel) and including (right panel) the identification of the production target for the dimuons.*

effects of geometrical acceptance and reconstruction efficiency. In order to do so, we build a correction profile as a function of the mass, weighting the profiles we get from the MC for the three processes separately. We must keep in mind, in fact, that the three processes may have different acceptances even in the same mass region, due to the differences associated to the remaining kinematic degrees of freedom; from this, the necessity to properly weight their contributions in each bin of mass.

The acceptance $\times$ efficiency profile for each process is built dividing the reconstructed MC mass spectrum by the corresponding generated spectrum; the absolute

normalization of these two spectra is also important here: the normalization of the reconstructed spectrum is given directly by the fit on the mass spectrum, while the generated profile is correspondingly normalized taking into account the mass-integrated acceptance × efficiency factor.

For each process, the content of the i-th bin of the generated mass spectrum is proportional to the probability that a dimuon falling within that bin has been produced by the given process. It follows that the weighted acceptance for the three processes must be built, bin per bin, weighting the content of the acceptance × efficiency profile for each process by the content of their generated mass profile, properly normalized as described above. This procedure is self-consistent, since the weights used to weight the three single-process acceptances are determined from the data themselves.

Nevertheless, in order to further test the stability of our results on the form factors parameters, the weights for the three processes have also been varied. Since in the mass region involved in the determination of the form factors (below 0.65 GeV/c^2) the $\rho \to \mu^+\mu^-$ is hardly significant, we will only change the relative weights of the two Dalitz processes. This has been done by changing one of the two weights, keeping the other fixed. In this way, we defined three acceptance options:

(A) no variation of the weights;

(B) weight for $\omega \to \mu^+\mu^-\pi^0$ scaled by a factor 0.5;

(C) weight for $\omega \to \mu^+\mu^-\pi^0$ scaled by a factor 1.5.

The broad range defined by this choice should account for the rather large uncertainty which must affect the ratio between the p_T-integrated acceptances of the Dalitz decays of the η and ω mesons, due to their remarkably small acceptance × efficiency in the low-p_T region, where the main fraction of the Dalitz dimuons are produced. The resulting acceptance × efficiency profiles for the superposition of the $\eta \to \mu^+\mu^-\gamma$, $\omega \to \mu^+\mu^-\pi^0$ and $\rho \to \mu^+\mu^-$ processes, is shown in Figure 8.3 (without requiring target identification for the dimuons) and Figure 8.4 (requiring target identification) for the three weighting options just defined. The ratios of the "alternative" options B and C with respect to the "reference" option A are also shown. As one can see, whichever the considered option, the weighted profile is dominated by the η Dalitz acceptance for masses below 0.5 GeV/c^2, while the $\rho \to \mu^+\mu^-$ process dominates above 0.6 GeV/c^2.

Fit on the Acceptance-Corrected Mass Spectrum

After the correction for the acceptance × efficiency effects, the resulting mass spectrum is finally compared with the superposition of the expected line shapes of the three processes $\eta \to \mu^+\mu^-\gamma$, $\omega \to \mu^+\mu^-\pi^0$ and $\rho \to \mu^+\mu^-$. These line shapes are described by the following functions:

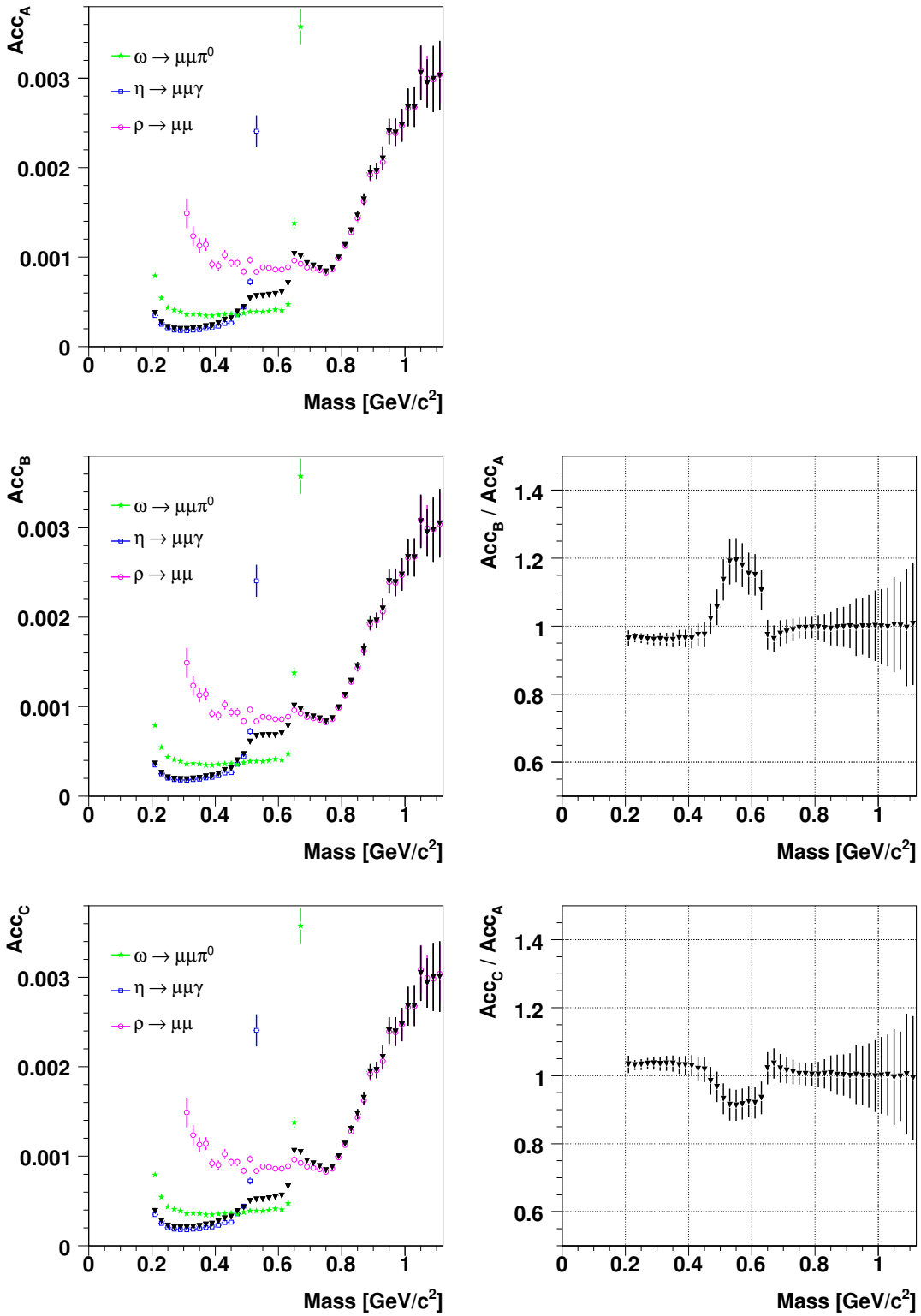

Figure 8.3: *Weighted acceptances and their ratios, when target identification is not required.*

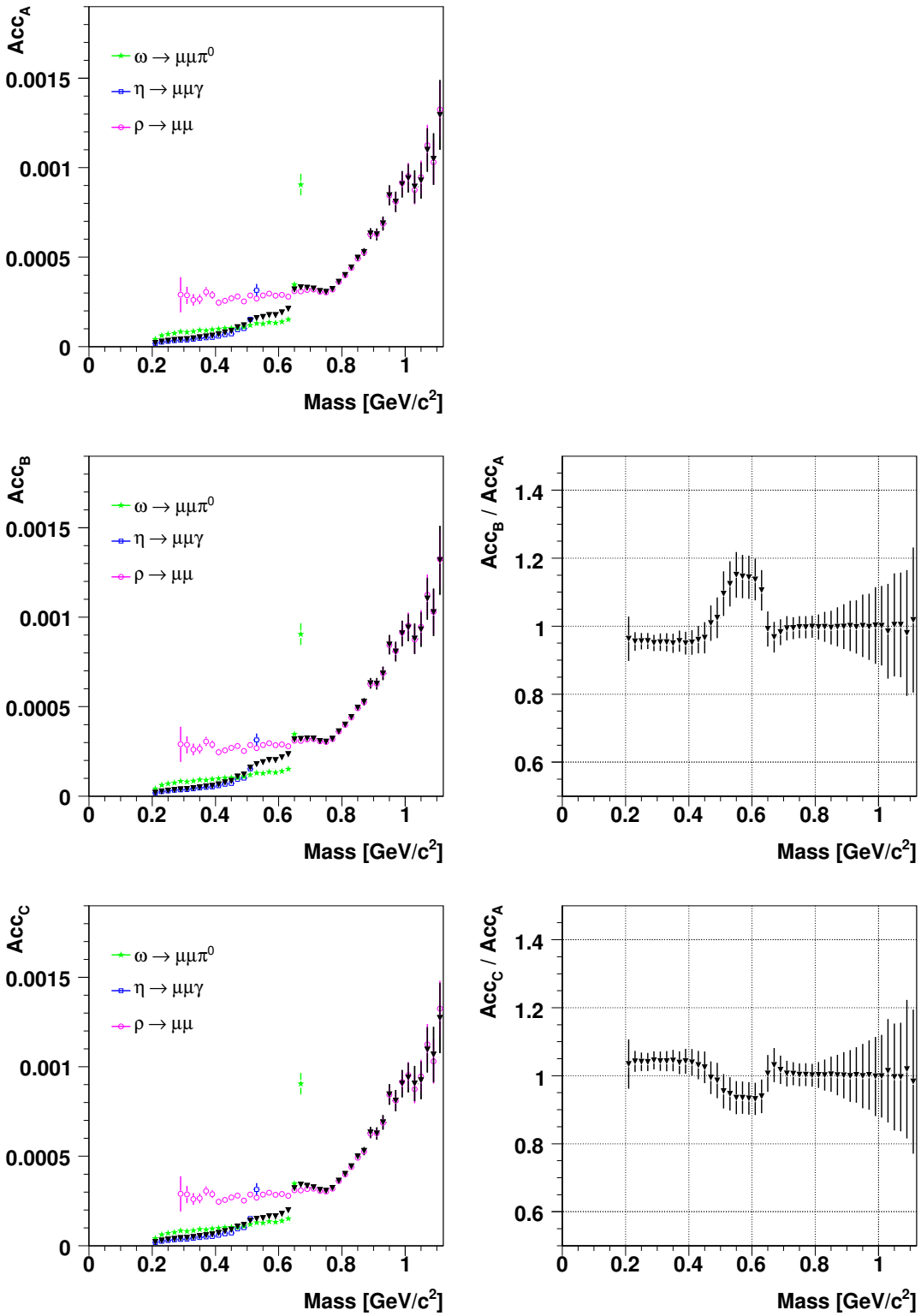

Figure 8.4: *Weighted acceptances and their ratios, when target identification is required.*

$$\left.\frac{dN}{dM}\right|_{\eta_{Dal}} \propto 2M \times \frac{d\Gamma(\eta \to \mu^+\mu^-\gamma)}{dM^2} = \\ = 2M \times \frac{2}{3}\frac{\alpha}{\pi}\frac{\Gamma(\eta \to \gamma\gamma)}{M^2} \times \left(1 - \frac{M^2}{m_\eta^2}\right)^3 \left(1 + \frac{2m_\eta^2}{M^2}\right)\left(1 - \frac{4m_\eta^2}{M^2}\right)^{1/2} \times \left|F_\eta(M^2)\right|^2 \quad (8.1)$$

$$\left.\frac{dN}{dM}\right|_{\omega_{Dal}} \propto 2M \times \frac{d\Gamma(\omega \to \mu^+\mu^-\pi^0)}{dM^2} = 2M \times \frac{\alpha}{3\pi}\frac{\Gamma(\omega \to \gamma\pi^0)}{M^2} \times \left(1 + \frac{2m_\mu^2}{M^2}\right) \times \\ \times \left(1 - \frac{4m_\eta^2}{M^2}\right)^{1/2} \times \left[\left(1 + \frac{M^2}{m_\omega^2 - m_{\pi^0}^2}\right)^2 - \frac{4m_\omega^2 M^2}{(m_\omega^2 - m_{\pi^0}^2)^2}\right] \times \left|F_\omega(M^2)\right|^2 \quad (8.2)$$

$$\left.\frac{dN}{dM}\right|_{\rho} \propto \frac{d\Gamma(\rho \to \mu^+\mu^-)}{dM} = \frac{\alpha^2 m_\rho^4}{3(2\pi)^4} \times \\ \times \left(1 - \frac{4m_\mu^2}{M^2}\right)^{1/2}\left(1 + \frac{2m_\mu^2}{M^2}\right) \times (2\pi M T)^{3/2} \times \frac{1}{(M^2 - m_\rho^2)^2 + (M\Gamma_{tot}^0)^2} \quad (8.3)$$

The line shapes for the Dalitz decays correspond to the theoretical line shapes derived in the framework of the QED − thus considering point-like particles in the Feynman diagrams depicted in Figure 1.11 − multiplied by the mass-dependent form factors $\left|F_\eta(M)\right|^2$ and $\left|F_\omega(M)\right|^2$, respectively, being described by the pole parametrization

$$F(M) = \left[1 - \frac{M^2}{\Lambda^2}\right]^{-1} \quad (8.4)$$

introduced in Chapter 1 in the framework of the Vector Meson Dominance (VMD) model. The line shape adopted for the $\rho \to \mu^+\mu^-$ is the one already described in Chapter 4. It should be noted that considering the additional factor $\left(1 - \frac{4m_\pi^2}{M^2}\right)^{3/2}$ in the ρ line shape does not introduce any significant effect on the pole parameters for the η and ω mesons; in any case, the fit seems to slightly prefer a ρ line shape without this factor. In the fit, the following parameters have been left free:

- the three normalizations, one for each of the line shapes above;
- the parameters Λ_η^{-2} and Λ_ω^{-2}, contained respectively in the form factor $\left|F_\eta(M)\right|^2$ and $\left|F_\omega(M)\right|^2$, according to the parametrization 8.4.

Concerning the line shape for the $\rho \rightarrow \mu^+\mu^-$ decay, the parameters Γ_ρ (entering in the definition of Γ_{tot}) and m_ρ are fixed to their PDG values, while the effective temperature T_ρ has been set to 170 MeV consistently both with what observed in the NA60 peripheral In-In data and what expected by statistical model fits on particle ratios in p-p interactions. Three different fit options have furthermore been defined, contributing to the estimation of the systematic uncertainties on the output parameters:

(α) The five parameters are all left free, and the fit is performed from the threshold up to 0.9 GeV/c^2;

(β) After having performed a fit with the option α, the normalization and the pole parameter of the $\omega \rightarrow \mu^+\mu^-\pi^0$ line shape are fixed and the fit is performed again, this time from the threshold up to 0.9 GeV/c^2;

(γ) After having performed a fit with the option α, the normalization and the pole parameter of the $\eta \rightarrow \mu^+\mu^-\gamma$ line shape are fixed and the fit is performed again, this time from 0.5 GeV/c^2 up to 0.9 GeV/c^2.

In Figure 8.5 the fit on the corrected mass spectrum is shown, considering as usual the two options of excluding and including the target identification for the dimuons. In both the cases, the spectrum has been corrected with the "reference" acceptance A, and the fit performed using the fit option α.

The best description of the mass spectrum resulting after the correction is probably given by the following citation, adapted from [22]. "The spectral shape of the data looks impressive. Beyond the η Dalitz decay which was easily recognizable before in Figure 8.1 due to its dominance in the mass region $M < 0.5$ GeV/c^2 and its characteristic mass shape, the ρ now shines out completely isolated, and the ω Dalitz decay in between becomes directly recognizable in the mass window $0.5 < M < 0.65$ GeV/c^2 through the characteristic shoulder close to the kinematic cut-off of its mass distribution. This shoulder reflects, beyond any doubt, the qualitative existence of the strong anomaly in the associated electromagnetic transition form factor [35, 47] and the data quality in this well-isolated section raises the expectation that the extraction of the quantitative details will be possible with a high reliability. This is indeed the case."

We may add that the statistics available in the NA60 p-A sample is even higher than the one which could be exploited in the analysis of the peripheral In-In events. This reflects, as we will see, in improved statistical uncertainties for the measurement of the electromagnetic transition form factors.

8.2 Systematics and Results

As for the analysis of the transverse momentum spectra and the cross sections, several systematic checks have been defined here to test the stability of the results, and estimate their systematic uncertainties. These checks can be summarized as follows:

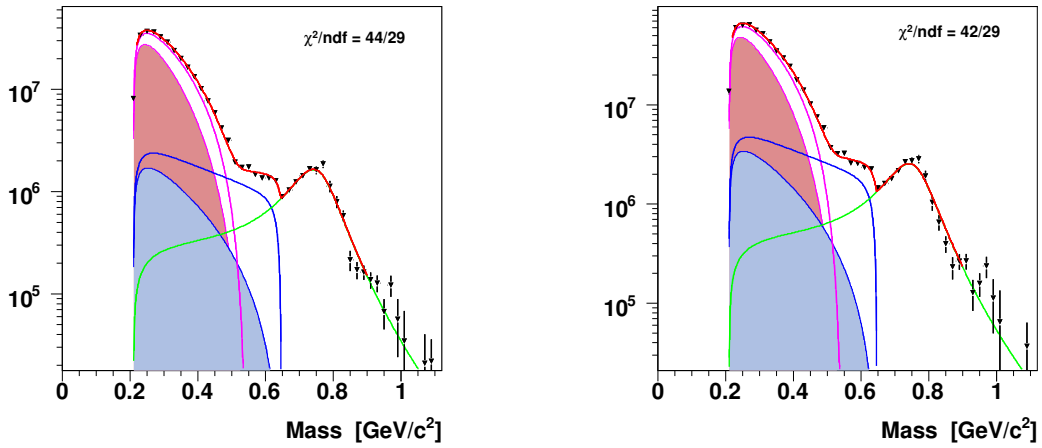

Figure 8.5: *Fit on the corrected mass spectrum, both excluding (left panel) and including (right panel) the identification of the production target for the dimuons. The shaded areas indicate the Kroll-Wada expectations for point-like particles, defined by QED [46]*

- choice of three different weighted acceptances "A", "B" and "C" (see above for the definitions);
- choice of three different options for the fit of the acceptance-corrected mass spectrum (see above for the definitions);
- the extreme scenarios $\sigma_{\eta'}/\sigma_{\omega} = 0.0$ and 4.8, accounting to 0% and 400% of the reference value $\sigma_{\eta'}/\sigma_{\omega} = 0.12$;
- scaling the level of the combinatorial background by a factor 66% up to 166% of the reference level fixed by the comparison with the LS component of the real data
- scaling the open charm process down to 60% and even 0% of the level optimized by the fit on the raw mass spectrum;
- considering stricter cuts on the matching χ^2 for the single muons, i.e $\chi^2_{\text{match}} < 2.5$ and $\chi^2_{\text{match}} < 2.0$ in addition to the "nominal" selection $\chi^2_{\text{match}} < 3.0$.

Again, the variation of each input parameter is performed keeping the others fixed to their "nominal" values. As can be noticed, we consider here variations of the parameters significantly stronger than in the analysis of the p_{T} spectra and the production cross sections. Nevertheless, the systematic uncertainties estimated by performing these checks are still comparable or even smaller than the statistical uncertainties. Consistently with the analyses presented in the previous Chapters, the systematic

uncertainties are evaluated by means of the Barlow's criterion, relying on the identification of the systematic checks which significantly deviate from the averaged final value within their statistical errors, as it is explained in details in Section 6.2.1.

The resulting values for the Λ_η^{-2} and Λ_ω^{-2} parameters, expressed in $(\mathrm{GeV}/c^2)^-2$, are 1.950 ± 0.059 (stat.) ± 0.042 (syst.) and 2.241 ± 0.025 (stat.) ± 0.028 (syst.) when the target identification is not considered; these values become 1.971 ± 0.084 (stat.) ± 0.034 (syst.) and 2.236 ± 0.027 (stat.) ± 0.010 (syst.) when the target identification is required. These two results agree within their total uncertainties, so we can retain as final value for the analysis the one exploiting the largest statistics. In this case, we should consider the second result at most as a further systematic check; nevertheless, its contribution to the definition of the final systematic uncertainty comes out to be zero, as long a the Barlow's criterion is taken into account, since for both the Λ_η^{-2} and Λ_ω^{-2} parameters the difference between the two estimates (with and without considering the target identification) is smaller than the difference in quadrature between their statistical uncertainties.

In Table 8.2 we thus report the final results for the pole parameters Λ_η^{-2} and Λ_ω^{-2} as estimated within the present analysis, together with the corresponding values obtained by the analysis on the NA60 peripheral In-In data and the Lepton-G results. As it can be seen, the three measurements are in perfect agreement within their uncertainties, thus confirming the discrepancy with the prediction of the Vector Meson Dominance model in the case of the electromagnetic form factor of the ω meson. As a final comment, it is interesting to notice how the statistical error for the Λ_η^{-2} is more than two times larger than the one of the Λ_ω^{-2}, which may be surprising if one considers the number of events available for the two Dalitz decays; the explanation is that the form factor of the η meson has a lower kinematical cut-off than the form factor of the ω: then, since the high mass region is the one which better constraints the form pole parameter of the form factor, we observe such a noticeable difference between the statistical uncertainties on the two parameters extracted by the fit.

8.2.1 Disentangling the Form Factors

Once the final fit parameters and their errors are fixed, the contributions of the $\eta \to \mu^+\mu^-\gamma$ and $\omega \to \mu^+\mu^-\pi^0$ processes are disentangled, making it then possible to present the two form factors in the usual way, in order to compare them with the previous experimental points, see Figure 8.6.

The procedure works as follows. In a first step, we isolate the individual Dalitz contributions in the spectrum of Figure 8.5 (left panel, since we only consider now the option in which the target identification is not included in the analysis) subtracting the contribution of the $\rho \to \mu^+\mu^-$ decay and disentangling the $\eta \to \mu^+\mu^-\gamma$ and $\omega \to \mu^+\mu^-\pi^0$ decays as determined by the fit. This implies to use the same individual data points for the η and the ω, subtracting for the η the fit results of the ω and vice versa. Being $|F_i(M)|^2 \to 1$ for $M \to 0$ by definition of $|F_i(M)|^2$, the QED and the

Electromagnetic Transition Form Factors		
Λ_η^{-2} [GeV/c^2]$^{-2}$	NA60 p-A (this analysis)	1.950 ± 0.059 (stat.) ± 0.042 (syst.)
	NA60 In-In periph.	1.95 ± 0.17 (stat.) ± 0.04 (syst.)
	Lepton-G	1.9 ± 0.4
	VMD model	1.83
Λ_ω^{-2} [GeV/c^2]$^{-2}$	NA60 p-A (this analysis)	2.241 ± 0.025 (stat.) ± 0.028 (syst.)
	NA60 In-In periph.	2.24 ± 0.06 (stat.) ± 0.02 (syst.)
	Lepton-G	2.4 ± 0.2
	VMD model	1.66

Table 8.2: *Comparison between the present measurement of the Λ_η^{-2} and Λ_ω^{-2} parameters, the previous experimental values from NA60 peripheral In-In data [22] and Lepton-G [35, 34, 47], and the prediction of the Vector Meson Dominance model.*

form factor parts can be separately assessed for each process: this allows, in a second step, to obtain the squared form factors $|F_i(M)|^2$ by dividing the difference data for the respective decay by its QED part.

The pole parameters and their errors as obtained from the combined fit to both Dalitz decays are shown as inserts in Figure 8.6. It should be noted that these are the correct values, while independent fits through the data points of Figure 8.6 would automatically result in somewhat smaller errors of the pole parameters, since the respective other decay appears as fixed. Both panels of Figure 8.6 also include the NA60 data obtained in peripheral In-In, the Lepton-G data, and the expectations from VMD for comparison. Within the errors, perfect agreement between the three data sets is seen in both cases. Irrespective of the much reduced errors, the form factor of the η is still close to the expectation from VMD. The form factor of the ω, on the other hand, strongly deviates from the VMD, showing a relative increase close to the kinematic cut-off by a factor of ~ 10.

8.2.2 An Alternative Theoretical Prediction for the ω Form Factor

The striking discrepancy observed between the measurement of the Λ_ω^{-2} and its VMD prediction, fully confirmed by the results obtained in the present analysis, has stimulated in the last years several theoretical efforts aiming to improve the agreement with the data. It was only with the appearance of the NA60 high-precision measurement

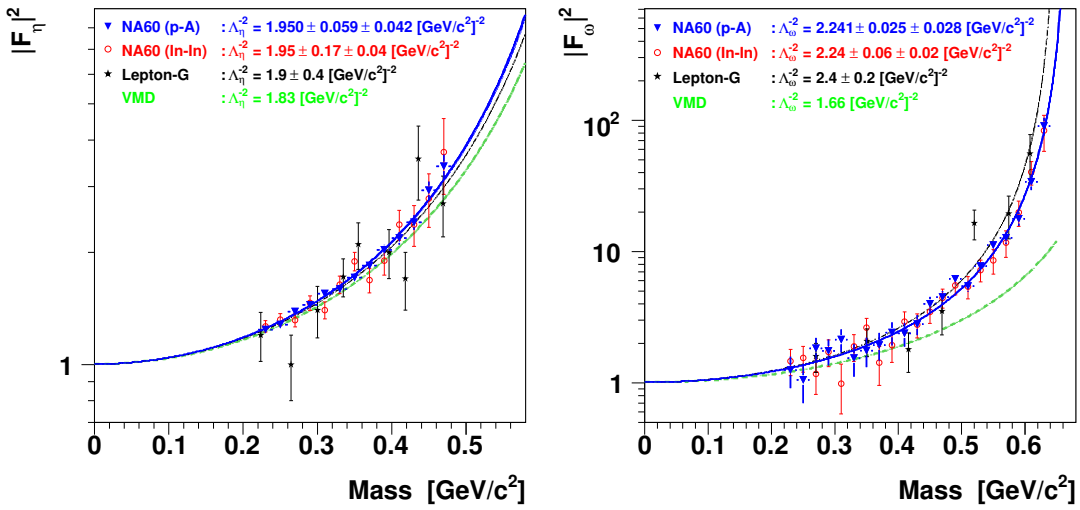

Figure 8.6: *Electromagnetic transition form factors for the η (left) and ω (right) mesons as a function of M.*

in peripheral In-In, however, that the need for an alternative – or complementary – approach to the VMD model became unavoidable.

Very recently, a new theoretical work appeared [72] which addresses – among other items – a new prediction for the mass distribution of the muon pair in the $\omega \to \mu^+\mu^-\pi^0$ decay. The difference with the standard VMD approach is two-fold: (i) first, a new form for the VMD part of the Lagrangian (the part which considers the production of the virtual photon as mediated by a virtual vector meson) is proposed; (ii) second, a next to leading order part is now included in the Lagrangian, accounting for the *direct* production of the virtual photon in the decay of the parent meson.

The resulting expression for the transition form factor in the $\omega \to \mu^+\mu^-\pi^0$ decay, as a function of the dimuon mass, has the following form:

$$F_\omega(M^2) = \frac{m_\omega}{2f\,m_V e}\left[e_A + 2b_A e_V m_V^2 \frac{m_\pi^2}{m_\omega^2} S_\rho(M^2) - \frac{1}{4} e_V h_A m_V^2 \left(1 + \frac{M^2}{m_\omega^2}\right) S_\rho(M^2)\right] \tag{8.5}$$

where the ρ meson propagator is:

$$S_\rho(M^2) = \frac{1}{M^2 - m_\rho^2 + i m_\rho \Gamma_\rho(M^2)}\,. \tag{8.6}$$

In Equation (8.5), the parameter e_A accounts for the non-VMD term, i.e. the one related to the *direct* production of the virtual photon in the decay of the parent meson; the remaining terms correspond to a VMD aproach, with the virtual photon produced via an intermediate vector meson state.

As explained in [72], in all calculations the results with and without vector-meson widths differ by less than 1% for the integrated quantities, such as the electromagnetic form factors. As the authors do not consider their leading-order calculations and the determination of the parameters to have such a good accuracy, the width has been neglected in their calculations.

The authors provide two sets of values for the parameters involved in Equation (8.5). The first is a strict leading-order set − thus solely accounting for VMD mechanisms in the Lagrangian:

$$f = 90 \text{ MeV}, \quad m_V = 776 \text{ MeV}, \quad e_V = 0.22, \quad e_A = 0, \quad h_A = 2.32, \quad b_A = 0.19.$$

The second set of parameters allows the existence of a non-vanishing term for non-VMD next to leading order production mechanisms:

$$f = 90 \text{ MeV}, \quad m_V = 776 \text{ MeV}, \quad e_V = 0.22, \quad e_A = 0.015, \quad h_A = 2.10, \quad b_A = 0.27.$$

As explained in [72], these parameters are fixed by independent fits, both on the direct dilepton decays of the light vector mesons ρ^0, ω and ϕ, and on their decays $\omega \to \pi^0\gamma$, $\omega \to \eta\gamma$, $\phi \to \eta\gamma$ − these latter being the real photon counterparts of the transition form factors we are interested in. As a result, the authors stress that the prediction for the form factor of the ω is totally constrained by this independent evaluation of the parameters (apart the condition of having $|F_\omega(M^2)|^2 \to 0$ when $M \to 0$): in this way, the comparison with the high-quality NA60 data can provide an authentic test of their theoretical model.

The comparison between the form factor (8.5) and the NA60 In-In data, presented in [72], actually appears as a significant improvement with respect to the prediction by the "standard" VMD model. The theoretical calculations now fit quite well the experimental data, except for the three data points close to the upper kinematical boundary, $M < m_\omega - m_{\pi^0}$. We are now in the position to also compare this prediction to the NA60 p-A data presented in this thesis. The comparison is shown in Figure 8.7, where the old VMD prediction and the NA60 In-In data points are also retained for comparison. As it can be seen, the new theoretical prediction shows a good agreement with the p-A NA60 data up to ~ 0.55 GeV/c^2, while still failing in describing the last data points. The same conclusions as for the comparison with the In-In data thus still stand, now profiting from an improved statistical significance.

8.3 Results for the $\omega \to \mu^+\mu^-\pi^0$ Branching Ratio

We already mentioned, at the beginning of this Chapter, that the analysis of the electromagnetic form factors profits from the the full event sample, because no dependence is expected on the physics conditions under which the particles are created. The same argument stands of course when considering the ratio between the Dalitz and 2-body decay channels of the ω meson, for which independently normalizations are found when performing the fit on the raw mass spectrum.

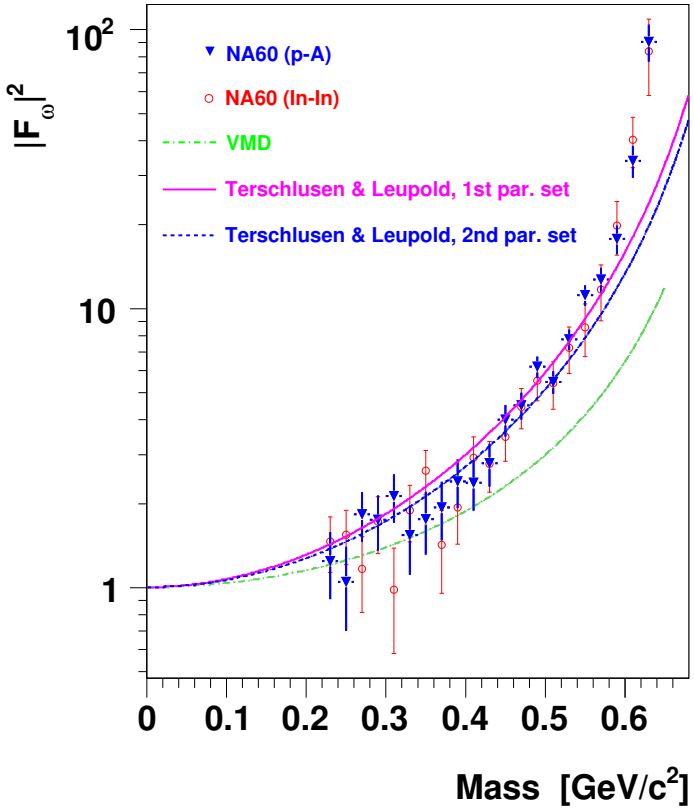

Figure 8.7: *Electromagnetic transition form factor for the ω meson, evaluated in the Dalitz decay $\omega \to \mu^+\mu^-\pi^0$. NA60 data (both p-A and peripheral In-In) are compared with the theoretical prediction of the "standard" VMD model and the recent predictions by C. Terschlüsen and S. Leupold [72].*

The measure of the relative branching ratio for the $\omega \to \mu^+\mu^-\pi^0$ decay requires that the reconstructed yields and the acceptance $\times$ efficiency for both the 2-body and the Dalitz decay of the ω can be reliably evaluated. This requirements are certainly satisfied by the 2-body decay, while the Dalitz decay suffers both from a less constrained normalization − due to its broad shape − and a remarkably small acceptance at low p_T, see Figure 8.8. As explained in Chapter 5, this is due to the increased thickness of the iron component of the hadron absorber, together with reduced tracking efficiencies both before and after the hadron absorber, which lead to a significant reduction of the acceptance $\times$ efficiency with respect to the In-In setup.

The observed small acceptance at low p_T could introduce systematic effects on the p_T-integrated estimation for the acceptance $\times$ efficiency factors. For this reason, the measurement of the relative branching ratio for the ω Dalitz decay has also been performed in the high p_T range $p_T > 1$ GeV/c. We must stress, at this regard, that this aspect is much less critical in the analysis of the electromagnetic form factors, in which the line shapes of the processes are involved, rather than their normalizations.

Furthermore, in this case the analysis is performed requiring the target identification for the dimuons, since this ensures a better control on the acceptance $\times$ efficiency

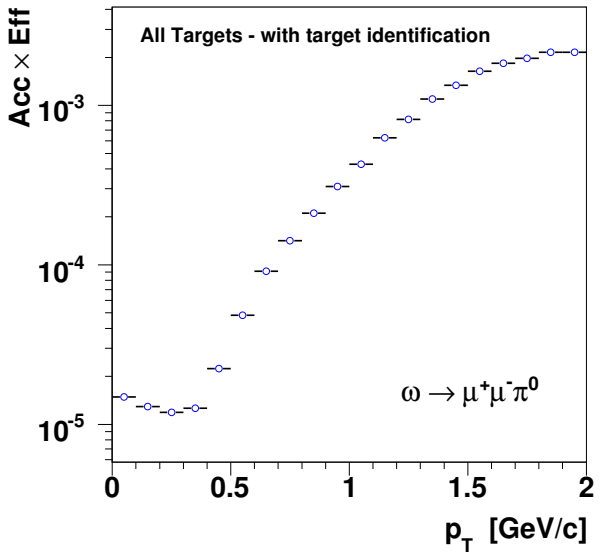

Figure 8.8: *Acceptance × efficiency for the dimuon in the $\omega \to \mu^+\mu^-$, integrated over the targets, requiring the identification of the production target for the dimuons.*

factors as a function of z for the $\omega \to \mu^+\mu^-$ and $\omega \to \mu^+\mu^-\pi^0$, needed to define the generated yield for the two processes. This choice worsens the statistical uncertainty of the results: however, this worsening does not significantly alter the precision of the measurement, since − as we will see − the total error is dominated by the systematic uncertainty.

In order a direct comparison can be assessed with the analysis of the peripheral In-In data, we present the final results in the same way as in [22]: this means that the branching ratio for the $\omega \to \mu^+\mu^-$ decay is fixed to the $\omega \to e^+e^-$ one (measured with a $3-4\%$ accuracy), while the branching ratio for the $\omega \to \mu^+\mu^-\pi^0$ decay is determined by the ratio between the observed yields for the two channels, and expressed in terms of a corrective factor with respect to the value reported in the 2008 edition of the Review of Particle Properties.

The systematic uncertainties, for the two values obtained in the present analysis, are evaluated considering the same checks performed for the analysis of the electromagnetic form factors, excluding the ones in which the choice of the acceptance and fit range options are involved − since these latter checks only relate to the analysis of the form factors. In this case, the result for $p_T > 1$ GeV/c is considered as a further systematic check, because the $\sim 15\%$ difference with the p_T-integrated value turns out to be significant with respect to their statistical uncertainties.

The measurement of the branching ratio for the $\omega \to \mu^+\mu^-\pi^0$ thus appears to be less robust than the one of the electromagnetic transition form factors; it does

not come as a surprise, hence, observing that the uncertainty on the final result is dominated by the systematic component. Averaging between the full-p_T and $p_T > 1$ GeV/c values we have in fact:

$$BR(\omega \to \mu^+\mu^-\pi^0) = 1.47 \pm 0.09\,(\text{stat.}) \pm 0.16\,(\text{syst.}) \quad \text{w.r.t. PDG08 ,}$$

which is to say, translated in absolute terms, the our estimate for the branching ratio of the $\omega \to \mu^+\mu^-\pi^0$ is:

$$BR(\omega \to \mu^+\mu^-\pi^0) = [1.41 \pm 0.09\,(\text{stat.}) \pm 0.15\,(\text{syst.})] \times 10^{-4}.$$

This final value is in agreement within two standard deviations with the estimate obtained in the analysis of the peripheral In-In data: $BR(\omega \to \mu^+\mu^-\pi^0) = [1.73 \pm 0.25\,(\text{stat.}) \pm 0.14\,(\text{syst.})] \times 10^{-4}$, dominated by the statistical uncertainty, and perfectly compatible with the current value listed in the 2010 edition of the Review of Particle Properties [55]: $BR(\omega \to \mu^+\mu^-\pi^0) = (1.3 \pm 0.4) \times 10^{-4}$, which profits from the NA60 measurement in peripheral In-In and the Lepton-G value reported by Dzhelyadin et al. in [35].

Conclusions

In this thesis we presented the analysis of the low mass ($M < 1.4$ GeV/c^2) dimuon data collected by the NA60 experiment in proton-nucleus collisions at $\sqrt{s} = 27.5$ GeV, at the CERN-SPS. Data relative to p-Be, p-Cu, p-In, p-W, p-Pb and p-U collisions have been considered in the present work.

The analysis of the p_T spectra for the ω and ϕ mesons has shown that the observed distributions cannot be explained by a thermal-like exponential function in the full p_T range accessed, while a good description of the whole observed spectrum is provided by the power-law parametrization

$$\frac{dN}{dp_T^2} \propto \left(1 + \frac{p_T^2}{p_0^2}\right)^{-\beta} .$$

The fit parameters extracted from the analysis have been used to tune the MC generations, in an iterative analysis procedure. Observations suggest the ϕ meson to have a higher mean p_T than the ω:

$$\langle p_T \rangle_\omega^{\text{NA60, p-A}} = 0.61 \pm 0.03 \pm 0.03 \text{ GeV}/c \qquad \langle p_T \rangle_\phi^{\text{NA60, p-A}} = 0.70 \pm 0.04 \pm 0.02 \text{ GeV}/c ,$$

while no evidence of target-dependence is found. Concerning the transverse momentum distribution for the η meson, agreement has been found between the trend extracted from the present analysis and the previous available measurements.

The analysis of the ratios between the production cross sections of the η, ρ and ϕ mesons to the ω, has shown a rising trend of the $\sigma_\eta/\sigma_\omega$ and $\sigma_\phi/\sigma_\omega$ ratios with respect to the NA27 measurement in p-p collisions at $\sqrt{s} = 27.5$ GeV, and as a function of A as well. Considering the strange component of the η and ϕ mesons, this observation can be interpreted as an evidence of strangeness enhancement from p-p to p-A collisions. The $\sigma_\rho/\sigma_\omega$ ratio, on the contrary, has been found to be almost independent on the production target, and compatible with unity.

The study of the nuclear dependence for the η, ω and ϕ relative production cross sections allowed us to extract the corresponding values for the α parameters, both considering the Be target or the Cu target for normalization. Directly related to the

observed nuclear dependence for the $\sigma_\eta/\sigma_\omega$ and $\sigma_\phi/\sigma_\omega$ ratios, we observe a smaller α parameter for the ω meson, with respect to the η and ϕ. The analysis as a function of p_T, in addition, clearly shows a rising trend of the α parameters as a function of p_T, as first observed by Cronin *et al.* for charged kaons and, much more recently, by the HERA-B experiment for the ϕ meson.

Finally, the analysis of the electromagnetic transition form factors of the η and ω mesons confirmed that the form factors are well described by the pole approximation

$$F(M) = \left[1 - \frac{M^2}{\Lambda^2}\right]^{-1} ,$$

with an excellent agreement with the previous available experimental results. The high statistics available for the present analysis allowed us to improve the accuracy for the measurement of the Λ_η^{-2} and Λ_ω^{-2}, for which we cite the final values:

$$\Lambda_\eta^{-2} = 1.950 \pm 0.059\ (\text{stat.})\ \pm 0.042\ (\text{syst.})\ (\text{GeV}/c^2)^{-2}$$
$$\Lambda_\omega^{-2} = 2.241 \pm 0.025\ (\text{stat.})\ \pm 0.028\ (\text{syst.})\ (\text{GeV}/c^2)^{-2}$$

improving by a factor ~ 2.5 the uncertainties of the currently available results cited in the Review of Particle Properties. These values thus confirm on more solid grounds the discrepancy between the VMD prediction for the ω and the experimental observations; an alternative theoretical approach, also considered in the analysis, offers an improved description of the ω form factor, yet still missing the part close to the kinematical cut-off.

Within the same analysis, we also measured the relative branching ratio of the $\omega \to \mu^+\mu^-\pi^0$ decay with respect to the 2-body decay $\omega \to \mu^+\mu^-$, leading to our final result:

$$BR(\omega \to \mu^+\mu^-\pi^0) = [1.41\ \pm\ 0.09\ (\text{stat.})\ \pm\ 0.15\ (\text{syst.})] \times 10^{-4}$$

in good agreement with the current value quoted by the Particle Data Group.

Bibliography

[1] K. Aamodt et al., *Transverse momentum spectra of charged particles in proton-proton collisions at $\sqrt{s} = 900$ GeV with ALICE at the LHC*, Phys. Lett., B693 (2010), pp. 53–68.

[2] M. C. Abreu et al., *Dimuon and charm production in nucleus nucleus collisions at the CERN-SPS*, Eur. Phys. J., C14 (2000), pp. 443–455.

[3] I. Abt et al., *K^{*0} and phi Meson Production in Proton-Nucleus Interactions at $\sqrt{(s)} = 41.6$ GeV*, Eur. Phys. J., C50 (2007), pp. 315–328.

[4] D. Adamova et al., *Leptonic and charged kaon decay modes of the ϕ meson measured in heavy-ion collisions at the CERN SPS*, Phys. Rev. Lett., 96 (2006), p. 152301.

[5] G. Agakishiev et al., *Enhanced production of low mass electron pairs in 200 GeV/c S-Au collisions at the CERN SPS*, Phys. Rev. Lett., 75 (1995), pp. 1272–1275.

[6] ——, *Neutral meson production in p-Be and p-Au collisions at 450 GeV beam energy*, Eur. Phys. J., C4 (1998), pp. 249–257.

[7] T. Akesson et al., *Production of π^0 and η at 11° in p-p collisions at $\sqrt{s} = 63$ GeV*, Z. Phys., C18 (1983), p. 5.

[8] ——, *A comparison of direct photon, π^0, and η production in p-$\bar{\text{p}}$ and p-p interactions at the CERN ISR*, Phys. Lett., B158 (1985), pp. 282–288.

[9] ——, *Inclusive η production at low transverse momentum in 63 GeV p-p collisions at the CERN interacting storage rings*, Phys. Lett., B178 (1986), p. 447.

[10] ——, *Low mass lepton pair production in p-Be collisions at 450 GeV/c*, Z. Phys., C68 (1995), pp. 47–64.

[11] M. S. Alam et al., *The ATLAS silicon pixel sensors*, Nucl. Instrum. Meth., A456 (2001), pp. 217–232.

[12] T. Alber et al., *Strange particle production in nuclear collisions at 200 GeV per nucleon*, Z. Phys., C64 (1994), pp. 195–207.

[13] A. N. Aleev et al., *A-Dependence of inclusive ϕ meson production in neutron - nucleus interactions at 30 GeV to 70 GeV*, Czech. J. Phys., 42 (1992), pp. 11–19.

[14] B. Alessandro et al., *ϕ production in Pb-Pb collisions at 158 GeV/c per nucleon incident momentum*, Phys. Lett., B555 (2003), pp. 147–155.

[15] C. Alt et al., *System-size dependence of strangeness production in nucleus nucleus collisions at $\sqrt{s_{NN}} = 17.3$ GeV*, Phys. Rev. Lett., 94 (2005), p. 052301.

[16] L. Anderson et al., *A high resolution spectrometer for the study of high mass muon pairs produced by intense hadron beams*, Nucl. Instr. Meth., A223 (1984), p. 26.

[17] J. Antille et al., *A measurement of the inclusive π^0 and η production cross sections at high p_T in p-$\bar{p}$ and p-p collisions at $\sqrt{s} = 24.3$ GeV*, Phys. Lett., B194 (1987), p. 568.

[18] R. Arnaldi et al., *First measurement of the ρ spectral function in high-energy nuclear collisions*, Phys. Rev. Lett., 96 (2006), p. 162302.

[19] R. Arnaldi et al., *Evidence for the production of thermal-like muon pairs with masses above 1 GeV/c^2 in 158A GeV Indium-Indium Collisions*, Eur. Phys. J., C59 (2009), pp. 607–623.

[20] R. Arnaldi et al., *First results on angular distributions of thermal dileptons in nuclear collisions*, Phys. Rev. Lett., 102 (2009), p. 222301.

[21] R. Arnaldi et al., *NA60 results on thermal dimuons*, Eur. Phys. J., C61 (2009), pp. 711–720.

[22] R. Arnaldi et al., *Study of the electromagnetic transition form-factors in $\eta \to \mu^+\mu^-\gamma$ and $\omega \to \mu^+\mu^-\pi^0$ decays with NA60*, Phys. Lett., B677 (2009), pp. 260–266.

[23] R. Bailey et al., *A-Dependence study of inclusive ϕ production*, Z. Phys., C22 (1984), p. 125.

[24] H. J. M. Banicz, K. and M. Keil, *Measurement of radiation dose and particle fluence in the NA60 vertex telescope during the Indium run, October and November 2003*, NA60 Note 2004-2, (May 2004).

[25] K. Banicz et al., *Operation and performance of the NA60 silicon pixel telescope*, Nucl. Instrum. Meth., A539 (2005), pp. 137–145.

[26] K. Banicz et al., *ϕ Production in In-In Collisions at 158 AGeV*, Eur. Phys. J., C64 (2009), pp. 1–18.

[27] R. Barlow, *Systematic errors: Facts and fictions*, (2002).

[28] F. Becattini, M. Gazdzicki, A. Keranen, J. Manninen, and R. Stock, *Study of chemical equilibrium in nucleus nucleus collisions at AGS and SPS energies*, Phys. Rev., C69 (2004), p. 024905.

[29] G. E. Brown and M. Rho, *Scaling effective Lagrangians in a dense medium*, Phys. Rev. Lett., 66 (1991), pp. 2720–2723.

[30] S. Damjanovic, *First measurement of the ρ spectral function in nuclear collisions*, Eur. Phys. J., C49 (2007), pp. 235–241.

[31] S. Damjanovic et al., *NA60 results on the rho spectral function in In-In collisions*, Nucl. Phys., A783 (2007), pp. 327–334.

[32] S. Damjanovic, R. Shahoyan, and H. J. Specht, *NA60: In hot pursuit of thermal dileptons*, CERN Cour., 49N9 (2009), pp. 31–34.

[33] A. De Falco, *NA60 results on ϕ production in the hadronic and leptonic channels in In-In collisions at 158 GeV*, Nucl. Phys., A830 (2009), pp. 753c–756c.

[34] R. I. Dzhelyadin et al., *Investigation of η meson electromagnetic structure in $\eta \to \mu^+\mu^-\gamma$ decay*, Phys. Lett., B94 (1980), p. 548.

[35] ——, *Study of the electromagnetic transition form factor in $\omega \to \pi^0\mu^+\mu^-$ DECAY*, Phys. Lett., B102 (1981), p. 296.

[36] G. J. Gounaris and J. J. Sakurai, *Finite width corrections to the vector meson dominance prediction for $\rho \to e^+e^-$*, Phys. Rev. Lett., 21 (1968), pp. 244–247.

[37] T. Hatsuda, Y. Koike, and S.-H. Lee, *Finite temperature QCD sum rules reexamined: rho, omega and A1 mesons*, Nucl. Phys., B394 (1993), pp. 221–266.

[38] T. Ishikawa et al., *ϕ photo-production from Li, C, Al, and Cu nuclei at E(γ) = 1.5 GeV - 2.4 GeV*, Phys. Lett., B608 (2005), pp. 215–222.

[39] D. Jouan, *phi and ω-ρ production in d-C, d-U, S-U and Pb-Pb at SPS energies*, J. Phys., G35 (2008), p. 104163.

[40] F. Karsch, *Lattice simulations of the thermodynamics of strongly interacting elementary particles and the exploration of new phases of matter in relativistic heavy ion collisions*, J. Phys. Conf. Ser., 46 (2006), pp. 122–131.

[41] V. Khachatryan et al., *Transverse momentum and pseudorapidity distributions of charged hadrons in p-p collisions at $\sqrt{s} = 0.9$ and 2.3 TeV*, JHEP, 02 (2010), p. 041.

[42] L. KLUBERG ET AL., *Atomic Number Dependence of Large Transverse Momentum Hadron Production by Protons*, Phys. Rev. Lett., 38 (1977), pp. 670–673.

[43] P. KOCH, B. MULLER, AND J. RAFELSKI, *Strangeness in Relativistic Heavy Ion Collisions*, Phys. Rept., 142 (1986), pp. 167–262.

[44] M. KOTULLA ET AL., *Modification of the ω-Meson Lifetime in Nuclear Matter*, Phys. Rev. Lett., 100 (2008), p. 192302.

[45] C. KOURKOUMELIS ET AL., *Inclusive η production at high p_T at the ISR*, Phys. Lett., B84 (1979), p. 277.

[46] N. M. KROLL AND W. WADA, *Internal pair production associated with the emission of high-energy gamma rays*, Phys. Rev., 98 (1955), pp. 1355–1359.

[47] L. G. LANDSBERG, *Electromagnetic Decays of Light Mesons*, Phys. Rept., 128 (1985), pp. 301–376.

[48] G.-Q. LI, C. M. KO, AND G. E. BROWN, *Enhancement of low mass dileptons in heavy ion collisions*, Phys. Rev. Lett., 75 (1995), pp. 4007–4010.

[49] C. LOURENÇO, *J/ψ, ψ' and dimuon production in p-A and S-U collisions at 200 GeV per nucleon*, Instituto Superior Técnico, Lisbon, (1995). PhD Thesis.

[50] ——, *Measuring absolute production cross sections from the proton-nucleus data collected by NA60*, NA60 Note 2007-1, (April 2007).

[51] M. MASERA, *Dimuon production below mass 3.1 GeV/c^2 in p-W and S-W interactions at 200 AGeV/c*, Nucl. Phys., A590 (1995), pp. 93c–102c.

[52] U. MOSEL, *Hadronic in-medium effects with elementary probes*, (2000).

[53] R. MUTO ET AL., *Evidence for in-medium modification of the ϕ meson at normal nuclear density*, Phys. Rev. Lett., 98 (2007), p. 042501.

[54] NA60, *Memorandum — Report on the 2004 proton run*, CERN-SPSC-2005-015, (April 2005).

[55] K. NAKAMURA, *Review of particle physics*, J. Phys., G37 (2010), p. 075021.

[56] M. NARUKI ET AL., *Experimental signature of the medium modification for ρ and ω mesons in 12 GeV p-A reactions*, Phys. Rev. Lett., 96 (2006), p. 092301.

[57] ——, *Medium modification on vector mesons observed in 12 GeV p-A reactions*, J. Phys., G34 (2007), pp. S1059–1064.

[58] R. NASSERIPOUR ET AL., *Search for medium modification of the ρ meson*, Phys. Rev. Lett., 99 (2007), p. 262302.

[59] G. B. Osborne, III, *Direct photon and neutral meson production at high transverse momentum by negative 515-GeV/c pions and 530- GeV/c protons incident upon hydrogen, beryllium, and copper targets*. FERMILAB-THESIS-1996-64.

[60] K. Ozawa et al., *Observation of ρ/ω meson modification in nuclear matter*, Phys. Rev. Lett., 86 (2001), pp. 5019–5022.

[61] A. Polyanskiy et al., *Measurement of the in-medium ϕ-meson width in proton-nucleus collisions*, (2010).

[62] J. Rafelski and B. Muller, *Strangeness Production in the Quark-Gluon Plasma*, Phys. Rev. Lett., 48 (1982), p. 1066.

[63] R. Rapp, G. Chanfray, and J. Wambach, *Medium modifications of the rho meson at CERN SPS energies*, Phys. Rev. Lett., 76 (1996), pp. 368–371.

[64] F. Sakuma et al., *Nuclear-matter modification of decay widths in the $\phi \to e^+e^-$ and $\phi \to K^+K^-$ channels*, Phys. Rev. Lett., 98 (2007), p. 152302.

[65] P. Salabura, *Private Communications*, (2010, Workshop on Electromagnetic Probes of Hot and Dense Matter, ECT* Trento).

[66] R. Shahoyan, *Combinatorial Background in the NA60 Muon Spectrometer*, NA60 Note 2004-3, (June 2004).

[67] A. Sibirtsev, H. W. Hammer, and U. G. Meissner, *A-dependence of ϕ meson production in p-A collisions*, Eur. Phys. J., A37 (2008), pp. 287–301.

[68] T. Sjostrand, S. Mrenna, and P. Z. Skands, *PYTHIA 6.4 Physics and Manual*, JHEP, 05 (2006), p. 026.

[69] H. J. Specht, *Lepton-pair production in nuclear collisions - past, present, future*, Nucl. Phys., A805 (2008), pp. 338–346.

[70] ——, *Thermal Dileptons from Hot and Dense Strongly Interacting Matter*, (2010).

[71] T. Tabaru et al., *Nuclear mass number dependence of inclusive production of ω and ϕ mesons in 12 GeV p-A collisions*, Phys. Rev., C74 (2006), p. 025201.

[72] C. Terschlusen and S. Leupold, *Electromagnetic transition form factors of light vector mesons*, Phys. Lett., B691 (2010), pp. 191–201.

[73] D. Trnka et al., *First observation of in-medium modifications of the omega meson*, Phys. Rev. Lett., 94 (2005), p. 192303.

[74] A. Uras, *Study of low mass dimuon production in 400 GeV proton- nucleus collisions at the CERN-SPS with the NA60 apparatus*, Università degli Studi di Cagliari, (2007). CERN-THESIS-2008-085.

[75] R. J. VEENHOF, *Low mass muon pair production in 450 GeV p-Be collisions*. RX-1433 (AMSTERDAM).

[76] F. VERBEURE ET AL., *Inclusive production of particles and resonances in p-p interactions at 400 GeV/c*, Sov. J. Nucl. Phys., 54 (1991), pp. 585–611.

[77] H. K. WOEHRI, *Low Mass Dimuon Production in Proton-Nucleus Collisions at 400 GeV at the CERN-SPS*, Technische Universitat Wien, (2004). PhD Thesis.

[78] H. K. WOEHRI ET AL., *Low mass dimuon production in proton-nucleus collisions with the NA60 apparatus*, Eur. Phys. J., C43 (2005), pp. 407–413.

[79] H. K. WOEHRI AND C. LOURENCO, *Heavy flavour production cross-sections from fixed target to collider energies*, J. Phys., G30 (2004), pp. S315–S324.

[80] K. WYLLIE ET AL., *A pixel readout chip for tracking at ALICE and particle identification at LHCb*. Prepared for 5th Workshop on Electronics for the LHC Experiments (LEB 99), Snowmass, Colorado, 20-24 Sep 1999.